TAMPEREEN TEKNILLINEN YLIOPISTO
TAMPERE UNIVERSITY OF TECHNOLOGY

ANTTI VESALA

EDDY CURRENT LOSSES OF HIGH-SPEED PERMANENT MAGNET SYNCHRONOUS MOTOR

Master of Science Thesis

Examiner: Assistant Professor Paavo Rasilo
The examiner and the topic approved by the Faculty of Electrical Engineering Council meeting on 05.12.2018

ABSTRACT

ANTTI VESALA: Eddy current losses of high-speed permanent magnet synchronous motor
Tampere University of Technology
Master of Science Thesis, 79 pages, 5 Appendix pages
December 2018
Master's Degree Programme in Electrical Engineering
Major: Power Systems and Market
Examiner: Assistant Professor Paavo Rasilo

Keywords: eddy current losses, Elmer, electromagnetics, finite element method, high-speed electric machine, permanent magnet synchronous machine

In this thesis, an Ingersoll-Rand made high-speed permanent magnet synchronous motor is simulated by using the finite element method. The interest for Ingersoll-Rand in this work is to study how to use the open source software Elmer for electric machine simulations. This work is written at FS Dynamics' office in Tampere. FS Dynamics is a co-partner in this thesis and their motivation is to learn more about electromagnetic simulations. The use of numerical simulations for the electric machines are increasing since these simulations give a good estimation of the machine properties. Simulations are especially effective in electric machine design since they reduce the number of prototypes required and thus the manufacturing costs of the machine. In addition, the variables at some points of the geometry cannot be measured in real life but the numerical method will give an estimation of the calculated variable at every point in the geometry. In electric machines, the interesting variables include the magnetic flux density and current density.

This thesis explains how to create a workflow for simulating electric machines using Elmer as a solver. This workflow consists of creating the geometry model by SpaceClaim, mesh by Salome and post-processing is done by using Paraview and Python scripts. The motor is simulated in four different operation points. These simulations consist of nominal load and no-load operation of the motor. At both of these operation points, the stator windings are supplied with sinusoidal voltage or pulse width modulated voltage. The eddy current losses and copper losses are studied at these different simulation cases and compared to each other. From the results, it is clearly seen that the pulse width modulated voltage increases these losses in both operation points. The nominal load total losses are higher compared to the no-load total losses since the currents are lower without the load. The eddy current losses decrease when changing the motor operation from the nominal load to no-load with sinusoidal supply. However, with the pulse width modulated voltage the eddy current losses increase when changing the operation point. In addition, the start-up transients in the simulations can be reduced by the following three methods. The motor is started by the ramped sinusoidal signal. Electric conductivity is added after the motor has reached steady-state operation. At last, the sinusoidal voltage is changed to pulse width modulated voltage during one fundamental period. These methods were found working rather well in this thesis.

TIIVISTELMÄ

ANTTI VESALA: Suurnopeuksisen kestomagneettitahtimoottorin pyörrevirtahäviöt
Tampereen teknillinen yliopisto
Diplomityö, 79 sivua, 5 liitesivua
Joulukuu 2018
Sähkötekniikan diplomi-insinöörin tutkinto-ohjelma
Pääaine: Sähköverkot ja -markkinat
Tarkastaja: Akatemiatutkija Paavo Rasilo

Avainsanat: Elmer, elementtimenetelmä, kestomagneettitahtikone, pyörrevirtahäviöt, suurnopeussähkökone, sähkömagnetiikka

Tässä työssä tutkitaan Ingersoll-Rand:n valmistamaa suurnopeuksista kestomagneettitahtimoottoria elementtimenetelmää käyttäen. Ingersoll-Rand:n kiinnostus tässä työssä on tutkia avoimen lähdekoodin ohjelman, nimeltään Elmer, käyttöä sähkökoneiden simuloinneissa. Työ on kirjoitettu FS Dynamics:n toimistolla Tampereella. FS Dynamics on toinen diplomityön yhteistyökumppaneista ja on kiinnostunut laajentamaan osaamistaan sähkömagneettisessa simuloinnissa. Sähkömagneettisen simuloinnin käyttö on kasvamassa, koska simuloinnit antavat hyvän arvion sähkökoneen ominaisuuksista. Simuloinnit ovat erityisen tehokkaita sähkökoneiden suunnittelussa, koska ne vähentävät tarvittavien prototyyppien määrää ja siten koneen valmistuskustannuksia. Lisäksi, joitakin paikkoja geometriassa ei voida mitata reaalimaailmassa ja tarvitaan numeerista laskentaa, jonka avulla haluttu muuttuja voidaan laskea jokaisessa pisteessä geometriaa. Sähkökoneen tapauksessa kiinnostavia muuttujia ovat esimerkiksi magneettivuon tiheys ja virrantiheys.

Tämä diplomityö selvittää kuinka luoda työvuo sähkömagneettiseen laskentaan käyttämällä Elmer-ohjelmaa elementtimenetelmän ratkaisijana. Työvuo alkaa geometrian muodostamisesta SpaceClaim-ohjelmalla, verkon muodostamisesta Salome-ohjelmalla ja tulosten tarkastelusta Paraview-ohjelmalla ja Python-koodilla. Moottoria simuloidaan nimellisellä kuormituksella ja kuormittamattomana eli tyhjäkäynnillä. Molemmissa toimintapisteissä staattorikäämeille syötetään joko sinimuotoista tai pulssimoduloitua jännitettä. Tällöin saadaan neljä eri simulointia. Kaikissa simuloinneissa lasketaan pyörrevirtahäviöt roottorissa ja staattorin käämihäviöt. Simulointien jälkeen tuloksia verrataan toisiinsa. Tuloksista huomataan selvästi, että häviöt kasvavat aina, kun siirrytään sinimuotoisesta jännitteestä pulssimoduloituun. Kokonaishäviöt ovat suuremmat nimellisellä kuormalla verrattuna tyhjäkäyntiin johtuen suuremmista käämivirroista. Pyörrevirtahäviöt pienenevät sinijännitteellä ja suurenevat pulssimoduloidulla jännitteellä siirryttäessä nimelliseltä kuormalta tyhjäkäynnille. Lisäksi työssä tutkitaan kuinka käynnistyksen aiheuttamia transientteja voitaisiin vähentää, jotta simulointiaikaa saataisiin lyhyemmäksi. Edellä mainitun saavuttamiseksi on käytetty avuksi kolmea eri menetelmää. Aluksi moottori käynnistetään sinimuotoisella ramppifunktiolla sähkönjohtavuuden ollessa nolla joka materiaalille. Kun simulointi saavuttaa tasapainotilan, lisätään roottorin materiaaleille sähkönjohtavuus. Tämä sama menetelmä ei onnistu suoraan pulssimoduloidulle jännitteelle, vaan sinimuotoinen jännite muutetaan pulssimoduloiduksi yhden jakson aikana. Edellä kuvatut menetelmät näyttivät toimivan melko hyvin simuloinneissa.

PREFACE

This thesis was written between January 2018 and November 2018 at FS Dynamics' office in Tampere. I would like to thank my supervisor assistant professor Paavo Rasilo who recommended me to apply for this Master's thesis position. The active guidance and discussion during this period provided me with the required knowledge to complete this thesis. I would also like to thank Arttu Kalliovalkama from FS Dynamics for choosing me for this position. The support and patience during this thesis were much appreciated. From Ingersoll-Rand, I would like to thank Petri Mäki-Ontto for the interesting topic and advice on how to advance in the simulations. The support of the Elmer developers from CSC was really helpful when debugging the simulation model. In particular, I would like to thank Peter Råback and Juhani Kataja for giving me important advice related to the use of Elmer. At last, I would like to thank all members of FS Dynamics for providing a great working environment and guidance during this thesis.

Most of all, I would like to thank my family for moral support. Especially my brother Jussi provided much-needed support during this thesis.

Tampere, 21.11.2018

Antti Vesala

CONTENTS

LIST OF ABBREVIATIONS AND SYMBOLS

AC	Alternating current
DC	Direct current
FEM	Finite element method
IR	Ingersoll-Rand
PDE	Partial differential equation
PMSM	Permanent magnet synchronous machine (or motor)
PWM	Pulse width modulation
RMS	Root mean square

$\boldsymbol{A}$	Magnetic vector potential
$\boldsymbol{a}$	Nodal value vector
$\boldsymbol{a}'$	Time derivative of nodal value vector
A_z	Magnetic vector potential z-component
a_n	Numerical constant calculated by Rayleigh method
$\boldsymbol{B}$	Magnetic flux density
B_r	Remanence flux density, magnetic flux density r-component
$\boldsymbol{B}_{aa'}$	Magnetic flux density for phase a
$\boldsymbol{B}_{bb'}$	Magnetic flux density for phase b
$\boldsymbol{B}_{cc'}$	Magnetic flux density for phase c
$\boldsymbol{B}_{net}$	Net Magnetic flux density
$\boldsymbol{B}_M$	Magnetic flux density magnitude
BH_{max}	Energy product
B_φ	Magnetic flux density φ-component
C_d	Skin friction coefficient for turbulent flow
$\boldsymbol{D}$	Electric flux density
D_r	Rotor outer diameter
$\boldsymbol{E}$	Electric field strength
E	Young's modulus
E_A	Induced voltage
E_{emf}	Electromotive force
e_{ind}	Induced voltage
$\boldsymbol{F}$	Auxiliary variable for the Stokes's and Gauss's theorems
f	Frequency
f_s	Switching frequency
f_1	Fundamental frequency of the inverter
$\boldsymbol{H}$	Magnetic field strength
H_{ci}	Intrinsic coercive field strength
I	Inertia of the rotor
I_m	Stator coil current magnitude
$i_{aa'}$	Stator coil current for phase a
$i_{bb'}$	Stator coil current for phase b
$i_{cc'}$	Stator coil current for phase c
$\boldsymbol{J}$	Current density, Jacobian matrix
$\boldsymbol{J}_s$	Source current density, surface current density
$J_{s,z}$	Source current density z-component
j	Turns per slot

K_c	Classical eddy current losses coefficient
K_e	Excess eddy current losses coefficient
K_h	Hysteresis losses coefficient
k_d	Distribution factor, ratio of effective AC vs. DC resistance
k_p	Pitching factor
k_w	Winding factor
L_d	Direct-axis inductance
L_q	Quadrature-axis inductance
l	Length, axial length of the rotor
m	Number of phases
m_a	Amplitude modulation index
m_f	Frequency modulation index
N	Rotational speed of the rotor, nodal point, number of turns in a coil
N_i	Nodal point N_i for the element k, shape function
$\boldsymbol{n}$	normal unit vector of the surface
n	Number of element nodal points
n_s	Synchronous speed
P	Power, number of poles, general eddy current losses
P_{Cu}	Copper losses
P_{stray}	Proximity effect losses
P_{iron}	Iron losses
P_w	Windage losses
p	Number of pole pairs
Q	Number of stator slots
q	Number of slots per pole and phase
R_s	Stator phase resistance
Re	Reynolds number
r	Radius of the rotor, residual
r_r	Inner radii of the air gap
r_s	Outer radii of the air gap
S_{ag}	Cross-sectional area of the air gap
T_e	Electromagnetic torque
t	Time
V	Volume
V_a	Phase voltage a
$(\hat{V}_{Ao})_1$	Fundamental voltage
V_b	Phase voltage b
$\hat{V}_{control}$	Amplitude of the control signal
$\hat{V}_{control\ a}$	Control signal a amplitude
$\hat{V}_{control\ b}$	Control signal b amplitude
V_{dc}	Rectified DC voltage
V_{LL}	Line to line voltage
V_{tip}	Rotor tip speed
$\hat{V}_{tri}$	Amplitude of the triangular signal
$\boldsymbol{v}$	Velocity
v	Harmonic number
w	Weight function, coil width
$\hat{\boldsymbol{x}}$	The unit vector in the horizontal direction
x	x-coordinate
$\hat{\boldsymbol{y}}$	The unit vector in the vertical direction

y	y-coordinate
z	z-coordinate
α	Temperature coefficient for B_{r}, angle
β	Temperature coefficient for H_{ci}
Γ	Boundary line region
γ	Electric angle between stator teeth
δ	Power angle, skin depth
ε_0	Permittivity of vacuum
ε_{r}	Relative permittivity
ξ	ξ-coordinate
η	η-coordinate
θ_{e}	Electrical angle
θ_{m}	Mechanical angle
ϑ	Azimuthal coordinate
Λ	Area coordinates
μ_{r}	Relative permeability
μ_0	Permeability of vacuum
μ_1	Mass in per unit length
ρ	Resistivity, density, electric charge density
ρ_{s}	Surface charge density
σ	Electric conductivity
τ_{p}	Pole pitch
τ	Fractional-pitch in electrical degrees
ϕ	Magnetic flux, air gap length
φ	Electric scalar potential
Ω	Global element domain, field region
Ω_{ref}	Reference element domain
ω	Angular frequency
Δ	Triangle element area
∇	Nabla

1. INTRODUCTION

In this thesis, a permanent magnet synchronous motor (PMSM) is studied by using finite element method (FEM). The aim is to simulate eddy current losses in PMSM. Aforementioned motor is currently in use at the Aalto University laboratory and it is made by Ingersoll-Rand (IR), which is a co-partner of this thesis. The other company involved is FS Dynamics and the thesis was written in their premises in Tampere. IR's interest in this work is to create a workflow for using Elmer as a partial differential equation (PDE) solver. Elmer is mainly developed by CSC – IT Center for Science and it is an open source tool for multiphysical simulations [1]. Elmer uses the finite element method to solve the PDEs. For the above reason, the use of Elmer in this thesis was predetermined and the other used software was selected by the author. The interest for FS Dynamics was to achieve a deeper knowledge of the electromagnetic simulations since the company is focused on the computational fluid and structural mechanics.

Finite element method is based on numerical methods, which allow the solution of the desired variable by computer. This requires initial geometry to be discretized. In addition, the time requires discretization in a transient case. The FEM was first presented in the 1950s for structural mechanic applications. Later on, this method was also expanded to electromagnetics and the first simulations for the electric machine were presented in the early 1970s. Currently, FEM is the most used method for solving electromagnetic problems since the method can be applied to complex geometries and nonlinear materials. This method gives a good estimation of electric machine properties hence reducing the manufacturing costs by increasing the different loadings within the machine. Otherwise, the machine would require multiple prototypes and measurements to justify the design. In addition, some places in electric machines cannot be measured and the simulation is the only option since it allows the field variable to be solved at every point in the geometry. FEM can also be used to calculate the losses in the electric machine, which is one of the main topics of this thesis. [2, p. 1:1-1:3]

Currently, there is some commercial software available, which includes the electromagnetic solvers. These softwares are for example ANSYS Maxwell, COMSOL Multiphysics, and Star-CCM+. However, there are some significant license costs and therefore universities, for example, may use open source or in-house software for research and study material. Some common open source software solvers for electromagnetics are Finite Element Method Magnetics, ONELAB GetDP, and Elmer. There are two in-depth tutorials of how to simulate an electric machine using Elmer [3], [4]. The simulated electric machines were PMSM and induction machine. There is also some previous research material related to the use of Elmer in the electric machine applications [5]–[8].

In this thesis, a 2D-model of the motor and the workflow for the electromagnetic simulations are created. The results are studied at different operation points and voltage supplies. In addition, the methods for reducing the transients are studied. The main goals are the following:

1. Create a workflow to simulate electric machine using Elmer as a solver.
2. Simulate the motor at nominal and no-load operation and calculate the eddy current losses at different parts of the rotor using sinusoidal and pulse width modulated (PWM) supply voltage.
3. Study how the transients at the start of the simulation can be reduced.

The workflow presented is similar to [3]–[4] with the main difference being the geometry and the mesh software. The eddy current losses are calculated with varying operation point and supply voltage, so these differences can be effectively compared. In addition, some common but not often documented methods to reduce transients are introduced.

The thesis consists of two main parts where the first part explains the required background theory and the second part consists of the creation of the simulation model and results that were obtained using this model. The chapter after the introduction explains the fundamentals of the PMSM operation principle. Most important parts of this chapter are focused on different rotor structures, stator-winding layouts and the operation principle of the frequency converter. The third chapter focuses on the effects of the high-speed operation and the generation of different losses. In the last theory chapter, the eddy current formulations are derived. After that, the basic principle of the finite element method is explained and applied to the derived eddy current equations.

In the second part, the simulation model is created. This chapter introduces the necessary starting parameters and the stator, and the rotor structures for the simulated motor. The only predetermined program in the created workflow is Elmer since IR desired to create a workflow focusing on the use of Elmer software. Other software in the workflow are SpaceClaim, Salome, Paraview and Python. All of these are open source programs except for the SpaceClaim, which is a commercial product. The results consist of the eddy current losses of the different rotor parts at nominal and no-load motor operation. In addition, the used supply voltage is either sinusoidal or pulse width modulated, which results in four different simulation cases. In summary, the losses in these different cases are compared.

2. PERMANENT MAGNET SYNCHRONOUS MACHINES

In the last twenty years, the permanent magnet synchronous machine has gained popularity over the traditional induction machine. Many induction machines are replaced by a more convenient PMSM in different converter fed electric drives and control systems. There are two main reasons for this. The fast commercialization of NdFeB magnets in the eighties and the rare-earth magnet boom in China at the start of the nineties, which significantly reduced the price of the rare-earth magnets. This reduction of price made the use of PMSMs affordable since it is more expensive to build compared to the equally rated induction machine. At the same time, the machining of the magnets developed and different shaped magnets were more readily available. [9, p. 13-14]

Another reason for the popularity of PMSMs is the importance of energy efficiency. The exploitation of energy resources has made a need for more efficient and compact electromechanical systems. Either the electric machines can replace the old mechanical system or they can be coupled with the mechanical system. A car is an example of this since hybrid uses both fuel and electric powered system and electric car run only by electricity. The PMSMs are a good choice for these kinds of electromechanical systems since they are very energy efficient and have a high power factor. This is due to the fact that PMSMs do not require a separate excitation circuit in the rotor because of the use of permanent magnets. The absence of a separate excitation circuit also increases the power-to-weight ratio since the permanent magnets can produce the same amount of magnetization with more compact size in low power applications. [9, p. 13-14]

2.1 Magnetic materials

Magnetic flux density $\boldsymbol{B}$ and magnetic field strength $\boldsymbol{H}$ are dependent on the relative permeability μ_{r} of the medium. According to the magnetic properties of the medium, magnetic materials can be divided in three different categories: Diamagnetic, paramagnetic, and ferromagnetic. In diamagnetic materials, the relative permeability of the medium is below one and in paramagnetic materials, relative permeability is slightly over one. Examples of diamagnetic materials are copper and gold. Paramagnetic materials are for example aluminum and wolfram. Materials that have relative permeability close to one, which is very close to relative permeability of vacuum (1), are called non-magnetic materials. Examples of non-magnetic materials are air and rubber. Ferromagnetic materials typically have very high relative permeability. Common ferromagnetic material is iron, which is usually alloyed with a small amount of silicon. [10, p. 9:6-9:7]

It is known that every material consists of atoms. Atoms consist of a nucleus and the electrons circulating around it. Neutrons, which have no electric charge, and protons, which have positive electric charge, are inside the nucleus. Electrons have a negative charge and together with protons, they hold the atom together. The circulation of electrons also creates a circulating current around the nucleus and thus a magnetic dipole moment. In addition, the nucleus and electrons spin around their own axis and create an additional magnetic dipole moment called *spin*. However, spin is usually insignificantly small. Figure 1 demonstrates the resultant dipole moment. [10, p. 9:3]

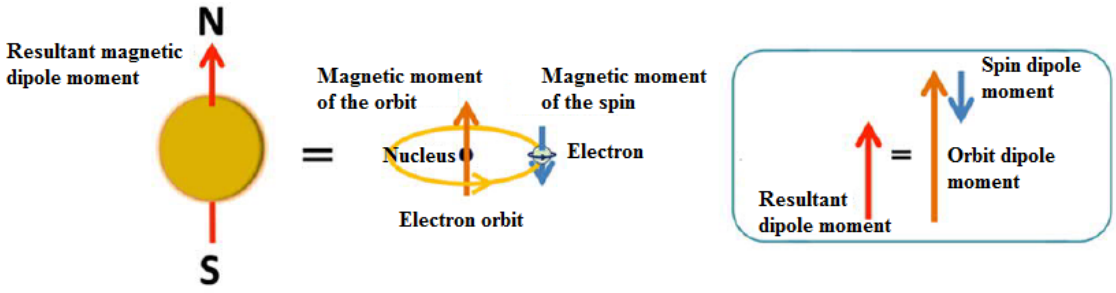

Figure 1. *Demonstration of magnetic dipole moments. Adapted from [10, 9:3].*

As can be seen from Figure 1, the resultant dipole moment consists of both spin and orbit dipole moments. Without the exterior magnetic field, the different dipole moments in the atoms cancel out and there is no resultant dipole moment. However, permanent magnets are an exception because they have a permanent resultant dipole moment.

In non-magnetic material such as air, the dipole moments in the atoms cancel out and the resultant moment is zero. In ferromagnetic materials, these dipole moments do not cancel out perfectly. In these materials there are different regions of elementary magnets where the dipole moment is in the same direction. These regions are called Weiss domains. Different Weiss domains are separated by transition areas, which are called Bloch walls. Figure 2 demonstrates the Weiss domains (left) and the transition area between two domains (right). [10, p. 9:3, 9:8]

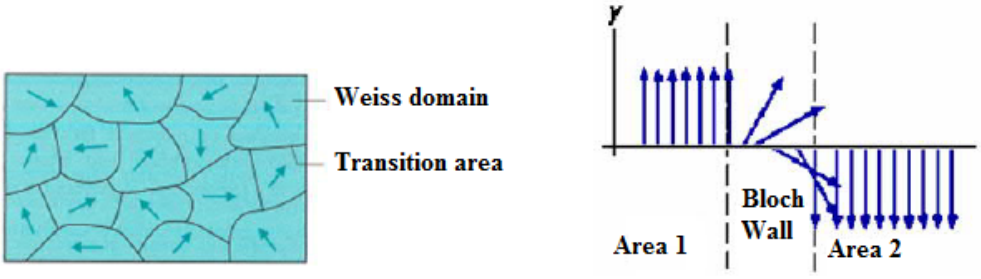

Figure 2. *Weiss domains and Bloch walls of a ferromagnetic material. Adapted from [10, p. 9:8].*

Without the exterior magnetic field, the Weiss domains are randomly organized. However, when the exterior field is applied the different Weiss domain elementary magnet directions unify and the material starts to strengthen the applied magnetic field. This change of direction happens in two steps. First, the areas that are in the same direction as applied field increase in expense of the domains at the opposite direction. Secondly, the remaining Weiss domains change their directions according to the applied field. When the field strength is increased abruptly, the Bloch walls can leave from their position at rest and do not return to their original position after the exterior field is removed. These displacements are called Barkhausen jumps and they result from Barkhausen noise and ferromagnetic hysteresis. [11, p. 183-185]

2.2 Permanent magnet materials

Some ferromagnetic materials can be permanently magnetized by using high external field strength. High external field orientates all the Weiss domains in the same direction and after the external field is closed, the Weiss domains remain in the same direction. The remaining field is not as strong as it was with the external field but it stabilizes to a stationary condition. For Weiss domains to behave this way, the material has to have high crystal anisotropy. High anisotropy is achieved by using rare-earth magnets as a base material. [11, p. 200]

Commercially, the most used permanent magnet materials are ferrite, aluminum nickel cobalt (Alnico), samarium cobalt (SmCo) and neodymium iron boron (NdFeB). Ferrite was the first permanent magnet material used in commercial products. Ferrite is relatively cheap but lacks the qualities of the other permanent magnet materials. Next, the Alnico and SmCo were invented. The newest permanent magnet material in electrical machines is NdFeB. The following terms can be used to compare the properties of permanent magnets: [11, p. 200-201]

- **Remanence B_r:** Describes the remaining magnetic flux density of the material when the external magnetic field strength is brought to zero.
- **Intrinsic coercivity H_{ci}:** The field strength that is required to bring the magnetization strength of the material to zero.
- **Energy product (BH_{max}):** Describes the energy density of the permanent magnet material.
- **Temperature coefficients α and β for B_r and H_{ci}:** Remanence and intrinsic coercivity values are usually given at the room temperature (21°C) so these coefficients can be used to estimate the values in different temperatures.
- **Saturation field strength H_s:** After this value is reached, the magnetization value of the material does not increase anymore when the external field strength is increased.

- **Curie temperature T_c:** When this temperature is exceeded, the permanent magnet demagnetizes. In other words, completely loses its magnetization and starts to behave paramagnetically. [12]

Depending on the application, there are four different material choices for the permanent magnets. Table 1 gives the typical properties of these permanent magnet materials.

Table 1. *Typical permanent magnet materials and their properties. Adapted from [12, p. 2].*

	Ferrite	***AlNiCo***	***SmCo***	***SmCo***	***SmCo***	***NdFeB***	***NdFeB***
Property	Ceramic 8	AlNiCo 5	1:5	1:5 TC	2:17	Bonded	Sintered
$B_\mathrm{r}(\mathrm{T})$	0.4	1.25	0.9	0.61	1.04	0.69	1.34
$\alpha(\%/°\mathrm{C})$	-0.18	-0.02	-0.045	-0.001	-0.035	-0.105	-0.12
$BH_\mathrm{max}\left(\frac{\mathrm{kJ}}{\mathrm{m}^3}\right)$	30.24	43.77	159.2	71.62	206.9	79.58	342.2
$H_\mathrm{ci}(\mathrm{kA/m})$	263.2	51.05	2393	2393	1994	717.9	1196
$\beta(\%/°\mathrm{C})$	+0.4	-0.015	-0.3	-0.02	-0.3	-0.4	-0.6
$H_\mathrm{s}(\mathrm{kA/m})$	797.7	239.3	1595	3190	2393	2791	2791
$T_\mathrm{c}(°\mathrm{C})$	460	890	727	729	825	360	310

According to Table 1, the sintered NdFeB permanent magnets have superior energy density compared to other materials. The same sized permanent magnet of NdFeB material delivers more flux compared to other permanent magnet materials. However, it has the lowest Curie temperature and high costs since it is made of iron alloyed with rare-earth metals. In addition, NdFeB is very sensitive to corrosion because it is made of iron alloys. Therefore, neodymium magnets are usually coated with some other corrosion resistant material like nickel and this weakens the flux component. [11, p. 202]

The advantage of SmCo magnets compared to NdFeB magnets is that they have excellent heat resistance as can be seen from Table 1. Using the 2:17 alloy the Curie temperature is over twice compared to neodymium magnets. In addition, SmCo magnets are more corrosion resistant. However, both samarium and cobalt are very rare materials, so the costs are even higher compared to neodymium magnets. [11, p. 202]

The advantage of ferrites is that they are very cheap since they are made of ceramics. However, ferrites have very limited properties and are used in applications that do not require the higher-powered SmCo or NdFeB magnets. Ferrites are still dominant in the market. [11, p. 202]

AlNiCo magnets have very high Curie temperature and they are used in technical applications where temperature stability is critical. In addition, the remanence flux is high in AlNiCo material but it is easily demagnetized since it has low H_{ci} according to Table 1. In addition, the energy density is rather poor compared to SmCo and NdFeB. [11, p. 202]

2.3 Operating principle of the synchronous machine

Since PMSM is a specially structured synchronous machine, the working principle of synchronous machine in general is studied first. Originally, synchronous machines were used mainly in high-powered motor and generator applications where constant rotational speed and possibly a reactive power compensation were needed. Nowadays, synchronous machines are used in many different applications, which require accurate control of rotational speed like robotics. The use of frequency converters has made this possible since the ability to adjust the frequency of the machine enables accurate speed control because the speed of the synchronous machine is always the same as the synchronous speed. In alternating current (AC) machines the synchronous frequency is defined as

$$n_s = \frac{f}{p} \tag{2.1}$$

where n_s is the synchronous speed, f is the frequency and p is the number of pole pairs. A pole pair consists of two magnetic poles, namely North and South pole, which means that the pole number is twice the pole pair number. It can be seen that by changing the frequency of the synchronous machine, it is possible to control the rotation speed of the machine. [13, p. 4:2], [14, p. 5]

Synchronous machines can be separated into three different main categories, which are separately magnetized synchronous machines, synchronous reluctance machines, and permanent magnet machines. This thesis focuses on permanent magnet machines but in order to understand the operating principle, a simple separately magnetized machine structure is shown in Figure 3.

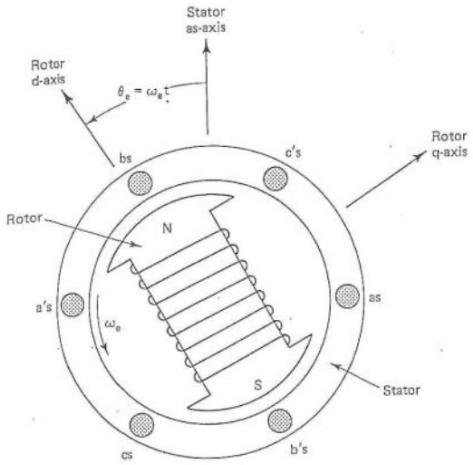

Figure 3. *Idealized separately magnetized synchronous machine [15, p. 4].*

As can be seen from Figure 3, electric machines consist of two main parts: the rotating part is called the rotor and the stationary part is called the stator. The stator structure has three-phase windings and is similar compared to all AC machines but the rotor is magnetized with an external circuit. The circuit magnetizes the rotor so that it has a constant magnetic field. Additionally, the rotor can be magnetized with slip rings or brushes. The magnetic flux flows from north to south pole via an air gap and stator structures. By using three-phase windings in the stator, it is possible to create a rotating magnetic field that has a constant amplitude. The flux lines tend to be parallel to each other because then the flux flows with the path of the least resistance. This forces the rotor to rotate according to the speed of the stator created field (synchronous speed). The power angle δ is the difference between the magnetic axis of the rotor and stator fields. The rotor is divided into direct-axis (d-axis) and quadrature-axis (q-axis), according to the structure of the rotor. The rotor structure can be made either a salient pole or a non-salient pole. The non-salient pole machine is structured cylindrically and the air gap is uniform, in which case the inductances of d- and q-axis are equal ($L_\mathrm{d} = L_\mathrm{q}$). However, in salient pole machines, the air gap is non-uniform and the d-axis inductance value is higher compared to the q-axis value ($L_\mathrm{d} > L_\mathrm{q}$). The rotor in Figure 3 is structured with one salient pole pair and it can be seen that the air gap at the q-axis is significantly larger. [15, p. 4-6]

In asynchronous machines, the rotor structure consists of squirrel cage winding, which is short-circuited at the rotor ends or with special slip rings. The rotating stator magnetic field then induces the voltage and the current (short-circuit) in the squirrel cage bars and the induced currents create a force in the rotor bars, which starts to rotate the rotor. The working principle is based on Faraday's induction law and it can only work with a changing magnetic field. The asynchronous machine always needs to operate at some slip in order to work. The similar winding as the squirrel cage winding can also be added to synchronous machines in order to stabilize vibrations in transient conditions [13, p. 4:3]. In addition, using the squirrel cage winding in synchronous machines it is also possible to start the machine as an asynchronous machine and synchronize the machine to the

synchronous speed [13, p. 4:3]. Without the squirrel cage assisted winding or a frequency converter, the synchronous motor needs assisting motor to start the machine because it does not have a starting torque. [14, p. 11-14, 71]

The term synchronous machine consists of the machine operating either as a generator or as a motor. The equations are the same in both cases but the direction of the torque is the opposite. In addition, the torque of the synchronous machine is different depending on the rotor structure. In the salient pole structure, the d- and q-axis have different reluctances (magnetic resistance) because of the different air gap lengths and the rotor tends to rotate to the position where the main flux has the least resistance. In non-salient structures, the air gap length is the same for both axes so the reluctances are also the same and there is no reluctance torque. Figure 4 shows the torque curves of the salient and non-salient pole synchronous machines.

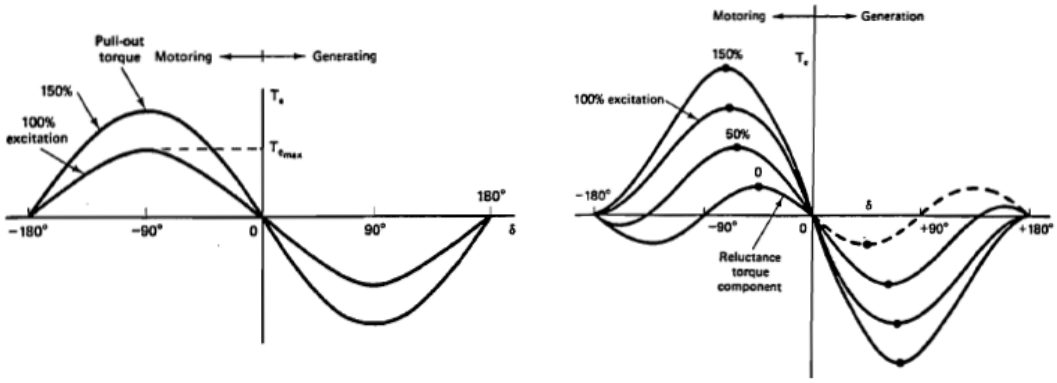

Figure 4. *Torque curves of non-salient (left) and salient pole (right) synchronous machines. Adapted from [13, p. 4:4-4:5].*

As can be seen from Figure 4, the motor operates with positive torque values and generator with the negative torque values. The torque is plotted with respect to power angle δ, which is the angle between the stator flux and rotor flux. In non-salient pole machines (left), the torque is at a maximum when the power angle is $\pm 90^{o}$ and the machine should be operated between these values or else the machine will lose operating stability. In salient pole machines (right), the maximum torque is obtained at the power angle values of $\pm 45^{o}$ due to the addition of reluctance torque. In synchronous reluctance machines, the only torque production is based on this reluctance torque. [13, p. 4:4-4:5]

2.4 Structure of permanent magnet synchronous machine

The previous section described the working principle for the externally magnetized synchronous machine. The PMSM works with the same principle but in this case, we can remove the external rotor circuit and use permanent magnets instead, which also makes the PMSM very efficient. The stator winding is identical to other synchronous machines.

Usually, permanent magnet motors are supplied with frequency converters but if the motor is supplied straight from the grid, it behaves as a common constantly magnetized synchronous machine. Frequency converter supply and the development of permanent magnet materials have made it possible to use PMSMs in numerous applications from servo drives to high-powered ship propulsion systems. Typical properties of the PMSMs are high airgap flux density, high power-to-weight ratio, high efficiency, and high power factor. [14, p. 129-130]

PMSMs can be divided into two categories: surface magnet machines or embedded magnet machines. Figure 5 shows the different PMSM rotor structures.

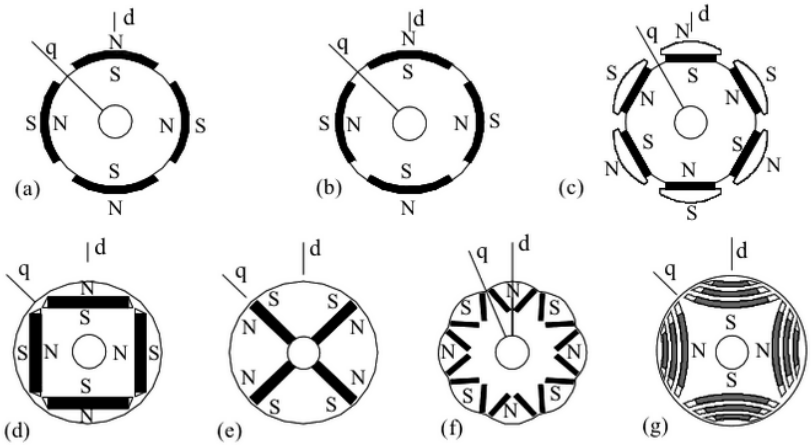

Figure 5. *Different rotor structures of PMSM [11, p. 397].*

In Figure 5, the dq-axis has been marked for different rotor structures. Different structures demonstrates the magnetic property difference (permeability) between the permanent magnets and the rotor iron. The inductance values are also different depending on the magnetic properties. However, if the structure is according to Figure 5 a, then the d- and q-axis inductances can be considered equal because the permeability of permanent magnets is very close to the permeability of air. This structure is similar to a separately magnetized synchronous machine with a non-salient pole structure. The structures b–g are embedded magnet structures and they have significant differences for d- and q-axis inductances. These structures are similar to the salient pole structure in separately magnetized synchronous machines. [14, p. 132]

Both of these structures have different benefits and downsides. Surface mounted PMSMs have better efficiency since they need lesser permanent magnet material to produce the same amount of power compared to the embedded magnet design. That is the main reason why the surface mounted PMSMs are widely used. The embedded magnet machines have better weight-to-torque ratio because of high airgap flux density. However, the embedded magnet machines require more permanent magnet material. In addition, in embedded machines, the permanent magnets are better protected from mechanical stress and demagnetization. [16, p. 3]

2.5 Rotating magnetic field

The stator structure is similar for both asynchronous and synchronous machines. It is made of thin steel laminations stacked on top of each other. Between the sheets is a thin layer of insulating material. Even though the stator is a static structure the variating magnetic flux causes eddy currents to flow in the stator structure. However, the layered structure of the stator reduces the eddy currents since they cannot pass the insulation layer. [14, p. 71-73]

As stated in section 2.3, flux lines of the rotor and the stator fields tend to be parallel to each other at the point of least resistance. In synchronous motors, the three-phase windings are applied to the stator structure. These windings are supplied separately with currents of equal magnitude but with a 120° phase shift. By using this multi-phase structure, it is possible to create a constantly rotating magnetic field, which circles around the stator. The magnetized rotor then starts to chase this field because now the stator flux rotates around the rotor and the path of least resistance and the point where the flux lines would be parallel changes constantly. The stator current equations for the three-phases are shown below

$$i_{\mathrm{aa}'}(t) = I_{\mathrm{M}} \sin(\omega t) \tag{2.2}$$

$$i_{\mathrm{bb}'}(t) = I_{\mathrm{M}} \sin(\omega t - 120^{\circ}) \tag{2.3}$$

$$i_{\mathrm{cc}'}(t) = I_{\mathrm{M}} \sin(\omega t - 240^{\circ}), \tag{2.4}$$

where $i_{\mathrm{aa}'}$, $i_{\mathrm{bb}'}$ and $i_{\mathrm{cc}'}$ are the currents that flow in the stator coils. The current I_{M} is the magnitude of the coil current, which is the same for all phases but the phase shift is applied inside the sine function. Figure 6 demonstrates the stator structure in this case.

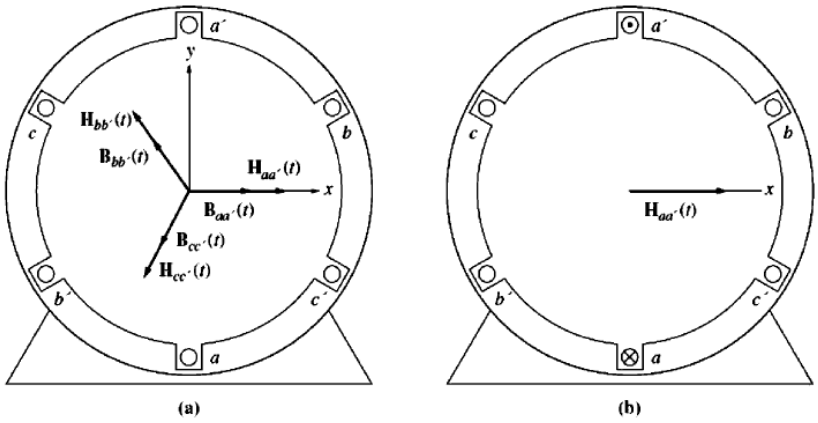

Figure 6. *A simple three-phase stator structure [17, p. 239].*

In Figure 6 b, the current flows into the *a* end of the stator and out of the *a'* end of the stator. This creates a magnetic field strength according to Ampere's law for the direction

oriented to the x-axis (right-hand rule). Magnetic flux density is proportional to magnetic field strength by a factor of permeability. Now the magnetic flux densities for every phase can be expressed as follows

$$\boldsymbol{B}_{\mathrm{aa'}}(t) = B_{\mathrm{M}} \sin(\omega t)\, \hat{\boldsymbol{x}} + B_{\mathrm{M}} \cos(\omega t)\, \hat{\boldsymbol{y}} \tag{2.5}$$

$$\boldsymbol{B}_{\mathrm{bb'}}(t) = B_{\mathrm{M}} \sin(\omega t - 120^{\mathrm{o}})\, \hat{\boldsymbol{x}} + B_{\mathrm{M}} \cos(\omega t - 120^{\mathrm{o}})\, \hat{\boldsymbol{y}} \tag{2.6}$$

$$\boldsymbol{B}_{\mathrm{cc'}}(t) = B_{\mathrm{M}} \sin(\omega t - 240^{\mathrm{o}})\, \hat{\boldsymbol{x}} + B_{\mathrm{M}} \cos(\omega t - 240^{\mathrm{o}})\, \hat{\boldsymbol{y}}, \tag{2.7}$$

where $\hat{\boldsymbol{x}}$ and $\hat{\boldsymbol{y}}$ are the unit vectors in the horizontal and vertical direction and B is the magnetic flux density. Figure 6 a, demonstrates the magnetic flux densities and magnetic field strengths for every phase. When determining the magnetic flux density values at a specific point of time, the resultant magnetic flux density and its direction can be calculated. The net value of the magnetic flux density is calculated below at the time $t = 0$ s

$$\boldsymbol{B}_{\mathrm{net}} = \boldsymbol{B}_{\mathrm{aa'}} + \boldsymbol{B}_{\mathrm{bb'}} + \boldsymbol{B}_{\mathrm{cc'}} = \frac{\sqrt{3}}{2} B_{\mathrm{M}} \left(0.5\hat{\boldsymbol{x}} - 0.5\hat{\boldsymbol{x}} - \frac{\sqrt{3}}{2}\hat{\boldsymbol{y}} - \frac{\sqrt{3}}{2}\hat{\boldsymbol{y}}\right) = -1.5 B_{\mathrm{M}} \hat{\boldsymbol{y}}, \tag{2.8}$$

where it can be seen that the magnitude of $\boldsymbol{B}_{\mathrm{net}}$ is 1.5 times the magnitude of one phase and the direction is -90^{o} in the stator structure of Figure 6. At any time step, the magnetic flux density will have the same value and it will rotate at the same speed. In general, the net value of magnetic flux can be expressed as:

$$\boldsymbol{B}_{\mathrm{net}}(t) = 1.5 B_{\mathrm{M}} \sin(\omega t)\, \hat{\boldsymbol{x}} - 1.5 B_{\mathrm{M}} \cos(\omega t)\, \hat{\boldsymbol{y}}. \tag{2.9}$$

This is true for the most basic version of stator windings and the equation gives the same results as was calculated before at the time $t = 0$ s. However, the electric machine windings are more complex in practice and there are numerous different ways to implement them depending on the application. [17, p. 238-241]

2.6 Stator windings

According to the Faradays law, the changing magnetic flux in the air gap induces a voltage in the stator coils. In the previous section, the flux distribution was sinusoidal so the voltage distribution was also sinusoidal. However, if the flux distribution is not sinusoidal also the induced voltage waveform will be distorted, which reduces the machine performance. Hence, the rotating magnetic field should be designed to be as sinusoidal as possible. In a practical situation, the actual air gap flux consists of a *fundamental component* and *harmonic components*, which are sine waves with a frequency that is multiple times the fundamental frequency. These harmonic components distort the sine wave and therefore they are undesired. However, there are a couple of different stator winding layouts for reducing the harmonic components. [17, p. 707]

2.6.1 Fractional-pitch windings

The *fractional-pitch winding* is one technique to reduce harmonic components. The angular distance between two adjacent poles is called a *pole pitch*. Pole pitch can be expressed in mechanical or electrical angles. In electrical angles, the pole pitch angle is always 180°_{e}. The conversion between electrical and mechanical angles is shown below

$$\theta_{\mathrm{e}} = p\theta_{\mathrm{m}}, \tag{2.10}$$

Where p is the *pole pair number*, Θ_{m} is the mechanical angle and Θ_{e} is the electrical angle [14, p. 6]. In electrical machines, the coils can be arranged as full-pitch coils or as fractional-pitch coils. Figure 7 demonstrates these different coiling types.

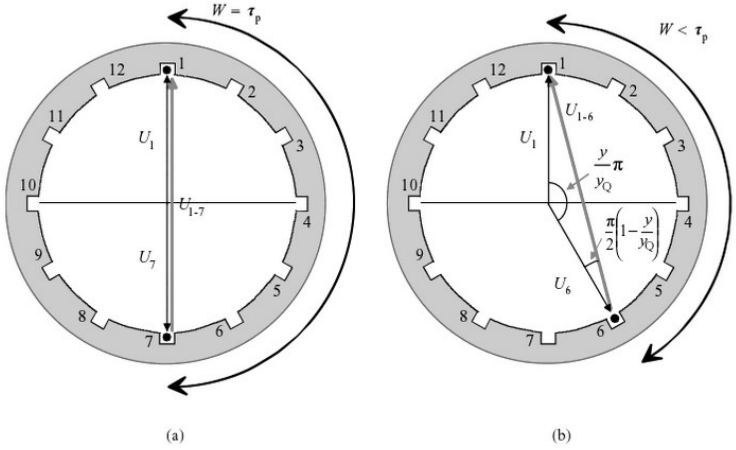

Figure 7. *Full-pitch coil (a) and fractional-pitch coil (b) [11, p. 74].*

In Figure 7, τ_{p} is the pole pitch and w is the coil width. In fractional-pitch winding, it is clearly seen that the coil width w is shorter compared to full-pitch coil where the width of a single coil is the same as pole pitch. The pitch of a fractional-pitch coil in electrical degrees can be calculated with the following two equations

$$\tau_{\mathrm{p}} = \frac{360^{\circ}}{P} \tag{2.11}$$

$$\tau = \frac{\theta_{\mathrm{m}}}{\tau_{\mathrm{p}}} \cdot 180^{\circ}_{\mathrm{e}}, \tag{2.12}$$

where τ_{p} is the pole pitch in mechanical degrees, P is the number of poles, τ is the fractional-pitch in electrical degrees and θ_{m} is the mechanical angle covered by the coil. In the Figure 7 b, the angle θ_{m} is 150° and the pole pitch angle is 180° in mechanical degrees since the machine has two poles. According to (2.12), the fractional-pitch is 150°_{e} electrical degrees. Dividing the fractional-pitch angle with the pole pitch angle it can be seen that the coil width is 5/6-pitch shorter. How this affects to the properties of the electric machine is studied next. The magnetic flux density in the air gap and how it induces the voltage in the wire is inspected in the following equations

$$\boldsymbol{B} = \boldsymbol{B}_{\mathrm{m}} \cos(\omega t - \alpha) \tag{2.13}$$

$$e_{\mathrm{ind}} = (\boldsymbol{v} \times \boldsymbol{B}) \cdot l, \tag{2.14}$$

where the first equation describes the magnetic flux density value at any angle α around the stator. In the second equation, $\boldsymbol{v}$ is the velocity, l is the length, and e_{ind} is the induced voltage of the wire. From these equations, it is possible to derive the general equation for the voltage induced in the wire shown below

$$E_{\mathrm{A}} = \frac{2\pi}{\sqrt{2}} N k_{\mathrm{p}} \phi f, \tag{2.15}$$

where N is the number of turns in a coil, f is the frequency, ϕ is the magnetic flux through the area covered by one pole pitch and k_{p} is the *pitch factor*. For full-pitch windings, the pitch factor is unity but for fractional-pitch windings, the factor is less than unity. Pitch factor can be expressed with the following equation

$$k_{\mathrm{p}} = \sin\left(\frac{v\tau}{2}\right), \tag{2.16}$$

Where τ represents the electric angle spanned by the coil at its fundamental frequency and $v = 1$ for the induced fundamental voltage. When $v = 1$, the equation expresses how the fractional-pitching affects to the fundamental value of the induced voltage and it is always below unity if the winding is fractional-pitched. In addition, by selecting different values than unity to the factor v it is possible to analyze also the induced harmonic voltages. The most significant harmonic components to study in electrical machines are the fifth and seventh harmonics. Third harmonics and its multiples will be insignificant in symmetrical load conditions because the supply circuit is generally three-phase star or delta connection. Figure 8 demonstrates the induced voltage waveform difference between full-pitch and fractional-pitch windings.

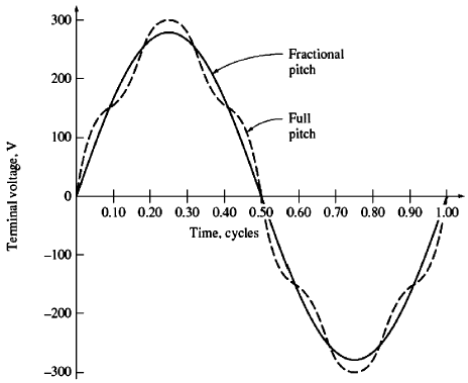

Figure 8. *Comparison of induced voltage waveform between full-pitch and fractional-pitch windings [17, p. 716].*

From Figure 8, it is seen that the fundamental value of voltage is higher in full-pitch winding but the waveform in the fractional-pitch winding is more sinusoidal. The reduced

fundamental value is worth it since there are more advantages to use the fractional-pitch windings. Since the end windings are shorter, the losses decrease in these windings and the amount of copper is reduced, which makes the machine more efficient to use. [17, p. 707-716]

2.6.2 Distributed windings

Since the number of stator slots is limited, the windings are usually stacked in two-layer windings. In two-layer windings there are two different coils in the same stator slot and one coil consists of a large number of turns that are insulated from each other. These coils are then distributed around the stator slots. The spacing between the adjacent stator slots is called *slot pitch* and expressed as γ in electrical or mechanical degrees. Figure 9 demonstrates the differences between the full-pitch and the fractional-pitch in two-layer windings.

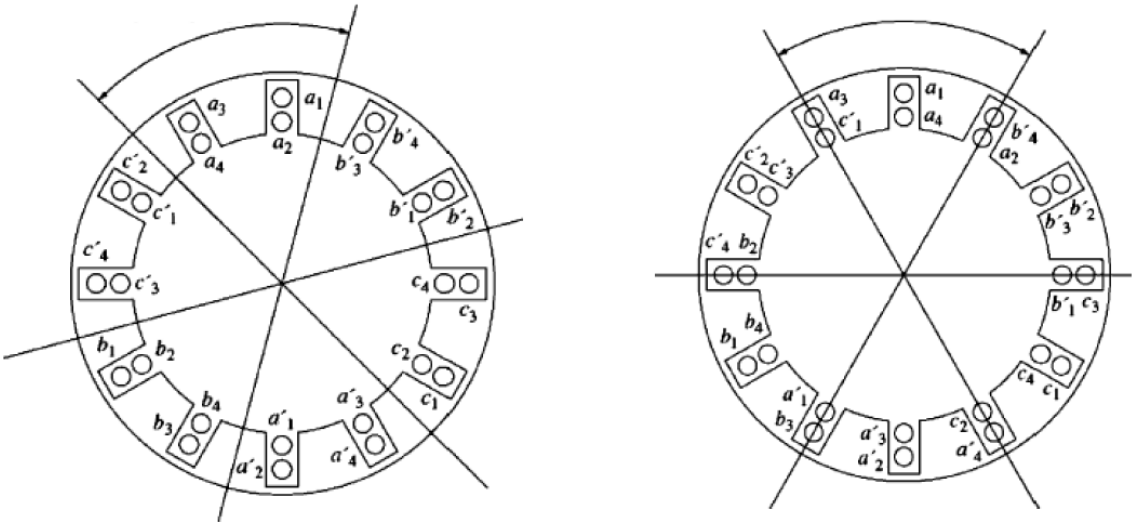

Figure 9. *A double layer full-pitch winding (left) and a fractional-pitch winding (right). Adapted from [17, p. 718-719].*

As can be seen from Figure 9, the difference between the two-layer full-pitch and the fractional-pitch windings is that in the fractional-pitch windings the phases of coils in the individual slot are mixed. The number of slots per pole and per phase in a machine can be calculated with the following equation

$$q = \frac{Q}{2pm}, \tag{2.17}$$

where q is the number of slots per pole per phase, Q is the number of slots in the stator and m is the number of phases. For the machine in Figure 9, $q = 2$ since it has a three-phase supply, one pole pair and, 12 stator slots. The difference between the machines is the winding layout. In fractional-pitch windings, there may be coils of different phases in the same stator slot but in full-pitch windings there can only be coils of the same phase

in the single slot. For example, the bottom slots can be shifted one slot clockwise in relation to top slots in fractional-pitch windings. This kind of winding distribution means that even in the same phase there is some phase shift depending on the slot pitch. Now the induced voltage in the phase belt is the geometrical sum of the phase-shifted voltages, which reduces the fundamental value of the induced voltage. The *distribution factor* is expressed with the following equation:

$$k_{\mathrm{d}} = \frac{\sin\left(\frac{q\gamma}{2}\right)}{q\sin\left(\frac{\gamma}{2}\right)}. \tag{2.18}$$

The winding distribution is used since in practice for high-powered electrical machines it is not possible to induce high enough voltages in coils if they are not distributed to multiple slots and connected to each other with serial connections. Correspondingly, the currents can be increased in the windings with parallel connections. The distribution of coils also makes it easier to install physically more windings in a given machine. [17, p. 716-720]

To get the total *winding factor* k_{w} the distribution factor is combined with the pitch factor. The winding factor and the updated equation for the induced phase voltage are given below:

$$k_{\mathrm{w}} = \sin\left(\frac{\nu\theta_{\mathrm{e}}}{2}\right) \cdot \frac{\sin\left(\frac{q\gamma}{2}\right)}{q\sin\left(\frac{\gamma}{2}\right)} = k_{\mathrm{p}}k_{\mathrm{d}} \tag{2.19}$$

$$E_{\mathrm{A}} = \frac{2\pi}{\sqrt{2}} N k_{\mathrm{w}} \phi f. \tag{2.20}$$

There are no universal solutions for electric machine windings and the windings need to be designed depending on the application. When the application is known the winding factor can be designed to produce the most efficient windings. In short, the pitch factor is used to reduce the harmonic components of the induced voltage, which produces more sinusoidal voltage waveforms. In addition, the amount of copper is reduced due to shorter end windings. The windings are distributed to allow higher induced voltages and power values. The number of stator slots is limited in the machine, which requires dividing one phase into several different stator slots to gain higher induced voltages. Both of these methods reduce the fundamental induced voltage value but the advantages are far more beneficial. [17, p. 721-725]

2.7 Frequency converter supply

Permanent magnet synchronous motors are often supplied with frequency converters since it allows a very accurate speed control and the possibility to start the motor without the additional help. Without the frequency converter, the rotating speed of PMSM is the same as the synchronous frequency in the supplying network according to (2.1) [14, p.

129-130]. However, the frequency converter applies higher frequency and more harmonic components compared to the pure sinusoidal voltage, which in turn increases losses. The principle of the frequency converter is to create the supply voltage to the machine by controlling the power transistor or thyristor switches in the supply circuit. With this structure, the supplying frequency can be varied according to the frequency converter switching frequency and since the rotating speed is proportional to the frequency, the motor speed can be controlled [18, p. 1]. In this chapter, a basic principle of the frequency converter is shown.

The basic frequency converter consists of a rectifier, intermediate circuit and inverter. Figure 10 demonstrates the basic structure of a frequency converter.

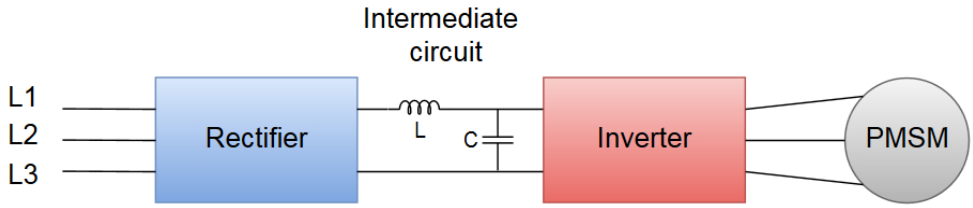

Figure 10. *The Basic structure of a frequency converter. Adapted from [19, p. 91, 94].*

On the left of Figure 10, the L1, L2 and L3 are the three phase lines of a supplying electric network. Commonly a 6-pulse rectifier is used to convert the three-phase AC supply voltage to direct current (DC) voltage. The rectified DC voltage value can be calculated with the following equation

$$V_{\mathrm{dc}} = \frac{3\sqrt{2}}{\pi} V_{\mathrm{LL}} \approx 1.35 V_{\mathrm{LL}}, \tag{2.21}$$

where V_{dc} is the rectified DC voltage and V_{LL} is the line-to-line voltage. V_{LL} is then supplied to the intermediate circuit. The DC voltage in the intermediate circuit is then converted back to AC voltage, which supplies the stator windings of the permanent magnet synchronous motor. The difference is that now the motor supplying frequency is isolated from the supplying electric grid, which allows the flexible speed control of the motor. Inverter topology varies depending on the intermediate circuit. If there is only a capacitor in the circuit it is called a voltage source inverter and if there is only an inductor in the circuit it is called a current source inverter. The former is more common since it can be used in a wide variety of applications but the latter is typically used in high-powered applications. [19, p. 90-95]

In this thesis, the interest is only in the inverter side since it controls the motor. A structure of an inverter is shown in Figure 11.

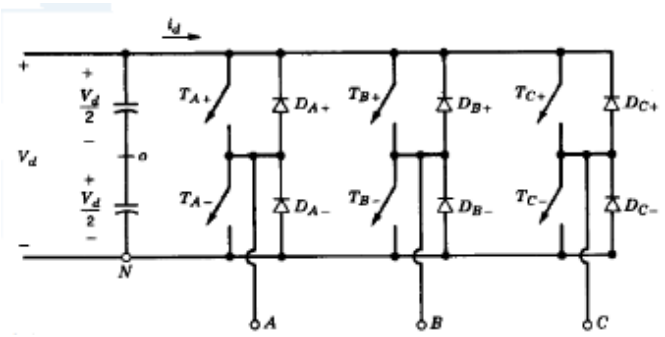

Figure 11. *Three-phase Inverter structure [20, p. 130].*

Figure 11 shows a two-level three-phase inverter structure, which uses insulated-gate bi-polar transistors. The inverter has 8 (2^3) different switching combinations. With these combinations, it is possible to create seven different voltage vectors, which include six equal magnitude but different direction voltage vectors and two zero voltage vectors. These switching combinations are defined by sine-triangle comparison. For every phase, the switch states are defined by comparing sinusoidal waves that are in 120^o phase shift to each other to the same triangle wave with the defined switching frequency. The switches are connected to the positive terminal when the sine wave is higher than the triangle wave and a negative terminal when the sine wave is lower than the triangle wave. This control method is demonstrated in Figure 12.

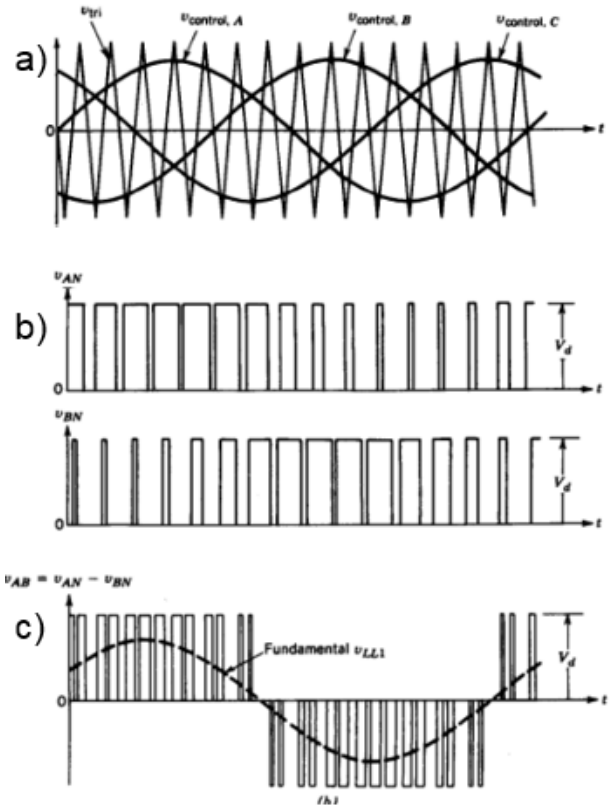

Figure 12. *Inverter switching pattern based on the sine-triangle comparison [20, p. 131].*

As can be seen from Figure 12, the switches are conducting when the control signal is higher than a triangle wave. The idea of the control method is to break the DC voltage to pulses with different durations and widths and when the pulses are integrated they create a motor supply voltage that resembles a sinusoidal signal. This kind of control method is called *pulse width modulation*. Another method is pulse amplitude modulation but PWM is the most common method since it does not require additional circuitry. [19, p. 88]

The phase voltages in Figure 12 b are measured with respect to the negative DC bus. If the voltages would be measured with respect to 0 V reference point then the pulse values would change either $+\frac{1}{2}V_{\mathrm{dc}}$ or $-\frac{1}{2}V_{\mathrm{dc}}$. We obtain the line-to-line values between A and B phases by subtracting the phase B value from the phase A value. Now the pulses in line-to-line are twice as high ($\pm V_{\mathrm{dc}}$) compared to the phase values. The fundamental V_{LL1} is obtained by taking fast Fourier transform of the signal V_{AB} or by using the following equation

$$\left(\hat{V}_{\mathrm{Ao}}\right)_1 = \frac{\hat{V}_{\mathrm{control}}}{\hat{V}_{\mathrm{tri}}} \cdot \sin(\omega_1 t) \cdot \frac{V_{\mathrm{dc}}}{2}, \tag{2.22}$$

where $\left(\hat{V}_{\mathrm{Ao}}\right)_1$ is the voltage fundamental, the first term is the amplitude modulation ratio, ω_1 is the fundamental angular frequency and V_{dc} is the intermediate circuit DC voltage. The harmonic components of the voltage can be calculated by multiplying the angular frequency values by integers. [20, p. 108].

The frequency converter properties can be defined with two different modulation ratios. These ratios are the amplitude modulation ratio and frequency modulation ratio. They are defined as follows

$$m_{\mathrm{a}} = \frac{\hat{V}_{\mathrm{control}}}{\hat{V}_{\mathrm{tri}}} \tag{2.23}$$

$$m_{\mathrm{f}} = \frac{f_{\mathrm{s}}}{f_1}, \tag{2.24}$$

where $\hat{V}_{\mathrm{tri}}$ is the amplitude of the triangular signal, $\hat{V}_{\mathrm{control}}$ is the amplitude of the control signal, f_{s} is the switching frequency and f_1 is the desired fundamental frequency of the inverter. The amplitude modulation index describes the relationship between the control signal and triangle signal peak values. The amplitude modulation index value affects to the output voltage value of the inverter. If m_{a} is lower than one, the output voltage is linearly dependent of the amplitude modulation ratio. If the amplitude modulation index is higher than one, the output voltage is not linearly dependent of amplitude modulation ratio anymore and this state is called overmodulation. Usually, the triangle signal is kept constant. The frequency modulation index describes the relationship between the switching frequency and the desired fundamental frequency of the converter. [19, p. 89]

3. HIGH-SPEED PMSMS

The high-speed electrical machines have been studied over the last decades. The demand is coming from the industry. High-speed electric machines have several advantages compared to the common low-speed machines. With the same power rating, the high-speed machine has a smaller size, weight and higher torque. In addition, the use of high-speed can eliminate the gearbox, which is used in mechanical devices. With the use of active magnetic bearings, the system will also be oil-free. This reduces the maintenance of the high-speed electric machines. These machines have advantages in numerous applications starting from grinding and milling to the aerospace and compressor applications. However, there are some disadvantages compared to the low-speed machines. Especially the rotor structure is problematic since the operating temperature and the rotor vibrations will be higher compared to the low-speed machines. [21, p. 2]

This chapter gives an overview of the high-speed technology mainly used in PMSMs. The focus is on the losses but also the basic design challenges of the high-speed technology are presented.

3.1 Definition of high speed

High-speed technology means an arrangement where the electric machine is connected to the actuator without the gearbox and the rotation speed of the electric machine is significantly higher compared to the synchronous speed of the two poles electric machine connected to a 50 Hz electric grid (3000 rpm). Typically the speed is higher than 10 000 rpm [22, p. 20]. Another way to define the high-speed is to calculate the tip speed of the rotor surface according to the equation

$$V_{\mathrm{tip}} = 2\pi N \frac{D_{\mathrm{r}}}{2} = \pi N D_{\mathrm{r}} \,, \tag{3.1}$$

where V_{tip} is the tip speed, N is the rotational speed of the rotor and D_{r} is the rotor outer diameter. In this way, also the size of the machine is taken into account because the rotor outer diameter is included in the equation. In literature, the high-speed is usually defined with rated rotational speed values but also the power of the machine should be taken into account. Otherwise, the arbitrary high speeds can be achieved by just scaling down the machine. That is why the only criterion for high speed should not be the rotational speed. [21, p. 2]

3.2 The losses in high-speed PMSMs

In this thesis, the focus is on the eddy current losses of the rotor. However, for understanding the loss components of the electric machine the general analytic loss models are introduced. The losses in the electric machine consist of stator losses, rotor eddy current losses, and windage losses. The stator losses are further divided into copper and iron losses. The rotor losses are low compared to the machine total losses but the heat is harder to remove from the rotor surface compared to the stator surface. Heat removal is important to ensure reasonable working temperatures for the rotor components, especially for the permanent magnets. Rotor losses consist mainly of space and time harmonics. Windage losses are mainly a high-speed problem and consist of friction between the air and the rotating rotor. [23, p. 1]

3.2.1 Eddy currents

Eddy currents are a direct result of Lenz's law. It states that the induced current in a conductor always opposes the changing magnetic flux that generated it. Lenz's law is shown below

$$E_{\text{emf}} = -\frac{\partial \phi}{\partial t}, \tag{3.2}$$

where E_{emf} is the electromotive force and ϕ is the magnetic flux. According to (3.2), eddy currents start flowing when the conductor is exposed to a changing magnetic field. The changing field can be produced by moving a static magnetic field source near a conductor or by creating a time-variating field near the conductor. The variating field creates short eddy current loops inside the conducting material. These loops resemble the vortices in fluid dynamics caused by the turbulence, hence the name eddy current. Figure 13 demonstrates the induced eddy currents in a conducting body.

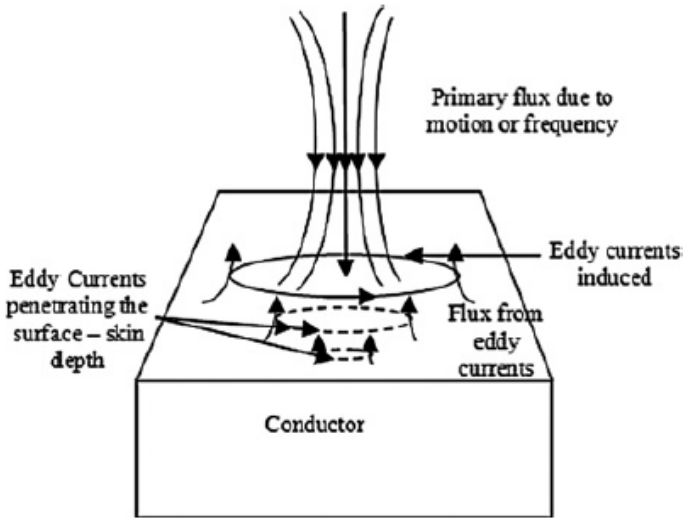

Figure 13. *Induced eddy currents in a conducting body [24, p. 744].*

There are two major effects of eddy currents. First, these eddy currents create their own magnetic field, which opposes the main field. This phenomenon is used in eddy current braking. Secondly, these additional current loops heat the conducting body. The heating is used as an advantage in induction heating but it is not a desirable effect in electrical machines. [24, p. 744]

3.2.2 Stator losses

The copper losses of the stator consist of resistive losses and stray load losses. The resistive copper losses can be calculated with the following equation

$$P_{\mathrm{Cu}} = mI^2R_{\mathrm{s}}, \tag{3.3}$$

where P_{Cu} is the copper losses, m is the phase number, I is the stator current and R_{s} is the stator winding resistance. These losses can be significant if the supply current and winding resistance is high. It should be noted that the copper losses depend on the temperature and they are calculated at the expected temperature. [23, p. 1]

Stray losses are divided into two separate components, namely skin effect and proximity effect. The skin effect is related to the eddy currents in a single conductor. When a single conductor is supplied with AC current, the induced eddy currents force the supply current to a thin surface layer (skin) [25, p. 23-27]. The skin depth demonstrates the distance it takes for electromagnetic wave amplitude to dampen by a factor of $1/e$ where e is mathematical constant (Euler's number). In other words, the skin depth carries 63 % of the total current flowing in the conductor [25, p. 23]. The skin depth distance can be calculated with the following equation

$$\delta = \sqrt{\frac{2}{\omega\mu\sigma}}, \tag{3.4}$$

where δ is the skin depth, ω is the angular frequency and σ is the electric conductivity of the material. As we can see from (3.4) the electric conductivity and the AC current frequency has a significant effect on skin depth. The skin depth effect is demonstrated in Figure 13. Due to the skin effect, the wire size in the conductor is designed so that the radius of the wire is significantly larger compared to the skin depth. [23, p. 1]

As described earlier, the stator windings are distributed in the stator slots. In the stator slots, there are several conductors located close to each other. These nearby conductors induce eddy currents to each other due to changing magnetic fields. The effect is called as a proximity effect and it can be estimated with the following equation

$$P_{\mathrm{stray}} = P_{\mathrm{Cu}}(k_{\mathrm{d}} - 1), \tag{3.5}$$

where P_{stray} is the proximity effect losses, P_{Cu} is the copper losses and k_d is the ratio of effective AC resistance versus DC resistance. The proximity effect losses can be significant in high-speed frequency converter motor drives since the high supply frequency increases the proximity losses. There are two common stator wire structures to reduce proximity losses: Litz wire and transposed wire bundles [21, p. 3-4]. [23, p. 1]

The iron losses consist of three basic loss components, which are hysteresis losses, eddy current losses and excess eddy current losses. *Eddy current losses* are described in the previous chapter. The *hysteresis losses* can be described by studying the hysteresis loop shown in Figure 14.

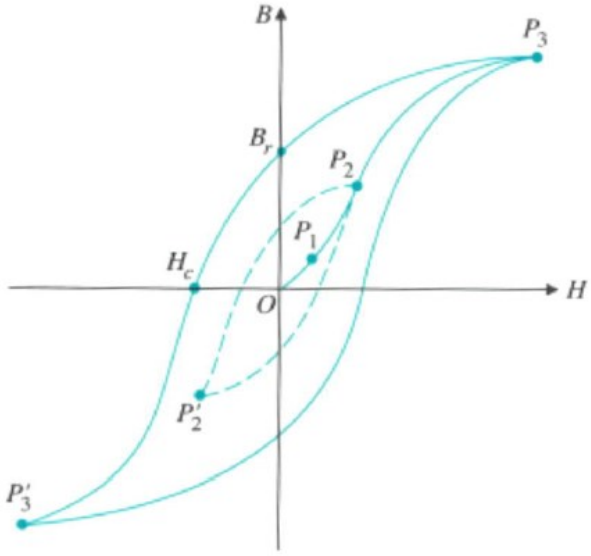

Figure 14. *Hysteresis loop of a ferromagnetic material [10, p. 13].*

Figure 14 describes the common hysteresis loop of a ferromagnetic material. Commonly in the ferromagnetic materials, the magnetic flux density is proportional to the external magnetic flux density. The curve is called a *BH* curve. At the start (origin) the exterior magnetic field is zero and when the exterior field is increased the magnetic flux density increases. The different Weiss domains will start to unify at the external field direction. Before P_1 point, this effect is reversible but after this point, the effect is non-reversible as can be seen from Figure 14. After the point P_2, the hysteresis curve will not follow the original path. This is due to the magnetization *M* of the material and the Barkhausen effect. At the Point P_3, the material is saturated, in which case all the Weiss regions in the material are directed at the external field direction. The x- and y-axis intersection points describes the coercive field strength H_c and the remanence flux density B_r respectively. The hysteresis losses are integrated from the hysteresis loop so the losses are proportional to the surface of the hysteresis loop. The whole hysteresis loop is obtained if the exterior magnetic field is of AC type. [10, p. 9:13-9:14]

The *excess eddy current losses* are lesser-known loss mechanism. These losses originate from the transition areas (Bloch walls) between different Weiss domains. In the transition areas, the magnetization direction of one Weiss domain changes in the direction of the adjacent Weiss domain. Among other things, the magnetization state of the material consists of the motion of these transition areas in relation to an applied exterior field. In this case, the magnetization of the material changes only in or near these transition areas. The magnetization has to change significantly compared to the average change in the material in or near these transition areas to be notable. [26, p. 3430]

The iron losses are usually estimated together with a single equation called a Steinmetz equation. The total iron losses can be calculated with the following equation for sinusoidal excitation

$$P_{\text{iron}} = K_{\text{h}} B^2 f + K_{\text{c}} (Bf)^2 + K_{\text{e}} (Bf)^{3/2}, \tag{3.6}$$

where K_{h}, K_{c} and K_{e} are the coefficients for the hysteresis losses, classical eddy current losses and excess eddy current losses respectively. B is the peak flux density and f is the frequency. The coefficients can be obtained from manufacturers data sheets or material test data using the curve fitting for the iron loss data. Equation (3.6) applies only to the sinusoidal supply and for the frequency converter drives, the equation needs to be modified because of the harmonic components. [23, p. 2]

3.2.3 Rotor losses

The rotor losses are not significant compared to the stator losses but the heat is harder to remove from the rotor compared to the stator. The heat removal is important to ensure reasonable working temperatures for the rotor. The high working temperature affects negatively to the permanent magnet properties. The induced eddy currents in the rotor can be divided into three separate categories, which are slot, space and time harmonics. Slot harmonics consists of stator slots, which are divided across the stator structure. Space harmonics are created due to windings magnetomotive force and time harmonics are related to the PWM supply. The general eddy current losses in the rotor can be estimated with the following equation

$$P = \int_V \sigma \|\boldsymbol{E}\|^2 dV = \int_V \frac{\|\boldsymbol{J}\|^2}{\sigma} dV, \tag{3.7}$$

where $\|\boldsymbol{E}\|$ is the normal component of the electric field strength, $\|\boldsymbol{J}\|$ is the normal component of the current density and σ is the electric conductivity of the material. As can be seen from the equation the induced eddy currents in the rotor are dependent on the material volume, current density and the conductivity of the material. [23, p. 2]

There are several common methods to reduce the induced eddy currents in the rotor. The slot opening can be reduced, which reduces the slot harmonics and therefore no-load

losses. In addition, the increase of the air gap between the stator and the rotor will reduce the no-load losses. The increase of the phase belt number and fractional slot winding will decrease the space harmonic losses. [23, p. 2]

In high-speed surface mounted PMSMs, the rotor is usually covered with a sleeve. The sleeve is a part that is installed around the surface of the rotor to ensure that the magnets retain on the rotor surface. The sleeve should be chosen carefully since it significantly affects the cooling and efficiency of the PMSM. Commonly used sleeve materials are, for example, carbon fiber, stainless steel, copper and copper iron alloy. [21, p. 5]

3.2.4 Windage losses

Windage losses depend on the fluid that is used in the air gap between the stator and the rotor. Usually, the air gap consists of air but various gases can also be used. The fluid flow in the air gap creates friction, which resists the rotor rotation. The amount of friction depends on the shaft rotational speed, fluid density, temperature and pressure for example. Windage losses can be estimated with the following equations

$$Re = 2\pi N r \frac{\rho}{\mu}\phi = \omega r \frac{\rho}{\mu}\phi \tag{3.8}$$

$$\frac{1}{\sqrt{C_\mathrm{d}}} = 2.04 + 1.768 \ln\left(Re\sqrt{C_\mathrm{d}}\right) \tag{3.9}$$

$$P_\mathrm{w} = C_\mathrm{D}\pi\rho\omega^3 r^4 l, \tag{3.10}$$

where Re is the Reynolds number, C_d is the skin friction coefficient for turbulent flow, N is the rotational speed, ρ is the density of fluid μ is the kinematic viscosity of cooling media, r is the radius of the rotor, l is the length of the rotor and ϕ is the air gap length. In high-speed machines, the windage losses can be very high since the shaft rotational speed ω is of a third power. In addition, the surface roughness of the rotor surface and the stator tooth affects to the windage losses. [23, p. 3]

3.3 Bearings of high-speed electric machines

The higher rotational and tip speeds in high-speed machines require more advanced bearings compared to the common electric machines. The position accuracy is not high enough in a standard journal or ball bearings. Another problem is the centrifugal loading, which rises with the square of the rotational speed and lowers the load capacity of the bearings. A common method to overcome these problems is to use more advanced mechanical bearings or contactless bearings. The mostly used bearings that are used in high-speed electric machines are advanced ball bearings, air bearings and active magnetic bearings. The bearing choice depends on the required speed, accuracy, cost and durability of the designed electric machine. [9, p. 118-119]

These three bearings introduced before are the most used bearings in the high-speed machines. All the advantages and disadvantages of these different bearings are compared in Table 2.

Table 2. *Comparison of different bearings. Adapted from [9, p. 125].*

Ball bearings	***Air bearings***	***Active magnetic bearings***
Advantages: + Low cost + Robust	Advantages: + No friction/wear + Ultra-precision + High stiffness + Low maintenance	Advantages: + No friction/wear + Zero contamination + No maintenance + Adjustable force, damping + Positioning during rotation + Modular design + Operate in harsh settings + Facilitate monitoring
Disadvantages: – Temperature limited – Wear – Need lubricant – Need maintenance	Disadvantages: – Require flawless geometry – Need preloading – Susceptible to dirt, temperature	Disadvantages: – Complex and expensive – Low reliability – Require control – Require constant power supply, sensors, and electronics

The mechanical ball bearings are still very common in high-speed machines. This is a result of the robustness and low costs of the ball bearings. The main disadvantages are related to the operating temperature since the friction in high speed increases the temperature significantly. The friction also increases wear of the bearings and shortens the lifespan of the bearings. For very high-speeds the ball bearing materials need to be improved, which consists usually of reduction of the size of the balls and the use of ceramic balls. The operation speed of the ball bearings can reach up to 500 000 rpm [21, p. 6]. [9, p. 119-122]

The air bearings are contactless bearings. In contactless bearings the rotor is held at a place without mechanical contact. In air bearings, this is done with air pressure. The air

pressure is generated by the rotor (dynamic and foil) or with an external supply (static). Air bearings also require very small air gaps with a flawless geometry, which enables very accurate motion accuracy. Air bearings are very attractive for precision machinery. The rotational speeds in air bearings can reach up to 700 000 rpm and the temperature can reach up to 650 ºC. [9, p. 119-122], [21, p. 6]

The active magnetic bearings are also contactless bearings. In this case, the rotor and the shaft is levitating in place by using magnetic forces. The operation of active magnetic bearings is purely contactless and frictionless, which means that no lubricants or contamination is required. The active magnetic bearings do not require constant maintenance. However, the active magnetic bearings are very complex and expensive electromechanical systems. [9, p. 123-124]

3.4 Rotor dynamic challenges

For high-speed electric machines, the rotor vibrations are significantly larger compared to the low-speed electric machines and need to be considered in the design. If the design is not done properly, different rotor vibrations will be a problem. The two different rotor vibrations are resonant vibration and self-excited vibration. Resonant vibrations happen when the resonant frequencies coincide with the speed of the rotor. Self-excited vibrations occur when certain threshold speed is passed. After this, the rotation will be unstable. The threshold speed depends on the intrinsic properties of the system. [21, p. 8]

The rotor dynamics are an important part of designing a high-speed electric machine and it has been studied by many researchers. They have found that the rotor has three different bending and vibration modes, which will occur at three natural frequencies. These frequencies can be calculated with the following equation

$$\omega_{\mathrm{n}} = a_{\mathrm{n}}\sqrt{\frac{EI}{\mu_1 l^4}}, \tag{3.11}$$

where E is Young's modulus, μ_1 is the mass in per unit length, l is the axial length of the rotor, I is the inertia of the rotor and a_{n} is the numerical constant calculated by the Rayleigh method. The three vibration modes for high-speed PMSM are investigated in [21, p. 8] and demonstrated in the Figure 15.

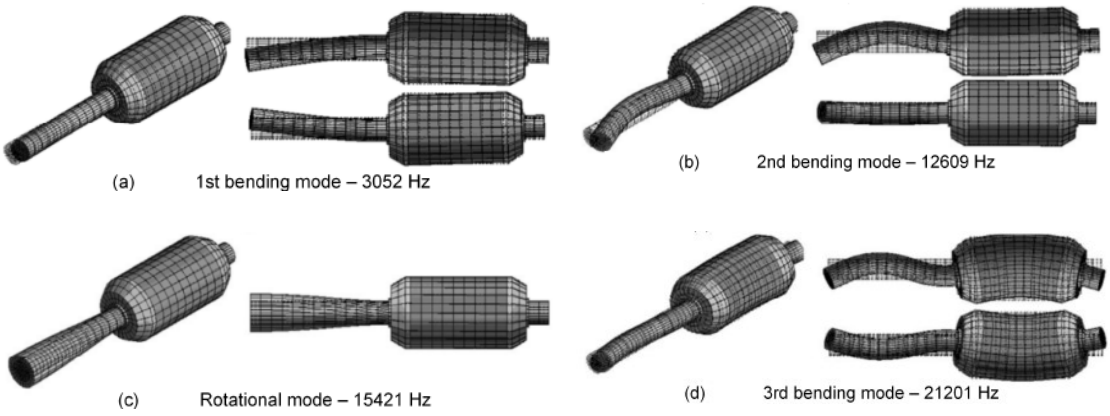

Figure 15. *High-speed PMSM rotor vibrations. Adapted from [21, p. 8].*

Based on the resonance analysis the rotation speed range of the rotor should be designed so that the range is placed reasonably apart from the resonant speed and ensure that the speed will not reach the threshold speed. Overall several methods can be used to modify the resonant frequencies. These consists of increasing the rotor diameter, reducing bearing span, increasing wall thickness, adding third center bearing and reducing machine length. However, some compromises are often required depending on the application. [21, p. 8]

3.5 Power electronic challenges

According to (2.1), the rotation speed and the frequency depend on each other and the pole pair number, which means that for high-speeds the high frequency is required since the gearbox is not used in high-speed applications. The power electronic components switching frequency has to be exceptionally high in high-speed applications. The traditional Si semiconductors operating area is around 20–30 kHz. At high enough speeds, the traditional semiconductors cannot switch fast enough and this will induce additional harmonic components. In addition, the inductances are lower due to the number of turns in the stator windings being lower in the high-speed electric machines, which increases the current ripple compared to a low-speed machine. [21, p. 9-10]

A couple of different methods can be used to meet these challenges. First, the low pass filter can be added to the electric machine input. Unfortunately, also the size and the costs of the system will be increased. Another method is to use multi-level inverters, which will increase the number of switches but reduce the harmonic components. [21, p. 9-10]

4. ELECTROMAGNETIC MODEL

This chapter introduces the electromagnetic modeling basics. At first, it introduces Maxwell's laws, which are the fundamental equations that can describe any electromagnetic phenomena. Using auxiliary functions called potentials with Maxwell's laws it is possible to derive formulations for eddy currents in 2D- and 3D-domain. Eddy current calculations can be approximated using 2D-simulations but it is mainly a 3D-problem. After eddy current formulation, the equation is discretized using Galerkin's weighted residual method. This method discretizes the eddy current formulations so that the solution can be obtained as an approximation using numerical methods. Numerical methods divide the simulation domain into finite elements. In 2D, usually the linear triangular elements are used to discretize the simulation domain. At last, defining the correct boundary conditions are necessary for any finite element simulation to succeed.

4.1 Maxwell's equations

The equations developed by James Clerk Maxwell are commonly known as the most important scientific result of the 19th century. Maxwell continued the work of some notable scientists i.e. Andre Marie Ampere and Michael Faraday. In 1865, Maxwell published a scientific article *A dynamical theory of the electromagnetic field* which introduced his equations for the first time [27, p. 47]. Maxwell did not know the modern vector analysis so describing his whole theory needed 20 equations. By the end of 1870's Oliver Heaviside developed more comprehensive equations using vector analysis and the 20 equations were reduced to four. These four equations are the basis of the whole electromagnetic theory. Before introducing the equations, Table 3 introduces the common variables used in these equations. [10, p. 1:9-1:10]

Table 3. *Common variables in electromagnetism. Based on [2, p. 2:1].*

Name	***Symbol***	***Unit***
Electric field strength	$\boldsymbol{E}$	V/m
Magnetic field strength	$\boldsymbol{H}$	A/m
Electric flux density	$\boldsymbol{D}$	C/m^2
Magnetic flux density	$\boldsymbol{B}$	T (Vs/m^2)
Electric current density	$\boldsymbol{J}$	A/m^2
Electric charge density	ρ	C/m^3

In Table 3, there are five vectors and one scalar variable. Using these variables, we can write the four Maxwell equations in integral form

$$\oint_{\sum} \boldsymbol{D} \cdot dS = \int_{\tau} \rho d\tau \tag{4.1}$$

$$\oint_{\sum} \boldsymbol{B} \cdot dS = 0 \tag{4.2}$$

$$\oint_{C} \boldsymbol{E} \cdot dl = -\int_{S} \frac{\partial \boldsymbol{B}}{\partial t} \cdot dS \tag{4.3}$$

$$\oint_{C} \boldsymbol{H} \cdot dl = \int_{S} \boldsymbol{J} \cdot dS + \int_{S} \frac{\partial \boldsymbol{D}}{\partial t} \cdot dS, \tag{4.4}$$

where τ is a volume, $\sum$ is the closed surface boundary of the volume τ, S is an open surface and C is the contour of the surface S. These equations are written in the dynamic state but the static form can be expressed by setting time derivatives to zero. Figure 16 illustrates the integral form of Maxwell's equations in open surface S (left) and volume τ (right). [27, p. 69]

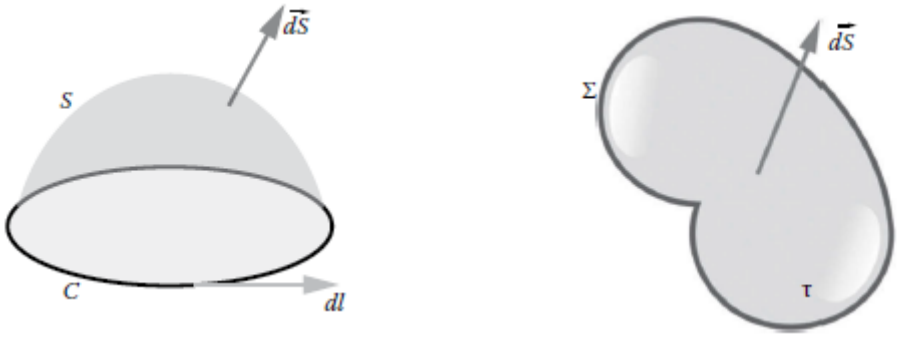

Figure 16. *Demonstrating Maxwell's equations in integral form. Adapted from [27, p. 69].*

First two laws are Gauss's laws for electric and magnetic fields. Latter two are Faraday's law of induction and Ampere's circuital law with Maxwell's addition. Maxwell's addition is the last term in (4.4), which describes the displacement current. According to (4.4), also the changing electric field produces a magnetic field. However, if the problem does not include the propagation of electromagnetic waves the displacement current is negligible because the current density is significantly larger compared to the displacement current at all frequencies. [2, p. 2:1-2:3]

The finite element method uses partial differential equations to solve a particular case. Therefore, the differential forms of Maxwell's equations are required. The following two integral theorems are used

$$\oint_{\sum} \boldsymbol{F} \cdot dS = \int_{\tau} (\nabla \cdot \boldsymbol{F}) d\tau \tag{4.5}$$

$$\oint_C \boldsymbol{F} \cdot dl = \int_S (\nabla \times \boldsymbol{F}) dS, \tag{4.6}$$

where the former equation is Gauss's theorem and the latter is Stokes's theorem. Using the Gauss's theorem to (4.1) and (4.2) and Stokes's theorem to (4.3) and (4.4), the differential forms of the Maxwell's equations can be derived:

$$\nabla \cdot \boldsymbol{D} = \rho \tag{4.7}$$

$$\nabla \cdot \boldsymbol{B} = 0 \tag{4.8}$$

$$\nabla \times \boldsymbol{E} = -\frac{\partial \boldsymbol{B}}{\partial t} \tag{4.9}$$

$$\nabla \times \boldsymbol{H} = \boldsymbol{J} + \frac{\partial \boldsymbol{D}}{\partial t}. \tag{4.10}$$

These four differential equations can be used in the finite element method. Aforementioned equations summarize electrical engineering because they can be used to describe any electromagnetic phenomena. [28, p. 4-7]

The constitutive relations are also necessary to solve Maxwell's differential equations. These three equations describe the property of the medium

$$\boldsymbol{D} = \varepsilon \boldsymbol{E} = \epsilon_0 \varepsilon_r \boldsymbol{E} \tag{4.11}$$

$$\boldsymbol{B} = \mu \boldsymbol{H} = \mu_0 \mu_r \boldsymbol{H} \tag{4.12}$$

$$\boldsymbol{J} = \sigma \boldsymbol{E}, \tag{4.13}$$

where ε is permittivity, μ is permeability and σ is the electric conductivity of the medium. Depending on the simulated case, these values are not necessary constants. For example, in ferromagnetic materials the *B*-*H* curve is not linear, which means that we have to iterate the FEM solution. Additionally, if the medium is highly anisotropic the permittivity and permeability are dealt as tensors. The values of permittivity and permeability in free space are $\epsilon_0 = 8.854 \cdot 10^{-12}$ F/m and $\mu_0 = 4\pi \cdot 10^{-7}$ H/m. [2, p. 2:1]

At last, the differential equations require special interface conditions to be solved. These conditions need to be applied at the interface of two different materials. For two different materials, which have a common interface, there are four different rules as follows:

$$(\boldsymbol{D}_1 - \boldsymbol{D}_2) \cdot \boldsymbol{n} = \rho_s \tag{4.14}$$

$$(\boldsymbol{B}_1 - \boldsymbol{B}_2) \cdot \boldsymbol{n} = 0 \tag{4.15}$$

$$(\boldsymbol{H}_2 - \boldsymbol{H}_1) \times \boldsymbol{n} = \boldsymbol{J}_s \tag{4.16}$$

$$(\boldsymbol{E}_2 - \boldsymbol{E}_1) \times \boldsymbol{n} = 0. \tag{4.17}$$

The first rule states that if the interface has surface charges then the $\boldsymbol{D}$ component is discontinuous by the amount of charge ρ_s. Next, the normal component of $\boldsymbol{B}$ is always continuous on the interface. Third rule states that the tangential component of $\boldsymbol{H}$ is discontinuous by the amount of surface current density $\boldsymbol{J}_s$. At last, the tangential component of $\boldsymbol{E}$ is always continuous on the interface. Additionally, we can see that if there is no surface charge or current density in the interface of (4.14) and (4.16) the normal component of $\boldsymbol{D}$ and the tangential component of $\boldsymbol{H}$ are continuous. [29, p. 72]

4.2 Potentials

Potentials are auxiliary scalar and vector functions for reducing the mathematical complexity of the solution. In electromagnetics, the most successful functions are the *electric scalar potential* and the *magnetic vector potential*. [28, p. 9]

Electric scalar potential can be derived by studying the electric field in a static case. In static case, the time-varying magnetic flux and the displacement current can be neglected. Now Maxwell's equations (4.7) and (4.9) can be modified as follows:

$$\nabla \cdot \boldsymbol{D} = \nabla \cdot (\varepsilon \boldsymbol{E}) = \rho \tag{4.18}$$

$$\nabla \times \boldsymbol{E} = 0. \tag{4.19}$$

The latter term means that the electric field is irrotational. According to the first null identity of vector calculus, the curl of a scalar function gradient is always equal to zero $(\nabla \times (\nabla f) = 0)$. Using this statement the electric field vector function can be replaced as a scalar function and (4.18) can be simplified as shown below

$$\boldsymbol{E} = -\nabla \varphi \tag{4.20}$$

$$-\nabla \cdot (\varepsilon \nabla \varphi) = \rho, \tag{4.21}$$

where φ is the electric scalar potential. The resulting scalar function is easier to solve than vector function. [28, p. 9-10]

A similar procedure is done for deriving the magnetic vector potential $\boldsymbol{A}$. In the static magnetic field, Maxwell's equation (4.8) states that the magnetic field is divergence free (solenoidal). This is more complicated than the previous case because of the divergence term. Using the second null identity of vector calculus, it is known that the divergence of a vector function curl is always zero $(\nabla \cdot (\nabla \times \boldsymbol{f}) = 0)$. Magnetic flux density can now be represented using magnetic vector potential as follows:

$$\boldsymbol{B} = \nabla \times \boldsymbol{A} \tag{4.22}$$

$$\nabla \times \boldsymbol{B} = 0. \tag{4.23}$$

Additionally, (4.23) describes a special Coulomb's condition that is required to define unambiguously the vector potential. These equations are used in the next chapter to define the equations for solving eddy currents. [28, p. 12-12], [2, p. 2:9-2:10]

4.3 Eddy current formulations

Eddy current formulations can be derived using Maxwell's laws (4.9) and (4.10). In (4.10) the changing electric flux density term can be ignored because it is negligible compared to the current density term in electrical machine applications. The $\boldsymbol{A} - \emptyset$ formulation uses the potentials to define eddy currents. In magnetostatic problems (4.8), (4.10), (4.12) and (4.22) can be combined to the following equation

$$\nabla \times \left(\frac{1}{\mu}\nabla \times \boldsymbol{A}\right) = \boldsymbol{J}_{\mathrm{s}}, \tag{4.24}$$

where $\boldsymbol{J}_{\mathrm{s}}$ is the source current term, which means that the current density is a known variable. Eddy currents can be calculated with the same equation but now the current density is unknown. Using the electric scalar potential and Faradays law the electric field strength is as follows

$$\nabla \times \boldsymbol{E} = -\frac{\partial \boldsymbol{B}}{\partial t} = -\nabla \times \frac{\partial \boldsymbol{A}}{\partial t} \tag{4.25}$$

$$\boldsymbol{E} = -\frac{\partial \boldsymbol{A}}{\partial t} - \nabla\varphi, \tag{4.26}$$

where φ is the reduced scalar potential. The electric field now has two parts consisting of a rotational part induced by time-variating magnetic field and irrotational part because of polarization and electric charges. Using (4.10), (4.13) and (4.26) the following partial differential equation can be derived to calculate eddy current densities

$$\nabla \times \left(\frac{1}{\mu}\nabla \times \boldsymbol{A}\right) = -\sigma\frac{\partial \boldsymbol{A}}{\partial t} - \sigma\nabla\varphi, \tag{4.27}$$

where σ is the electric conductivity. To summarize, (4.24) can be used to calculate sub-regions where there are source currents and (4.27) is used in eddy current subregions. Furthermore, in two-dimensional problems, the solution becomes simpler because the problem is reduced to *x–y* plane. In 2D case, the magnetic field vectors $\boldsymbol{B}$ and $\boldsymbol{H}$ lie in the *x–y* plane and $\nabla\varphi$ is a linear function of z-component because $\boldsymbol{J}$ and $\boldsymbol{A}$ are parallel to the z-axis direction. Equations (4.24) and (4.27) can now be combined as shown below

$$-\nabla \cdot \left(\frac{1}{\mu}\nabla A_{\mathrm{z}}\right) + \sigma\frac{\partial A_{\mathrm{z}}}{\partial t} + \sigma\nabla\varphi = J_{\mathrm{s,z}}, \tag{4.28}$$

where A_{z} and $J_{\mathrm{s,z}}$ are the z-components of the magnetic vector potential and the source current density respectively. In (4.28), it is assumed that in source current subregions, the electric conductivity term is zero and in eddy current subregions there are no source

currents. This partial differential equation is required for solving the magnetic vector potential in two-dimensional time-dependent problems. Equation (4.28) is too complex to solve analytically so a numerical method is applied to approximate the solution. Next section introduces the basic principles of the finite element method that is commonly used to solve partial differential equations. [2, p. 7:12-7:13, 7:15-7:16]

4.4 Finite element method

Finite element method is a numerical method, which is based on a discretization of a continuous problem to a computer that solves the created discrete system of equations. There are also some other numerical methods to solve the partial differential equations including the finite difference method and boundary element method. However, the finite element method has become the most popular method since it can be used to solve complex geometries and nonlinear problems. Finite element method was first introduced in the 1950s because of the problems in structural mechanics. [2, p. 1:2-1:3]

Especially in the electric machine design, the finite element method is necessary since the machines usually have complex geometries and nonlinear materials. Finite element method can also estimate the distribution of the electric and magnetic field at every point in the problem region. The advantage is that it allows the local analysis of the whole simulation region. The analysis can then point out the most critical points in the geometry in relation to a calculated variable (for example magnetic flux density). FEM gives a good estimation of machine performance. [30, p. 25-26]

The finite element method has some drawbacks though. The solution is always approximate so the method needs to be correctly applied for a given application to achieve reliable solutions. This cannot be done without the required knowledge of the method. Additionally, because the field variables are solved at every point of the geometry the computed time can be long especially in three-dimensional problems. The time can be reduced by optimizing the finite element dimensions and using special periodic and symmetric boundary conditions. [30, p. 25-26]

4.4.1 Triangular elements, shape functions and isoparametric mapping

This section describes the simplest 2D element that is used to solve electromagnetic problems. The element type is first order linear triangular element, which has three nodal points at its vertices. The individual elements within the computation region are first defined in local coordinates and then mapped to the global coordinate system (real elements). Figure 17 shows the local and global coordinate transformation.

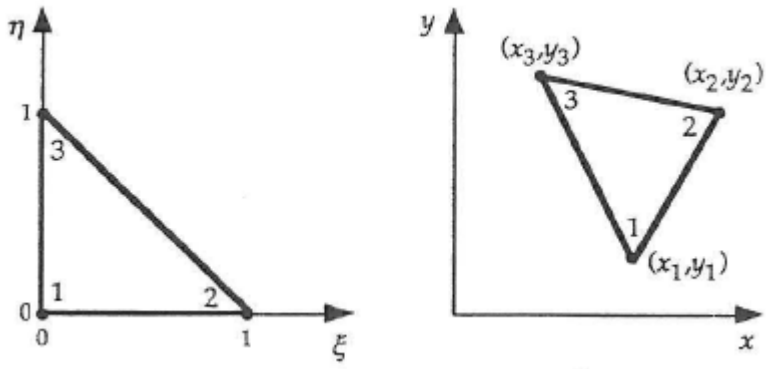

Figure 17. *A generic triangular element in local and global coordinates [2, p. 3:5].*

The left element in Figure 17 demonstrates the reference element in the ξ- η plane and the right element is the actual element in the global *x*-*y* plane. By linear coordinate transformation, it is possible to map any reference element into any triangle in the global *x*-*y* plane as shown below in two different equation sets

$$x = x_1 + (x_2 - x_1)\xi + (x_3 - x_1)\eta \tag{4.29}$$

$$y = y_1 + (y_2 - y_1)\xi + (y_3 - y_1)\eta \text{ or} \tag{4.30}$$

$$x = (1 - \xi - \eta)x_1 + \xi x_2 + \eta x_3 \tag{4.31}$$

$$y = (1 - \xi - \eta)y_1 + \xi y_2 + \eta y_3, \tag{4.32}$$

where x_i and y_i are the triangles vertex coordinates. Using the coordinate transformation every point in the reference element can be mapped uniquely into a point in the real triangle. [2, p. 3:5-3:6]

Another way to define the coordinate mapping of the triangle is to use the area of the triangle. For this, we create a set of coordinates defined as Λ_1, Λ_2, and Λ_3. The following linear relation between these and the *x*-*y* coordinates is defined below:

$$x = x_1\Lambda_1 + x_2\Lambda_2 + x_3\Lambda_3 \tag{4.33}$$

$$y = y_1\Lambda_1 + y_2\Lambda_2 + y_3\Lambda_3 \tag{4.34}$$

$$\Lambda_1 + \Lambda_2 + \Lambda_3 = 1. \tag{4.35}$$

These coordinates are called as barycentric coordinates and are usually called as area coordinates. Figure 18 demonstrates the area coordinates.

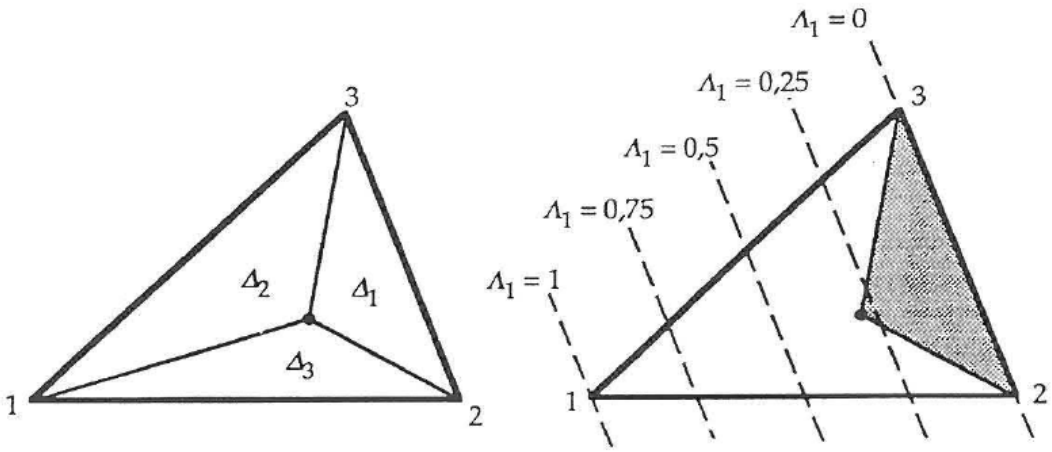

Figure 18. *Demonstration of area coordinates [2, p. 3:7].*

A point in Figure 18 demonstrates the subdivision of the whole area to three equal sized areas Δ_1, Δ_2 and Δ_3. Now the area coordinates are defined as

$$\Lambda_1 = \frac{\Delta_1}{\Delta} \tag{4.36}$$

$$\Lambda_2 = \frac{\Delta_2}{\Delta} \tag{4.37}$$

$$\Lambda_3 = \frac{\Delta_3}{\Delta}, \tag{4.38}$$

where Δ is the whole area of the triangle and subscript refers to the vertex opposite to the subarea in question. The total area is the sum of the subareas so (4.35) is valid. Area coordinates have the quality property that makes them constant along a line that is parallel to the side of the triangle in which the coordinate is zero. Geometrically speaking the area coordinates measure the perpendicular distance of the point toward the vertex from the opposite side. [2, p. 3:5-3:6]

Using (4.33) – (4.38) it is possible to define the expressions of the area coordinates. Next equations define the double area of the triangle and the double area of the three subtriangles defined by *x* and *y*:

$$2\Delta = \begin{vmatrix} 1 & x_1 & y_1 \\ 1 & x_2 & y_2 \\ 1 & x_3 & y_3 \end{vmatrix} = (x_2 - x_1)(y_3 - y_1) - (x_3 - x_1)(y_2 - y_1) \tag{4.39}$$

$$2\Delta_1 = \begin{vmatrix} 1 & x & y \\ 1 & x_2 & y_2 \\ 1 & x_3 & y_3 \end{vmatrix}, 2\Delta_2 = \begin{vmatrix} 1 & x & y \\ 1 & x_3 & y_3 \\ 1 & x_1 & y_1 \end{vmatrix}, 2\Delta_3 = \begin{vmatrix} 1 & x & y \\ 1 & x_1 & y_1 \\ 1 & x_2 & y_2 \end{vmatrix}. \tag{4.40}$$

These two equations can then be combined with (4.36) – (4.38). From this, the following solution is derived:

$$\Lambda_1 = \frac{1}{2\Delta}[(x_2y_3 - x_3y_2) + (y_2 - y_3)x + (x_3 - x_2)y] \quad (4.41)$$

$$\Lambda_2 = \frac{1}{2\Delta}[(x_3y_1 - x_1y_3) + (y_3 - y_1)x + (x_1 - x_3)y] \quad (4.42)$$

$$\Lambda_3 = \frac{1}{2\Delta}[(x_1y_2 - x_2y_1) + (y_1 - y_2)x + (x_2 - x_1)y]. \quad (4.43)$$

Now the area coordinate and the local coordinate system correspondence can be found. The relation between the two coordinate systems is shown below:

$$\Lambda_1 = 1 - \xi - \eta \quad (4.44)$$

$$\Lambda_2 = \xi \quad (4.45)$$

$$\Lambda_3 = \eta. \quad (4.46)$$

The linear triangular element has three nodal points at its vertices. The area coordinate Λ_i is unity at the nodal point i and towards the opposite side of the triangle, the value decreases linearly. This definition maps the area coordinate values and the linear shape function values to equal

$$N_1 = \Lambda_1 = 1 - \xi - \eta \quad (4.47)$$

$$N_2 = \Lambda_2 = \xi \quad (4.48)$$

$$N_3 = \Lambda_3 = \eta, \quad (4.49)$$

where N_1, N_2 and N_3 are the *shape functions*. Shape functions have non-zero values only at those elements that are connected to the same nodal point as the shape function. For every other element, the shape function value is zero. Figure 19 demonstrates the shape function at the nodal point N_i for the element k (left). [2, p. 3:7-3:8]

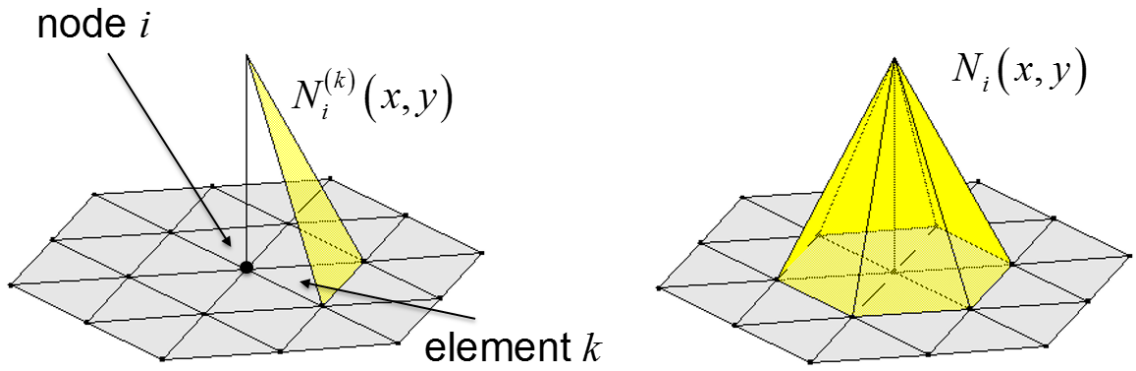

Figure 19. *Shape function at node i and the global shape function. Adapted from [31].*

From Figure 19, it can be seen that the value of shape function N_i at the node i is unity and at every other nodal point the shape function N_i is zero. The other shape functions at

the remaining node points are defined similarly. According to Figure 19 (right), the global shape functions can be obtained by combining the shape functions of the adjacent elements. Therefore, each shape function corresponds to just one nodal point, which is its own. In addition, the shape functions are linearly independent so that the shape function at the nodal point *i* cannot be the combination of the other shape functions. [2, p. 3:2-3:3]

The commonly used method for coordinate transformation (there are other ways) from local to global is to use the shape functions we have already derived to represent the variation of the unknown function. The same shape functions are used for describing the geometry and approximating the unknown function. This is called *isoparametric mapping* and the elements are known as isoparametric elements. The coordinate transformation for a single element is shown below

$$x = \sum_{j=1}^{n} N_j(\xi,\eta)x_j \tag{4.50}$$

$$y = \sum_{j=1}^{n} N_j(\xi,\eta)y_j, \tag{4.51}$$

where n is the number of element nodal points and x_j and y_j are the coordinates of the nodal point j. The continuity of the shape functions guarantees that there are no overlapping elements or holes in the mesh. For the evaluation of finite element matrices, there are two elementary transformations: The global partial derivatives and the surface integration have to be expressed with local coordinates. The linear coordinate transformation is given by (4.29) – (4.30) and the Jacobian matrix in the isoparametric elements is given by

$$\begin{bmatrix} \frac{\partial N_i}{\partial \xi} \\ \frac{\partial N_i}{\partial \eta} \end{bmatrix} = \begin{bmatrix} \frac{\partial x}{\partial \xi} & \frac{\partial y}{\partial \xi} \\ \frac{\partial x}{\partial \eta} & \frac{\partial y}{\partial \eta} \end{bmatrix} \begin{bmatrix} \frac{\partial N_i}{\partial x} \\ \frac{\partial N_i}{\partial y} \end{bmatrix} = \boldsymbol{J} \begin{bmatrix} \frac{\partial N_i}{\partial x} \\ \frac{\partial N_i}{\partial y} \end{bmatrix}, \tag{4.52}$$

where $\boldsymbol{J}$ is the Jacobian matrix. The Jacobian matrix can be obtained with shape functions and nodal coordinates. For solving the global derivatives, the inverse of the Jacobian matrix is required:

$$\begin{bmatrix} \frac{\partial N_i}{\partial x} \\ \frac{\partial N_i}{\partial y} \end{bmatrix} = \begin{bmatrix} \frac{\partial \xi}{\partial x} & \frac{\partial \xi}{\partial y} \\ \frac{\partial \eta}{\partial x} & \frac{\partial \eta}{\partial y} \end{bmatrix} \begin{bmatrix} \frac{\partial N_i}{\partial \xi} \\ \frac{\partial N_i}{\partial \eta} \end{bmatrix} = \boldsymbol{J}^{-1} \begin{bmatrix} \frac{\partial N_i}{\partial \xi} \\ \frac{\partial N_i}{\partial \eta} \end{bmatrix}. \tag{4.53}$$

For integrating the functions in the elements, the determinant of the Jacobian matrix is needed. The transformation of the integration is

$$\int_{\Omega} f(x,y)dxdy = \int_{\Omega_{\mathrm{ref}}} f[x(\xi,\eta), y(\xi,\eta)]\,|\boldsymbol{J}|d\xi d\eta, \tag{4.54}$$

where Ω is the global element domain in the x-y plane and Ω_{ref} is the reference element domain in $\xi - \eta$ plane. Equation (4.54) shows that it is possible to numerically integrate functions in the elements. [2, p. 5:5-5:8]

4.4.2 Discretization with the weighted residual method

The main purpose of numerical methods is to solve a partial differential equation on a discrete set of points in a solution domain. In the finite element method, the discretization is done by dividing the problem area to smaller subdomains in which vertices are defined as discretization points. The mesh size is defined as a distance between two adjacent vertices in the mesh size. Using the discretization to a PDE, the system of equations, where the unknowns are the values at the discretization points (element nodes), can be created. These equations are then solved using direct or iterative methods. [32, p. 95]

The discretizing is started by using the function (4.28) in a static field problem. In static field problems, the time derivative is zero. The weighted residual method is then applied to the equation. The purpose of this method is to find an approximate solution to the chosen functions of the position. The approximate solution can be derived by multiplying the equations with some weight function and integrating over the problem region. A weighted residual method in general form is shown below

$$r = \int_\Omega w[-\nabla \cdot (k\nabla u) - g]d\Omega = 0, \tag{4.55}$$

where u is the scalar potential function describing the field in region Ω and k and g are functions of the position. Applying this method to (4.28) in the source current subregion, the equation is the following

$$r = \int_\Omega w\left[-\nabla \cdot \left(\frac{1}{\mu}\nabla A_z\right) - J_{s,z}\right] d\Omega = 0, \tag{4.56}$$

where A_z describes the field and μ and $J_{s,z}$ are the functions of the position. As can be seen, the equation is exactly in the same form as the general expression of the weighted residual method. This equation contains a second order differential operator, which means that the function A_z has to be continuous and have continuous first derivatives. Thus, region Ω boundary consists of two parts. Using Green's theorem, the highest order of derivative can be reduced by one as shown below:

$$-\int_\Omega w\nabla \cdot \left(\frac{1}{\mu}\nabla A_z\right) d\Omega = \int_\Omega (\nabla w) \cdot \left(\frac{1}{\mu}\nabla A_z\right) d\Omega - \int_\Omega \nabla \cdot \left(w\frac{1}{\mu}\nabla A_z\right) d\Omega \tag{4.57}$$

$$-\int_\Omega w\nabla \cdot \left(\frac{1}{\mu}\nabla A_z\right) d\Omega = \int_\Omega \frac{1}{\mu}(\nabla w) \cdot \left(\frac{1}{\mu}\nabla A_z\right) d\Omega - \oint_\Gamma w\left(\frac{1}{\mu}\nabla A_z\right) \cdot \boldsymbol{n} d\Gamma \tag{4.58}$$

$$r = \int_\Omega \left[\frac{1}{\mu}(\nabla w) \cdot (\nabla A_z) - wJ_{s,z}\right] d\Omega - \oint_\Gamma w\left(\frac{1}{\mu}\nabla A_z\right) \cdot \boldsymbol{n} d\Gamma = 0. \tag{4.59}$$

Now the second order derivative is reduced to one, which means that function A_z still needs to be continuous but the first derivatives can be piecewise continuous over the region Ω. According to aforementioned condition, the second term in (4.59) can be neglected and now the residual is reduced to:

$$r = \int_\Omega \left[\frac{1}{\mu}(\nabla w)\cdot(\nabla A_z) - wJ_{s,z}\right] d\Omega = 0. \tag{4.60}$$

After this, the finite element approximation is used. Now the magnetic scalar potential is expressed as $A_z = \boldsymbol{Na}$. The modified equation is shown below:

$$r = \int_\Omega \left[\frac{1}{\mu}(\nabla w)\cdot(\boldsymbol{Da}) - wJ_{s,z}\right] d\Omega = 0, \text{ where} \tag{4.61}$$

$$\boldsymbol{a} = \begin{bmatrix} a_1 \\ a_2 \\ \dots \\ a_n \end{bmatrix}, \boldsymbol{N} = [N_1 \quad N_2 \quad \dots \quad N_n] \text{ and } \boldsymbol{D} = \begin{bmatrix} \frac{\partial N_1}{\partial x} & \frac{\partial N_2}{\partial x} & \dots & \frac{\partial N_n}{\partial x} \\ \frac{\partial N_1}{\partial y} & \frac{\partial N_2}{\partial y} & \dots & \frac{\partial N_n}{\partial y} \end{bmatrix}. \tag{4.62}$$

The weak formulation of the equation can be derived by setting weight functions to equal shape functions ($w = N_i$). This is known as *Galerkin's method*, which is commonly used in finite element method formulations. Using this method (4.61) can be further reduced to

$$r_i = \left(\int_\Omega \frac{1}{\mu}(\nabla N_i)\cdot(\boldsymbol{Da})d\Omega\right) - \int_\Omega N_i J_{s,z} d\Omega = 0 \tag{4.63}$$

$$\boldsymbol{r} = \boldsymbol{Sa} - \boldsymbol{f} = 0, \tag{4.64}$$

where $\boldsymbol{S}$ is called the stiffness matrix, $\boldsymbol{f}$ is the source vector and $\boldsymbol{a}$ is the nodal value vector. In linear problems, the solution of $\boldsymbol{a}$ is derived by multiplying source vector with the inverse of the stiffness matrix.

The former equation is derived from (4.28) in static case but in dynamic case, also the time derivative needs to be considered. This is solved similarly to the previous case but with the additional term. The following system of equations is derived

$$r_i = \left(\int_\Omega \frac{1}{\mu}(\nabla N_i)\cdot(\boldsymbol{Da})d\Omega\right) + \left(\int_\Omega \sigma \boldsymbol{Na}' d\Omega\right) - \int_\Omega N_i J_{s,z} d\Omega = 0 \tag{4.65}$$

$$\boldsymbol{r} = \boldsymbol{Sa} + \boldsymbol{Ta}' - \boldsymbol{f} = 0, \tag{4.66}$$

where $\boldsymbol{S}$ and $\boldsymbol{f}$ are identical to the static case and $\boldsymbol{a}'$ is the time derivative component of the nodal value vector. The form is now an ordinary system of differential equations and the time discretization can be done by various methods like the Crank-Nicolson method or Backward Difference Formulae. [2, p. 4:1-4:2, 7:15-7:17], [23]

4.4.3 Boundary conditions

For a unique solution, the differential equations must implement boundary conditions at the boundaries of the problem region. For example, if the derivative in the equation is of degree $2k$ then in every boundary in the region must have k boundary conditions. [33, p. 252-253]

In the last chapter when integrating (4.56) in parts, a new term was created at the boundary (second term in (4.59)). These boundary terms that are created by integrating into parts are called natural boundary conditions and they describe only the derivatives of a degree of at least k (parallel to the surface normal). This is due to the nature that they kind of fulfill naturally when formulating the partial differential equations. These boundary conditions can also be called *Neumann boundary conditions*. [33, p. 252-253]

Another common boundary condition is called an essential boundary condition. This boundary condition only includes derivatives that have a lesser order of degree than k. The problem region should always include some essential boundary condition or else it cannot be solved explicitly. These boundary conditions can also be called *Dirichlet boundary conditions*. [33, p. 252-253]

There are several possible ways of setting the essential boundary condition. The easiest way is to set the specific equation, in the system of equations that includes the boundary condition, to equation $T = T_\Gamma$ and solve this using the modified system of equations. Now the coefficient matrix row of this boundary condition is set to zero except for the diagonal element, which is set to unity. Additionally, the source vector value for this row should be set as T_Γ. Another more complex way of setting this boundary condition is to eliminate all the degrees of freedom in the global coefficient matrix at the boundary. This can be done if the values are known in advance. Essential boundary condition is used for example at the outer boundary of the stator in electric machine simulations. In this case, the boundary values are set to zero, which forces the magnetic flux lines parallel to the boundary at the outer stator. [33, p. 252-253]

The Neumann boundary condition can also be applied in *symmetry conditions*. By using homogeneous Neumann's condition, the flux lines can be forced to flow perpendicular to the boundary line (normal vector of the boundary line). According to Neumann's condition, the external material behind the boundary line has infinite magnetic permeability. The Neumann condition can be used to create symmetric conditions. Figure 20 demonstrates the symmetric boundary condition applied to a simple magnetic circuit.

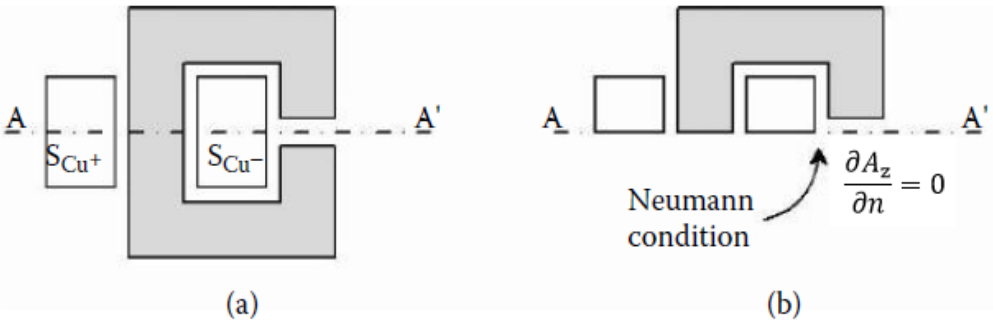

Figure 20. *Simple magnetic circuit describing symmetry conditions. Adapted from [30, p. 64].*

In Figure 20, a symmetry line AA' divides the domain into two mirrored images. Symmetry conditions states that the geometry and the flux distribution will be equal in both domains. When Neumann's condition is applied, the flux lines will be forced perpendicular to the symmetry line since the flux density distribution cannot be discontinuous in this particular case. Thus, the domain can be reduced to half of its size, which in turn reduces the simulation time. [30, p. 64]

Commonly in electrical machines, the *periodic boundary conditions* are used. Periodic boundary conditions are used when there are repetitive sections of electromagnetic devices. Now, in addition to geometrical symmetry, also the field solution is symmetrical. Since electric machines are cylindrical rotating devices with multipolar structures the periodic boundary conditions can be used as an advantage. According to periodic boundary conditions, only a portion of the machine region needs to be solved. Figure 21 shows a simple example of even and odd periodicity in an electric machine with multiple poles.

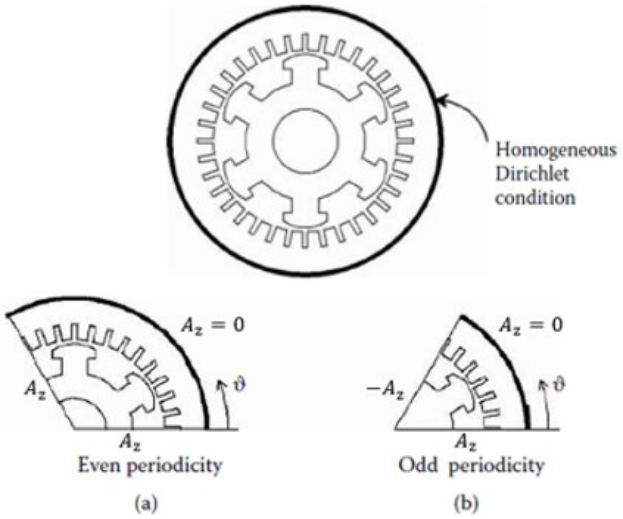

Figure 21. *Periodic boundary conditions in an electric machine. Adapted from [30, p. 63-64].*

As seen from Figure 21, the periodic boundary conditions are very useful in repetitive structures since the model can be reduced for example a third of the original model. Figure

21 also demonstrates that the periodic boundary conditions need to be applied for at least two lines of the boundary. In this case, for the boundary lines representing the right and the left boundaries of the rotor and the stator. In addition, Dirichlet's boundary conditions are used in the outer stator. The remaining parts are mirrored images of the reduced structure. Depending on the domain division, the periodic condition could be either even or odd periodicity. The initial machine has three pole pairs and it is divided into three mirrored parts (a) and into six mirrored parts (b). The A_z value can be now expressed as follows for both cases respectively

$$A_z(r,\vartheta) = +A_z\left(r,\vartheta + (2k)\frac{\pi}{p}\right) \qquad k = 1, 2, 3,\ldots \tag{4.67}$$

$$A_z(r,\vartheta) = -A_z\left(r,\vartheta + (2k-1)\frac{\pi}{p}\right), \qquad k = 1, 2, 3,\ldots \tag{4.68}$$

where the p is the pole pair number, A_z is the z-component of the magnetic vector potential, r is the radius and ϑ is the azimuthal coordinate. The even periodicity is described in (4.67) and the odd periodicity in (4.68). The use of periodicity can be clearly seen from the previous example. In addition, there is another benefit since the geometry is reduced significantly the mesh can be created more accurately to give better results. [27, p. 114], [30, p. 64-65]

4.4.4 Torque formulation

As explained in the introduction, this thesis calculates two different load operations with sinusoidal and PWM supply voltage. The nominal and no-load operation can be found by adjusting the power angle between the rotor and the stator winding magnetic axes. In practice, this is done by adjusting the starting angle of the rotor and iterating the angle so that the obtained torque is at nominal value at nominal load operation and close to zero at no load.

Elmer calculates torque based on the Arkkio's method derived in his dissertation [34]. According to this method, the torque is obtained as an integral over the air gap. The integral area is obtained by setting the inner and outer radius of the air gap. The following equation then calculates the average torque over this defined integration area

$$T_e = \frac{1}{\mu_0(r_s - r_r)} \int_{S_{ag}} r B_r B_\varphi \mathrm{dS}, \tag{4.69}$$

where T_e is the electromagnetic torque, r_s is the outer and r_r is the inner radii of the air gap, S_{ag} is the cross-sectional area of the air gap and B_r and B_φ are the r- and φ-components of the flux density. The air gap inner and outer radii are given in Elmer and the torque is calculated based on this equation. This is a more reliable method compared to the commonly used Maxwell's stress tensor method. [34, p. 55-56]

5. CONSTRUCTING THE SIMULATION MODEL

This chapter demonstrates the construction of the simulation model. First, the stator and the rotor structures are demonstrated. Then the workflow for the simulations is introduced. The main software is the Elmer, which is used as a PDE solver and the other programs are selected by the author. The common workflow for the electromagnetic simulations consists of the geometry, mesh, solver and post-process. The used workflow is based on this. All the most important parts of the simulation model building are documented in this chapter.

The simulated motor is currently located at the Aalto University laboratory and is used as a test motor. The motor was designed by Ingersoll-Rand, which is a co-partner in this thesis. The motor rated parameters are shown in Table 4.

Table 4. *Motor rated parameters.*

Rated parameters	***Value***
Supply voltage	400 V
Rated power	100 kW
Rated current	160 A
Rated speed	34 000 rpm
Rated torque	28.1 Nm
Pole pair number	2
Mechanical angular speed	3560.47 rad/s
Frequency	1133.33 Hz

According to section 3.1, the motor works as a high-speed motor since the rotational speed is over 10 000 rpm and there is no mechanical gearbox attached to the motor. The motor supply voltage is 400 V, which can be obtained in the main electric grid between two phases. Since the pole pair number and the synchronous speed is known, the frequency can be calculated from (2.1).

5.1 Stator design

The stator is constructed by stacking thin steel sheets on top of each other and these sheets are insulated from each other with lamination layers. This reduces the eddy current paths and thus the iron losses in the stator are decreased. The concrete stator structure and the SpaceClaim geometry without the windings is shown in Figure 22.

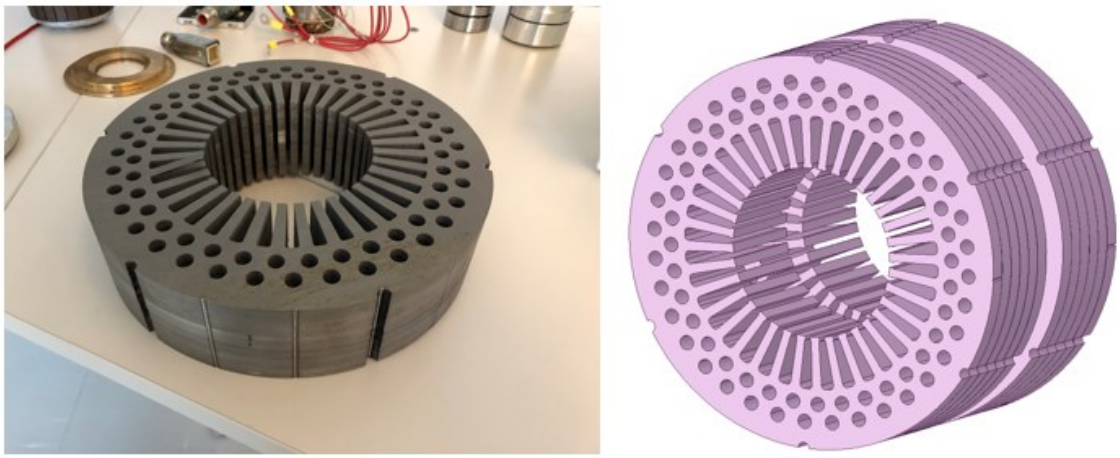

Figure 22. *Stator structure in real life and in 3D geometry software.*

According to Figure 22 (right), the stator is divided into two separate parts, which are 20 mm apart from each other. In addition, there are holes in the stator laminations. These cooling ducts are made to decrease the temperature in the stator and rotor structures because high temperature increases losses and may cause problems in the permanent magnets saturation and demagnetize them. Figure 22 (left) shows an example of how the stator is stacked in practice.

The winding structure is common for the three-phase AC electric machines. Windings are divided into 36 slots in the stator structure and one slot contains two different coils stacked on top of each other, which means that the windings are double-layered. The width and the distance between the two stator teeth are 6.32 mm and 3.8 mm respectively. The mechanical angle between stator teeth is $\frac{360^\circ}{36} = 10^\circ$. The winding diagrams for all phases can be seen from Appendix A. The slot polarities are marked as + or – signs and the connection is divided for both of the stator structures, namely D and N ends. According to Appendix A, the motor is supplied by two separate delta-connected windings each having two parallel branches.

The pole pitch of this stator is 90° mechanical degrees (four poles) according to (2.11) and the fractional-pitch angle is 60° mechanical degrees because the upper layer windings are transferred three slots counter-clockwise. Using (2.12), the coil span is 2/3-pitched. The pitch factor k_p is calculated according to (2.16) and its value is 0.866 for the fundamental voltage. For calculating the distribution factor, we need to define the number of slots per pole and phase. According to (2.17) and (2.18), the number of slots per pole and phase is q = 3 and the distribution factor is 0.9899. The winding factor is now $k_\mathrm{w} = k_\mathrm{d}k_\mathrm{p} = 0.8573$ according to (2.19).

5.2 Rotor design

This section introduces the rotor structure of the simulated motor. Figure 23 shows the rotor structure in practice and in exploded view.

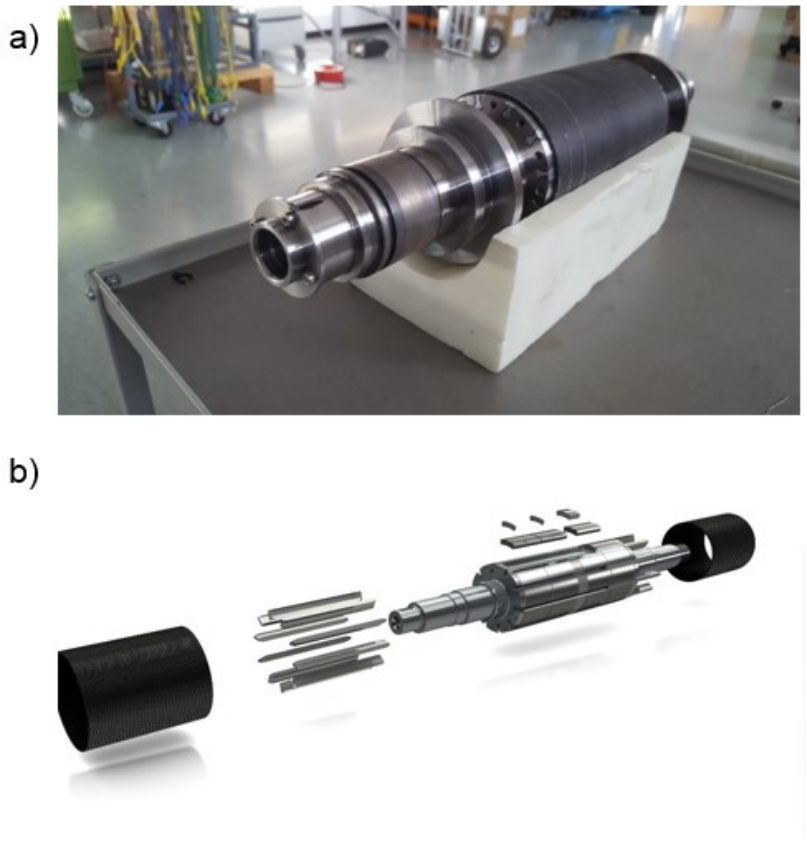

Figure 23. *Rotor design in practice (a) and in exploded view (b).*

In Figure 23 b, the exploding view gives a better look under the carbon fiber sleeve. The main reason for using the carbon fiber sleeve is to ensure that the permanent magnets stick to the rotor. In the left of Figure 23 b, after the sleeve, the aluminum bars are shown. The aluminum bars are short-circuited with both ends using short-circuit rings. This structure is similar to the squirrel cage structure, which is used in induction machines. This can be used as an advantage when starting the motor because the structure adds a starting torque. The center of the rotor is made of solid iron since it is more robust compared to the laminated structure. The permanent magnets are placed at the rotor surface so the structure is similar to the separately magnetized synchronous machine with a non-salient pole structure. The d- and q-axis inductance values are considered equal in simulations.

The rotor has four poles and each pole is divided into eight smaller magnets. The magnets are separated from each other by aluminum parts. The reason for this is to reduce the surface area and volume of the permanent magnets and hence reduce the induced eddy currents in the permanent magnets. This also reduces the heat from the permanent magnets, which is important since the NdFeB magnets are sensitive to heat. Between the

poles, there are non-magnetic materials shaped similarly as the PMs to create symmetric rotor structure, which reduces mechanical vibrations. More about the mechanical design of the rotor can be found in [35].

5.3 Material parameters

The correct material parameters are extremely important for acquiring reliable simulation results. The eddy current losses in the rotor materials are studied, so the material properties for the rotor must be valid. Table 5 shows the material parameters for the simulations.

Table 5. *Motor material parameters.*

Materials	***Relative permeability*** μ	***Electric conductivity*** σ (S/m)	***Density*** ρ (kg/m^3)	***Magnetic behavior***
Stator iron	Nonlinear BH-curve	0 ($1.61 \cdot 10^6$)	7600	Ferromagnetic
Rotor iron	Nonlinear BH-curve	$10.44 \cdot 10^6$	7900	Ferromagnetic
Copper [36]	1	0 ($58.7 \cdot 10^6$)	8900	Diamagnetic
Aluminum [36]	1	$36.9 \cdot 10^6$	2700	Paramagnetic
Permanent magnets (NdFeB) [37]	1.05	$0.667 \cdot 10^6$	7500	Ferromagnetic
Air	1	0	1.2	Paramagnetic

Electric conductivity value is probably the most important constant since it is used to calculate the eddy current losses in FEM simulations according to (4.28). The stator iron electric conductivity is set to zero because we assume in the simulations that there are no axial currents in the stator iron. The stator iron material is Surahammars Bruks NO27 and the parameters are given by IR. However, the rotor iron electric conductivity is not zero since the rotor is made from solid iron because the laminated structure would not withstand the forces due to the high rotational speed of the rotor. Solid rotor structure makes the rotor rigid enough for the 34 000-rpm synchronous speed. Material parameters for rotor iron is taken from *pure iron* at the Finite Element Method Magnetics software material library. Electric conductivity in the air is also zero since air is an insulator. The stator windings are simulated as stranded conductors so the eddy currents are not calculated in the windings and because of that also the copper electric conductivity is set to zero. The relative permeability determines how well the material strengthens the magnetic fields. For stator lamination and rotor iron, the relative permeability is nonlinear and the

BH-curves are shown in Appendixes B and C. The permanent magnets have very low relative permeability and the rest of the materials are non-magnetic.

In addition, the magnetization of the magnets needs to be defined in the material parameters. This has been calculated using the following equations

$$B = \mu_0(H + M) \text{ and for } B_\mathrm{r},\ H = 0 \tag{5.1}$$

$$M = \frac{B_\mathrm{r}}{\mu_0}, \tag{5.2}$$

where M is the magnetization of the permanent magnets. This magnetization describes the permanent magnet field strength when the exterior field strength H is removed. Equation (5.2) can be obtained from (5.1) if the remanence field strength B_r is used since the H is zero at this point in the hysteresis loop. The operating temperature of the rotor magnets is somewhere between $80°\mathrm{C} - 100°\mathrm{C}$ so the obtained B_r value of 1.157 T at $20°\mathrm{C}$ (given by IR) has to be multiplied by the thermal coefficient. According to Table 1, the thermal coefficient α is $-0.12\ \%/°\mathrm{C}$ for the sintered NdFeB magnets. The operating temperature is set to $100°\mathrm{C}$ in these simulations and the new B_r value is 1.061 T accordingly. Using the values defined for the permanent magnets, we get the magnetization value of 844.316 kA/m.

5.4 Workflow

One of the goals of this thesis is to construct a workflow for simulations using Elmer. Elmer is mainly used for solving the PDEs and it requires additional software for pre- and post-processing. Figure 24 demonstrates the workflow and shows the different software used in these simulations.

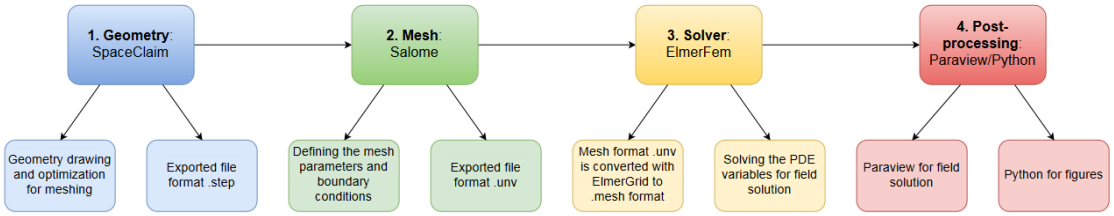

Figure 24. *Block diagram demonstrating the workflow.*

At first, the initial geometry is created or modified so that it can be reasonably meshed. This includes removing small airgaps between different surfaces and removing or reducing the most complex parts of the geometry. The geometry is done with SpaceClaim commercial software and this is the main difference compared to previously studied workflows for Elmer. The finished geometry is then exported as a step format for Salome. Salome is an open-source geometry software, which includes a separate mesh module. In this thesis, the NETGEN plugin for Salome is used to generate the mesh. Before meshing,

the physical groups and boundary conditions are defined in Salome geometry module. The generated mesh is then divided using these same groups. The mesh is exported as universal mesh format (unv). After export, the mesh is converted to Elmer mesh format by using ElmerGrid [38]. The same physical groups and boundary conditions defined in Salome are also transferred to the Elmer mesh. In the solver input file (sif) of Elmer, the solved variables can be defined and ElmerSolver calculates the results from the created mesh and sif file definitions [39]. The solved field and scalar variables are then presented using Paraview and Python respectively.

5.5 Geometry model

The FEM solution starts with a geometry of the calculated model. The initial 3D geometry model of the motor was received from the IR. The 3D-model consisted of stator and rotor models separately and they were already shown in Figure 22 and Figure 23. However, the original models have to be simplified for calculations that are more effective and due to the fact that the motor is simulated in 2D.

The 3D geometry modifications goal is to reduce the 3D-model first for calculations and then the cross-section of this model can be taken for 2D simulations. At first, this is done to the stator and the rotor separately and then combining the geometries into one model. The original and modified stator geometry is shown in Figure 25.

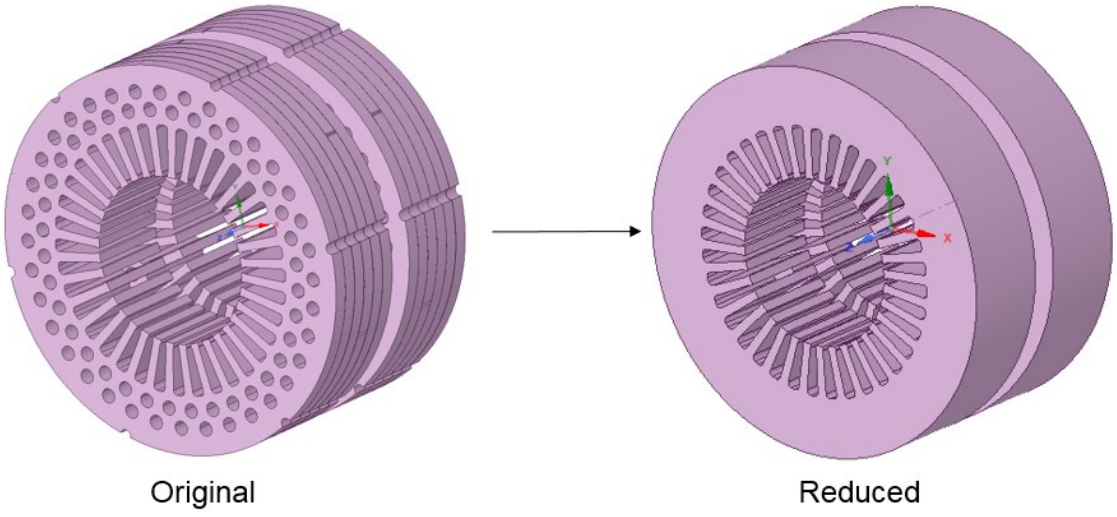

Figure 25. *The original and reduced stator geometry.*

As can be seen from Figure 25, the slots in the outer perimeter of the stator and the thin air gaps between the lamination sheets are filled. This can be done since the outer stator geometry effects in the air gap flux are negligible. The reason for this is to reduce the calculation time of the simulations. In addition, the cooling ducts in the stator structure

can be filled to reduce calculation time and to stay within convergence tolerances. However, the cooling ducts affect the field solution in the stator since the field lines will not go through the holes but the actual effect on the air gap flux is negligible.

The similar procedure needs to be done to the rotor geometry. The original and reduced rotor geometry is shown in Figure 26.

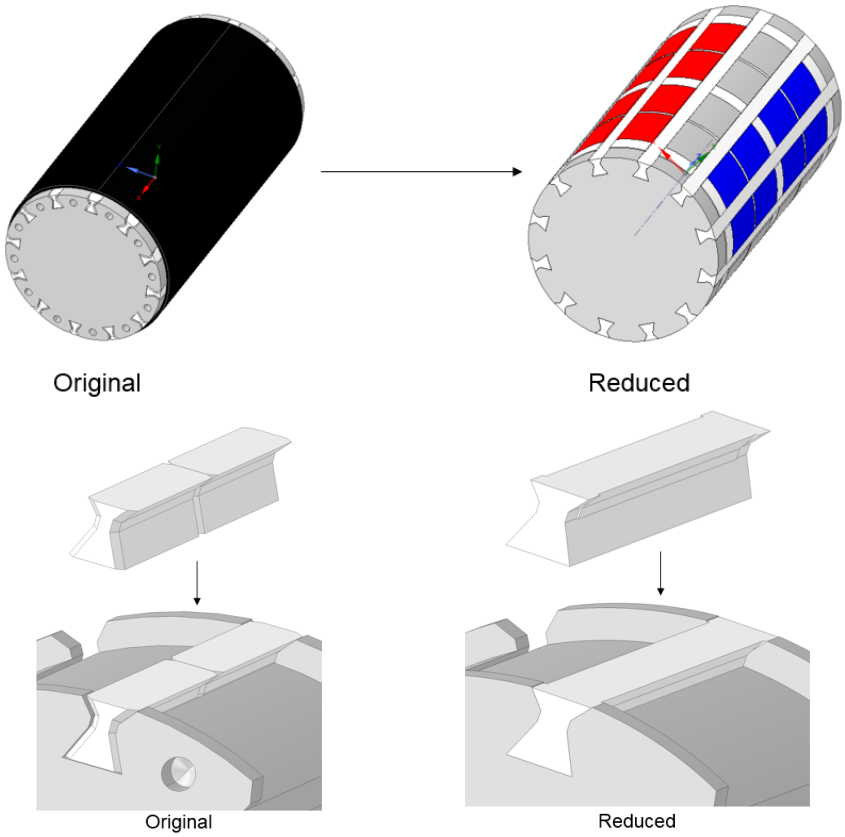

Figure 26. *The original and reduced rotor geometry.*

The reduction of the rotor geometry consists of filling the small airgaps of the rotor structure. According to the Figure 26, this is done by filling the screw holes in the rotor iron, modifying the aluminum bars and aluminum supports so that the small air gaps between the rotor structure and the aluminum parts are eliminated. The magnets are left untouched since they are the most important part of the rotor and modifying them would significantly affect the simulation results.

The whole simulation model consists of both the stator and the rotor so the reduced geometries have to be combined for one simulation model. The reduced 3D-model of the motor is shown in Figure 27.

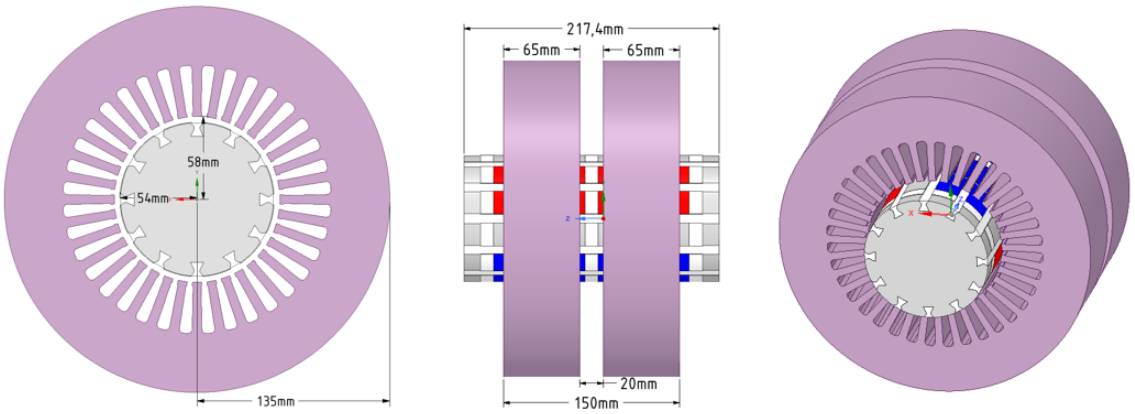

Figure 27.*The reduced 3D-model of the motor.*

The most important dimensions for the motor model are marked in Figure 27. These are the radius from the center of the rotor to the surface of the magnets and stator tooth. These distances are 54 mm and 58 mm respectively, which means that the air gap length is 4 mm. The cooling duct length between the divided stator structures is 20 mm. In addition, the actual stator stack length can be calculated from the dimensions and it is $150\ \text{mm} - 20\ \text{mm} = 130\ \text{mm} = 0.13\ \text{m}$. This is used later in the 2D-model to estimate the length of the simulation model in the z-axis.

The simulations in this thesis are done in 2D-model. The 2D-model can be obtained by taking a cross-section of the 3D-model at the middle of one of the stator structures. The dimensions in xy-axis remain the same and for z-axis, an estimated length is given. The 2D-model of the motor is shown in Figure 28.

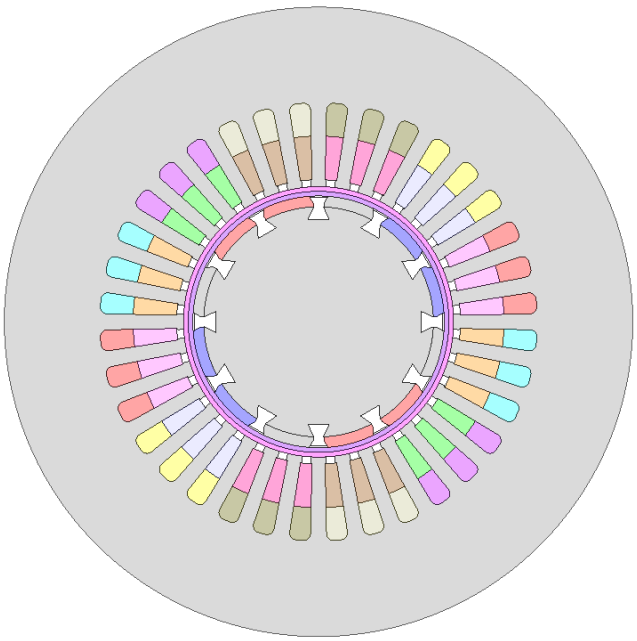

Figure 28. *2D-model of the motor.*

According to Figure 28, some additions are made to the geometry. These additions include windings between the stator teeth, wedges between windings and air gap and the air gap is divided into two parts at the middle. Dividing the air gap into two parts is common in electric machine simulations and is explained later. The geometry format is exported as a step format.

5.6 Mesh

After the geometry is defined for the simulations, the next step is to create a mesh for the model. Mesh is required to discretize the analogic geometry to a finite number of elements, which can be solved with a computer. In these simulations, the first order triangular elements are used. The mesh is done by Salome open-source geometry software, which includes NETGEN plugin for creating meshes. The reduced geometry from SpaceClaim is imported as a step format.

Before meshing, the geometry of the different physical groups and boundary conditions needs to be defined in Salome. Physical groups define the geometry regions. For example, stator windings for different phases and current directions are defined in separate physical groups. Same applies to the boundary conditions, which means that each boundary line needs to be defined separately. The created physical groups and boundary conditions are shown in Figure 29.

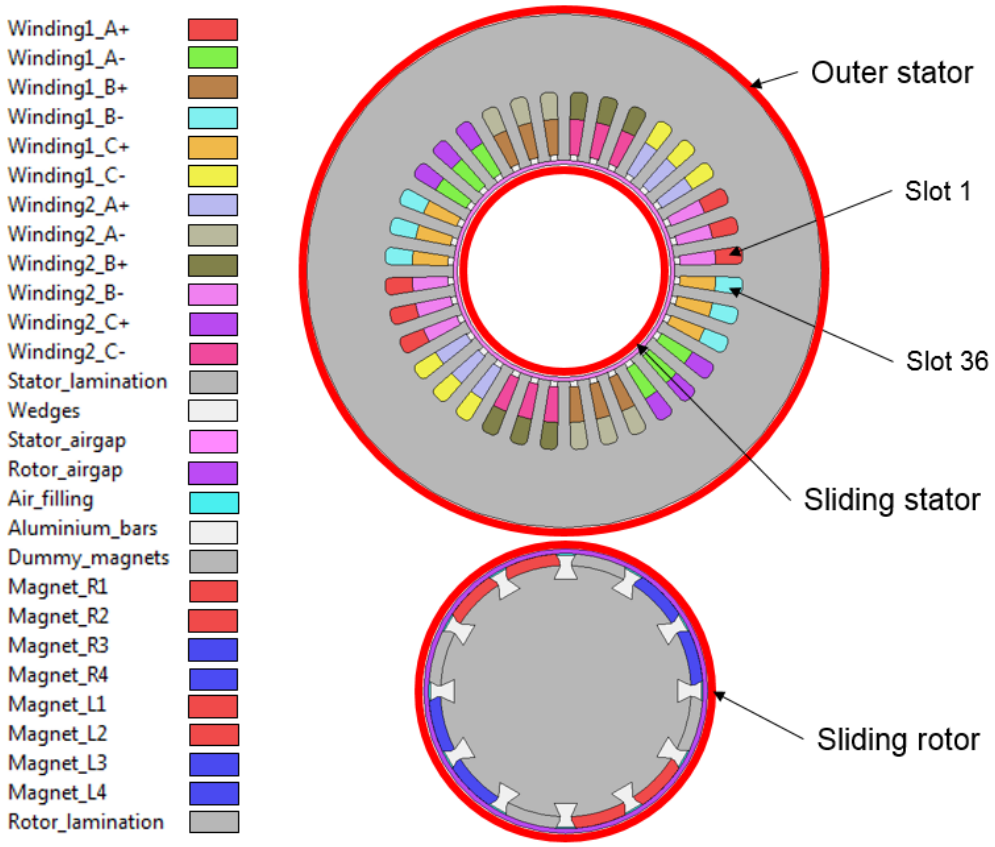

Figure 29. *Physical groups and boundary conditions defined in Salome.*

As seen in Figure 29, the geometry domain is divided into different color-coded regions. These regions represent the different physical groups. The domain consists of 28 physical regions and 3 boundary conditions. The dummy magnets represent the non-magnetic material that is shaped similarly as magnets to stabilize the structure but they are simulated as air. Boundary conditions consist of two different boundary definitions. Outer stator line represents the Dirichlet's boundary condition, which defines the magnetic vector potential as zero. The stator and the rotor sliding boundaries are required separately for transient simulations when the rotor is rotating. This is the reason why the stator parts have some offset compared to the rotor parts. The sliding boundary needs two boundary lines in which the other is the master boundary where definitions are made and the other is the dummy slave boundary, which the master uses as a reference. The mesh adapts for every time step even when the rotor is rotating. The two separate winding circuits are defined according to Appendix A.

After defining physical groups and boundary lines, the geometry is meshed for computer solution. Mesh density can be defined for physical groups separately, which is convenient since the density can be optimized. Usually, the density must be high in the most important parts related to the solution and low where the solution does not affect significantly to the simulations. For example, mesh density in the air gap and on the surface of the rotor parts is set to high since the induced eddy currents are solved in the rotor. In the outer stator structure, the mesh density can be set to low since the eddy currents are calculated only in the rotor.

Salome is an open source geometry software and uses external meshing modules. In this thesis, the NETGEN plugin is used since it does not require a commercial license. The mesh densities at different physical groups and the overall quality of the mesh can be controlled with this plugin. Table 6 shows the mesh parameters used in the simulations.

Table 6. *Mesh parameters.*

General mesh parameters	***Value***
Min. size	$6.66e^{-6}$
Max. size	0.008
Fineness	Fine
Growth rate	0.2
Nb. Segments per edge	2
Nb. Segments per radius	3
Local sizes	***Value***
Rotor iron	0.005
Air gaps	0.0008
Remaining rotor parts	0.0008
Other groups	0.008

In Table 6, the min. and max. sizes define the maximum and minimum linear dimensions for the mesh. Fineness defines the mesh detail from very coarse to very fine. Growth rate sets how much the linear dimensions in adjacent cells can differ (0.2 means 20 %). The number of segments per edge and per radius defines the minimum number of mesh segments in which the edges, curved edges, and surfaces will be split. The local sizes allow the definition of the element sizes on and around the defined physical groups. With these settings, the mesh for the rotor and the stator is shown in Figure 30.

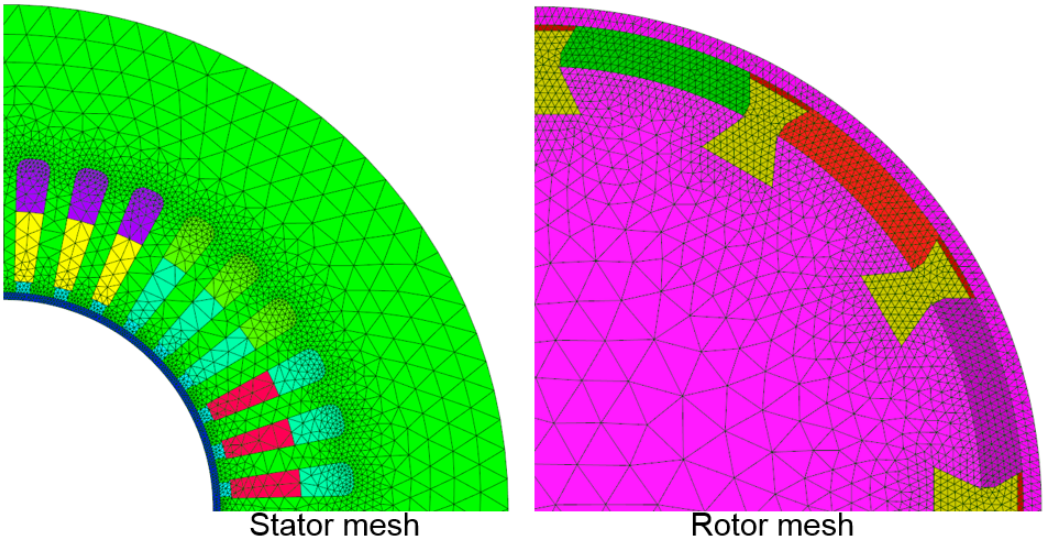

Figure 30. *Stator and rotor meshes.*

In Figure 30, a quarter of the stator and the rotor meshes is shown. The remaining quarters are symmetric, so it is enough to show one-quarter of the created mesh. The mesh is sparser in the stator groups compared to the rotor groups. This way the mesh is optimized for a more effective computer solution since the stator field is not as important as the rotor field. The created mesh is exported as unv format.

5.7 Setting up the solver

This workflow uses Elmer for solving the electromagnetic field. Since Elmer is used as the main tool for this thesis the solving process is studied closer compared to the other programs used in this workflow. The following block diagram in Figure 31 shows the solving process.

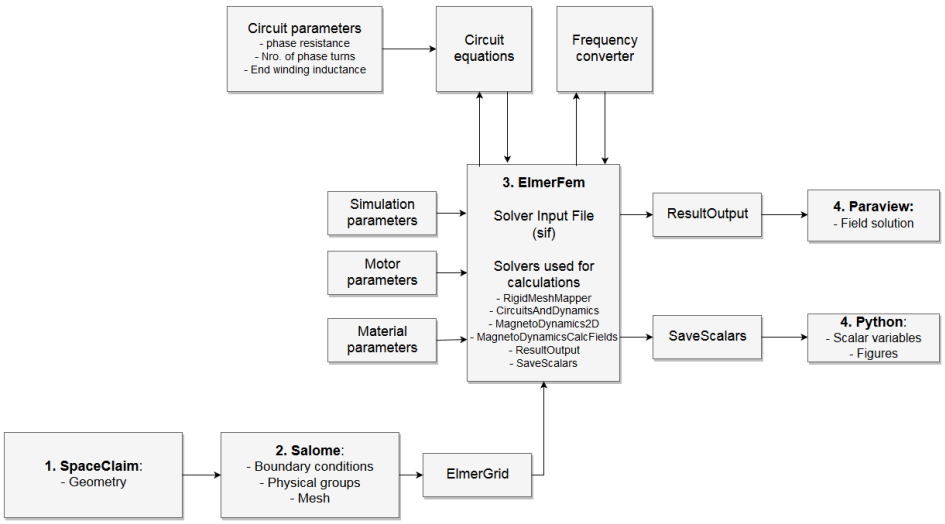

Figure 31. *Block diagram describing the solver process.*

As seen previously the geometry was made using SpaceClaim and the mesh was created using Salome. This mesh is exported as unv format and converted to Elmer mesh format using ElmerGrid, which is included in the installation package. The solution is based on the definitions made in the sif file. The ElmerFem block also shows all the used solver models in the sif. More info about the solver models can be found at [40]. The material and motor parameters are already defined in Table 4 and Table 5. The most important simulation parameters are shown in Table 7.

Table 7. *Simulation parameters.*

Variable	***Value***
Simulation type	Transient
Time stepping method	1st order backward difference formula
Time step size	$1/f_{\mathrm{n}}/450 \approx 1.96\ \mu\mathrm{s}$
Number of time steps	7200
Number of periods per simulation	$7200/450 = 16$
Circuit model depth	0.13 m

The simulations are defined as transient, which means that the simulations are done in relation to time. Another choice would be a steady-state simulation but since the eddy currents are a time-dependent phenomenon, the simulations are done as transient. The time discretization is required for the computer solution. The first order backward difference method is used in the simulations. The time step size defines that one fundamental period is divided into 450 different time steps. A number of time steps define how many

time steps are calculated within one simulation. The total simulation time with these settings is 14.11 ms. Circuit model depth sets the axial length of the motor to the simulation model, which is 0.13 m in this case.

5.7.1 Supply circuit definitions

As shown in the geometry chapter the stator structure is divided into two separate parts leaving a cooling channel of 20 mm in the middle of the rotor. There are two separate winding circuits for both of these stator structures and both of these circuits have two parallel branches. The full connection diagram for the stator circuit can be seen in Appendix A. Figure 32 shows a circuit diagram describing one branch of both of the circuits 1 and 2.

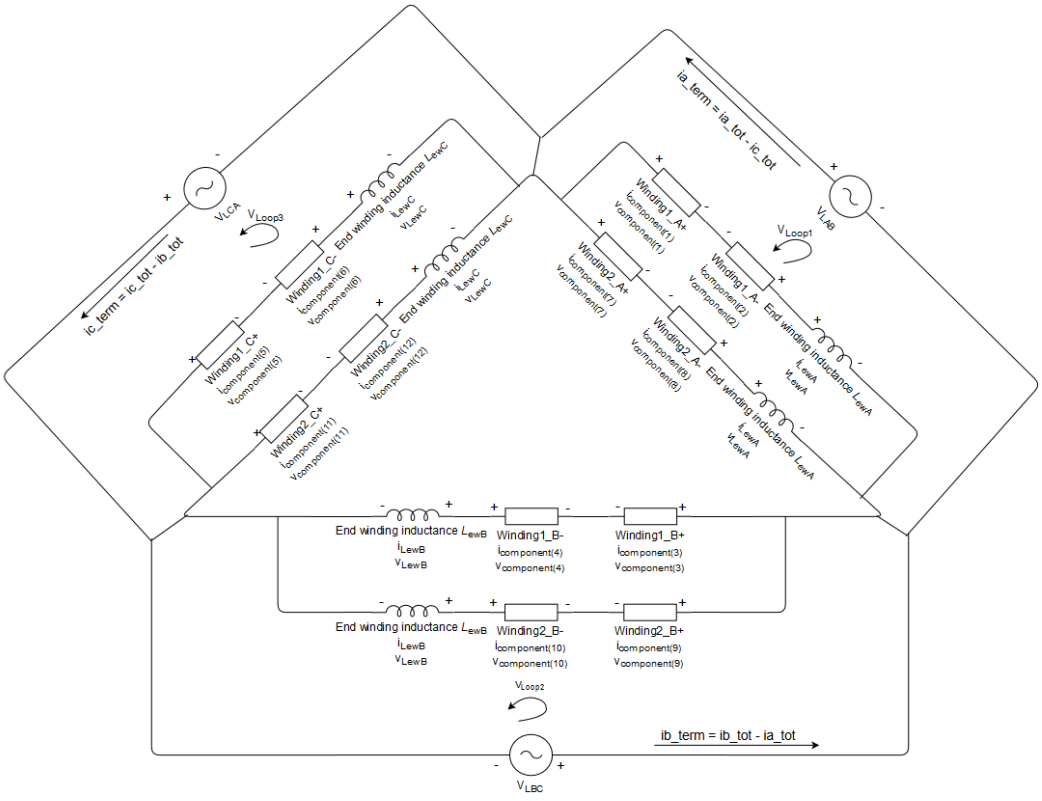

Figure 32. *Circuit diagram of the delta connected supply circuit.*

The winding number 1 describes the first supply circuit and winding number 2 describes the second supply circuit. In addition, the end windings are taken into account by adding an analytically estimated end winding inductance to the circuit. According to the winding diagram in Appendix A, both of the circuits 1 and 2 would have one additional parallel branch (4 branches per phase). However, if assumed that the currents are equal at both branches (symmetry) these additional branches can be taken into account by modifying the phase resistance, the end winding inductance, the number of turns and supply voltage values. The initial values for the phase resistance and end winding inductance are 0.014

Ω and 26 µH. The number of turns if only one winding is used can be calculated with the following equation

$$N = \frac{pqj}{a}, \tag{5.3}$$

where p is the pole pair number, q is the phase belt number, j is the number of turns per slot (16) and a is the number of parallel paths (2). Equation (5.3) defines the number of phase turns, which is 48. However, in this case, the number of turns is divided into two separate windings and the value is divided by two. Accordingly, 24 number of turns per winding is used in the simulations. The two separate circuits and four parallel branches can be taken into account by multiplying the number of phase turns by two, the phase resistance, and end winding inductance by four and the supply voltage by two (two separate circuits). Table 8 shows these modified values.

Table 8. *Modified circuit parameters.*

Variable	***Value***
Number of turns	$2 \cdot 24 = 48$
Phase resistance	$4 \cdot 0.014\ \Omega = 0.056\ \Omega$
End winding inductance	$4 \cdot 26\ \mu\text{H} = 104\ \mu\text{H}$
Supply voltage	$2 \cdot 400\ \text{V} = 800\ \text{V}$

These values are assigned in additional file, described by circuit equations block, which communicates with the sif file. The supply circuit is created according to the circuits and dynamics solver found in the Elmer models manual [40, p. 106-110]. This model solves the following function

$$\boldsymbol{A}\boldsymbol{x}' + \boldsymbol{B}\boldsymbol{x} = \boldsymbol{f}, \tag{5.4}$$

where the $\boldsymbol{A}$ and $\boldsymbol{B}$ are the coefficient matrices, $\boldsymbol{x}$ is the circuit variable vector and $\boldsymbol{f}$ is the force vector. Circuit equations consist of two categories. First, the component equations are used to define the behavior of the component and secondly the circuit network is created in Figure 32. The components are defined in the sif file in the component section. In this case, there are 12 components for 6 windings since the windings are further divided into positive and negative components according to the direction of the z-axis current in the windings. The component section is also divided into ideal electric component equations and the FEM coupled equations. In these simulations, the ideal components consist of the end winding inductances and the FEM components consist of the phase winding equations. Furthermore, in the FEM equations, the current and the voltage of the component need to be solved separately. The currents are solved by using Kirchhoff's first law and the voltages by Kirchhoff's second law. The finite element component equations are

defined automatically in Elmer after the circuit diagram is made and the specific component data is given. The equations for circuit 1 in Figure 32 are shown below

$$\begin{cases} i_{\text{component(2)}} + i_{\text{LewA}} = 0 \\ v_{\text{component(1)}} = \text{Elmer defines automatically} \\ v_{\text{component(1)}} - v_{\text{component(2)}} + v_{\text{LewA}} = V_{\text{LAB}} \\ i_{\text{component(1)}} + i_{\text{component(2)}} = 0 \\ v_{\text{component(2)}} = \text{Elmer defines automatically} \\ L_{\text{ewA}} i'_{\text{LewA}} - v_{\text{LewA}} = 0 \end{cases} \tag{5.5}$$

$$\begin{cases} i_{\text{component(4)}} + i_{\text{LewB}} = 0 \\ v_{\text{component(3)}} = \text{Elmer defines automatically} \\ v_{\text{component(3)}} - v_{\text{component(4)}} + v_{\text{LewB}} = V_{\text{LBC}} \\ i_{\text{component(3)}} + i_{\text{component(4)}} = 0 \\ v_{\text{component(4)}} = \text{Elmer defines automatically} \\ L_{\text{ewB}} i'_{\text{LewB}} - v_{\text{LewB}} = 0 \end{cases} \tag{5.6}$$

$$\begin{cases} i_{\text{component(6)}} + i_{\text{LewC}} = 0 \\ v_{\text{component(5)}} = \text{Elmer defines automatically} \\ v_{\text{component(5)}} - v_{\text{component(6)}} + v_{\text{LewC}} = V_{\text{LCA}} \\ i_{\text{component(5)}} + i_{\text{component(6)}} = 0 \\ v_{\text{component(6)}} = \text{Elmer defines automatically} \\ L_{\text{ewC}} i'_{\text{LewC}} - v_{\text{LewC}} = 0 \end{cases}, \tag{5.7}$$

where component 1 refers to the winding A positive direction current and voltage, component 2 refers to the winding A negative direction current and voltage and so on. The voltages V_{LAB}, V_{LBC} and V_{LCA} represent the supply line-to-line voltages, which are created by the frequency converter block. The voltage equations for the components are automatically defined in Elmer. The circuit 2 equations are identical except for the component indexes, which are between values 7–12. From this, we get six similar equation sets, which are separated from each other.

5.7.2 Frequency converter function

In electric machine simulations, there are two methods to model the supply for the motor: the motor can be supplied by current if the current value is already known or the motor can be supplied by voltage and the current is calculated from the voltage value. The first method does not require any additional circuitry and the current can be supplied directly to the model in the sif file. In this thesis, the motor is supplied by three-phase line-to-line voltages and the terminal and winding currents are calculated using the circuit created in the previous chapter.

The frequency converter creates a voltage based on the pulse width modulation. Figure 33 demonstrates the output of the frequency converter function in one period.

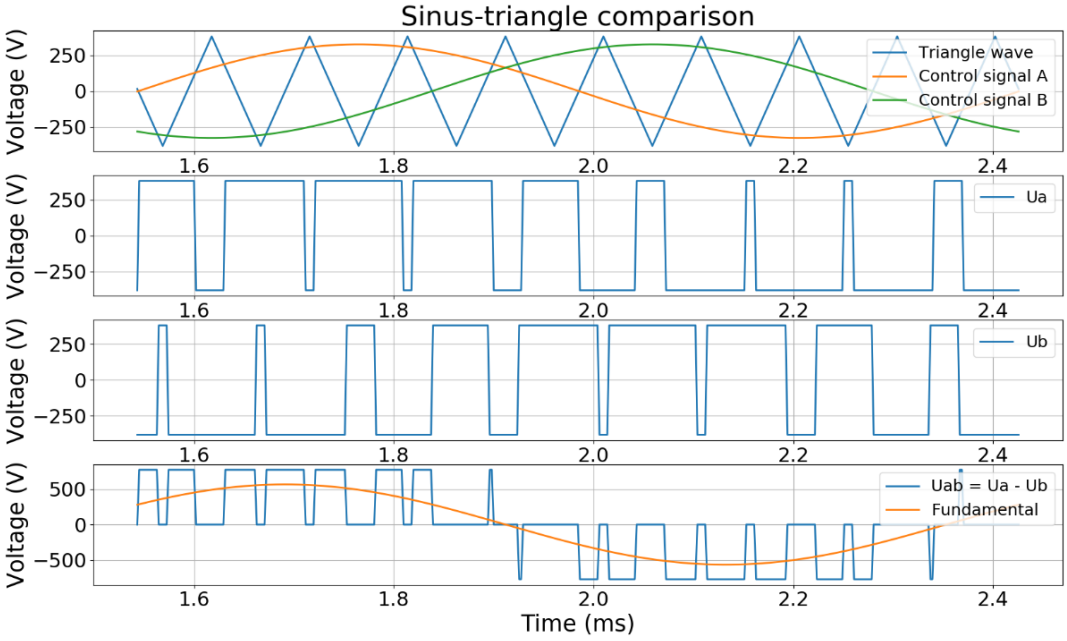

Figure 33. *Working principle of the frequency converter supply.*

Figure 38 demonstrates the working principle of the frequency converter function for the line-to-line voltage V_{ab}. This can be done by comparing two sinusoidal signals, which are phase shifted by 120 degrees to a triangle wave. The phase voltage V_a is $+\frac{1}{2}V_d$ if the control signal is higher than a triangle wave and $-\frac{1}{2}V_d$ if the control signal is lower than a triangle wave. This applied also for the phase voltage V_b. The pulse width modulated line-to-line voltage can be obtained by taking the difference between these phase voltages ($V_{ab} = V_a - V_b$). In the bottom figure, also the fundamental wave of the voltage V_{ab} is shown. The frequency converter parameters are shown in Table 9.

Table 9. *Frequency converter parameters.*

Variable	***Symbol***	***Value***
Triangle wave	$\hat{V}_{tri}$	381.97 V
Control signals	$\hat{V}_{control\ a}, \hat{V}_{control\ b}$	326.59 V
Phase voltages	$\hat{V}_a, \hat{V}_b$	381.97 V
DC voltage	V_d	763.94 V
Fundamental frequency	f_n	1133.33 Hz
Switching frequency	f_s	$9 \cdot f_n = 10.2$ kHz
Amplitude modulation ratio	m_a	0.85503
Frequency modulation ratio	m_f	9
Fundamental voltage	$(\hat{V}_{Ao})_1$	565.67 V

The amplitude modulation ratio and frequency modulation ratio can be calculated by using (2.23) and (2.24). The control signal values can be calculated by using (2.22). The line-to-line fundamental voltage value is the control signal value multiplied by square root of three. The switching frequency is quite high in this case since the motor is operating at a very high speed, which may cause some problems in practice.

6. SIMULATION RESULTS

In this chapter, the previously created model is simulated. Before the simulation results, the methods to reduce transients are introduced. Three different steps have been taken in the simulations to reduce transients significantly. This is done because the start-up transients of the motor are not studied in this thesis. The focus is in the operation of the motor when it reaches steady-state operation. The nominal load and no-load operation points are simulated and the copper and eddy current losses are studied from the simulations. Both of these operation points are supplied by either sinusoidal or PWM voltage supply thus four different simulation cases are presented. The losses behavior is studied at these different cases and compared to each other. Then the field solution for magnetic flux density and the current density is presented for nominal load and no-load operation points with the PWM voltage supply. These field solutions demonstrate the difference between the two operation points. At last, the measured losses are studied.

6.1 Transient analysis

In the first test simulations, the model did not reach steady-state operation and the results showed considerable transient behavior regardless of the simulation time. Because of that, there are three different methods used in the simulations to reduce the transients significantly. The motor is started with a sinusoidal supply voltage using a ramp function ($\text{time} \cdot \frac{1}{f} \cdot V_{\text{supply}}$). The addition of electric conductivity in the simulations caused significant transient behavior and in the field solution, the magnetic flux was only focused on the surface of the rotor. It was found out that the simulation model requires the steady-state solution before the electric conductivity can be added. In these simulations, the steady-state is obtained without the electric conductivity at first. After that, the electric conductivity is added to the simulation model at 3.53 ms. At last, the sinusoidal voltage is changed to PWM voltage during one fundamental period starting at 7.94 ms. The total simulation time is 14.11 ms. With these steps, the motor reaches steady-state with both sinusoidal and PWM voltage supplies during one simulation. However, the PWM voltage supply increases the average values especially for the torque and input power so the PWM voltage simulations need to be adjusted and four simulations are required. These steps were found working rather well and their effect can be clearly seen in the simulation results shown in section 6.2.

6.2 Nominal load simulations

The nominal load simulations are required to check the model. The model operates correctly if the nominal current produces the nominal torque. As shown previously, the

torque of the motor depends on the power angle between the rotor and the stator. In the simulations, this angle can be adjusted by modifying the rotor-starting angle. The rotor-starting angle can be seen from Figure 28 and Figure 29. Additionally, the power balance value should be close to zero or small compared to the input power. The power balance equation is shown below

$$P_{\mathrm{PB}} = P_{\mathrm{in}} - P_{\mathrm{shaft}} - P_{\mathrm{eddy}} - P_{\mathrm{Cu}}, \tag{6.1}$$

where P_{PB} is the power balance, P_{in} is the input power, P_{shaft} is the shaft power ($T_1\omega_1$), P_{eddy} is the eddy current losses and P_{Cu} is the copper losses. The power balance should be zero in the ideal case since the input power should be equal to the sum of shaft power and the calculated losses. In practice, the difference is not zero since the numerical results are always approximations. For example, the time discretization method affects to the power balance results. The nominal load simulations with the sinusoidal and the PWM voltage are shown in the next subchapters.

6.2.1 Sinusoidal supply

The simulations start by checking the operation at nominal load. Previously it was defined that because of the supply circuit connection diagram the motor should be supplied by two times the rated voltage. However, this was just used in the simulations and in the results, the voltages are divided by two. Figure 34 shows the terminal voltages of the motor.

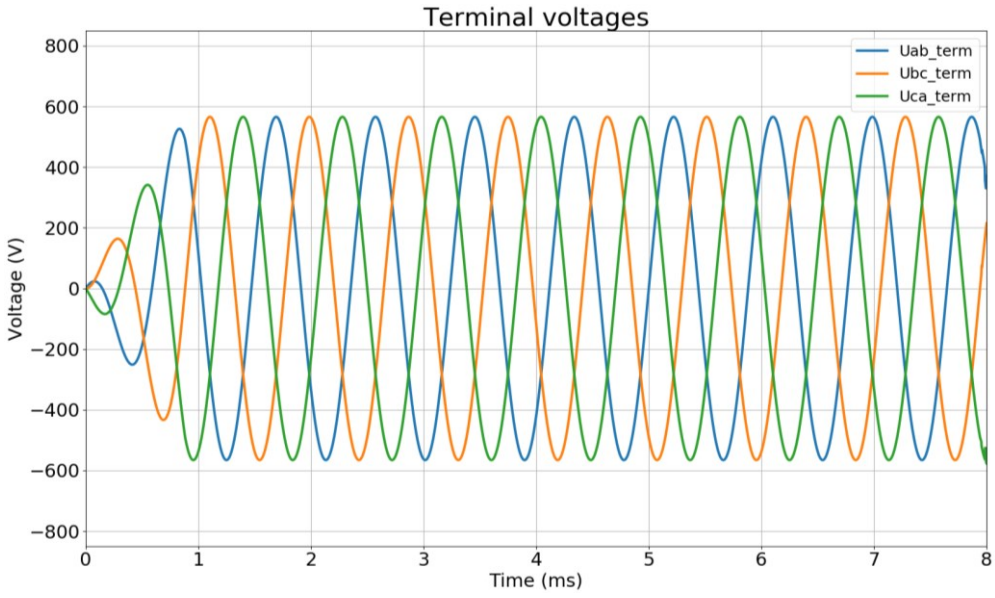

Figure 34. *Terminal voltages.*

The results presentation in the sinusoidal supply is restricted between 0 ms to 8 ms since the supply would change to PWM after 7.94 ms. The root mean square (RMS) values for the line-to-line voltages are close to 400 V, which seems correct since the motor rated

RMS voltage is 400 V as shown in Table 4. In the voltage waveforms, the ramp function for reducing the transients at motor start is clearly seen.

Next, the winding currents and terminal currents are studied. The winding current represents the current that flows in the stator windings and the terminal currents represent the currents flowing in the terminals (Figure 32). Figure 35 shows the winding and terminal currents.

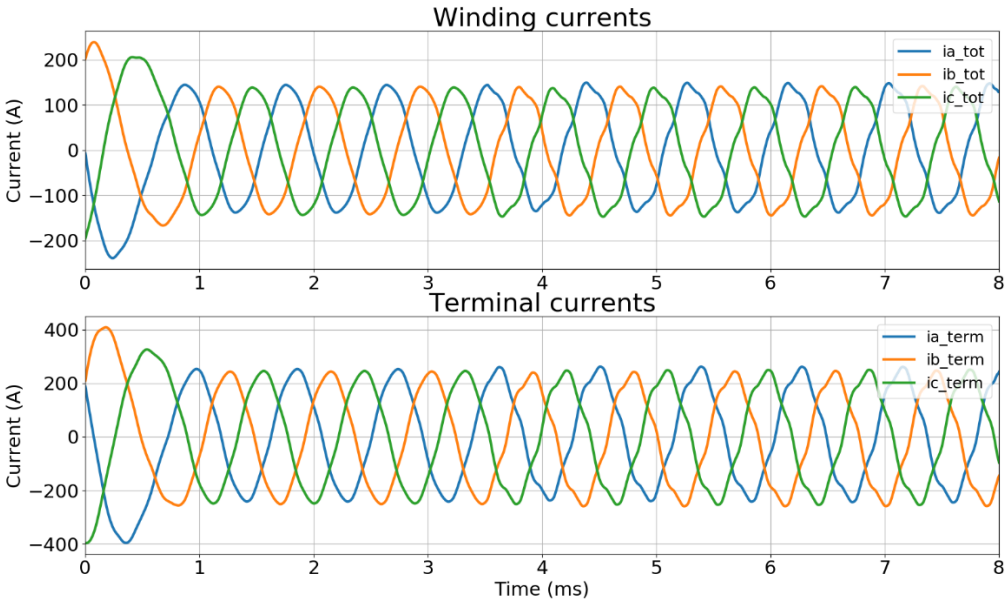

Figure 35. *Winding and terminal currents.*

In Figure 35, the addition of electric conductivity is seen from the current waveforms. After 3.53 ms there is a clear notch in the current waveforms, which is the result of adding the electric conductivity. The RMS values for the winding and terminal currents are around 99.44 A and 172.24 A respectively. According to Table 4, the rated current is 160 A, so the terminal currents are slightly elevated in the simulations.

The torque and input power are studied next since these can be used to check the model. If the rated power is obtained with the rated torque, the model should be working correctly. Figure 36 shows the torque and input power.

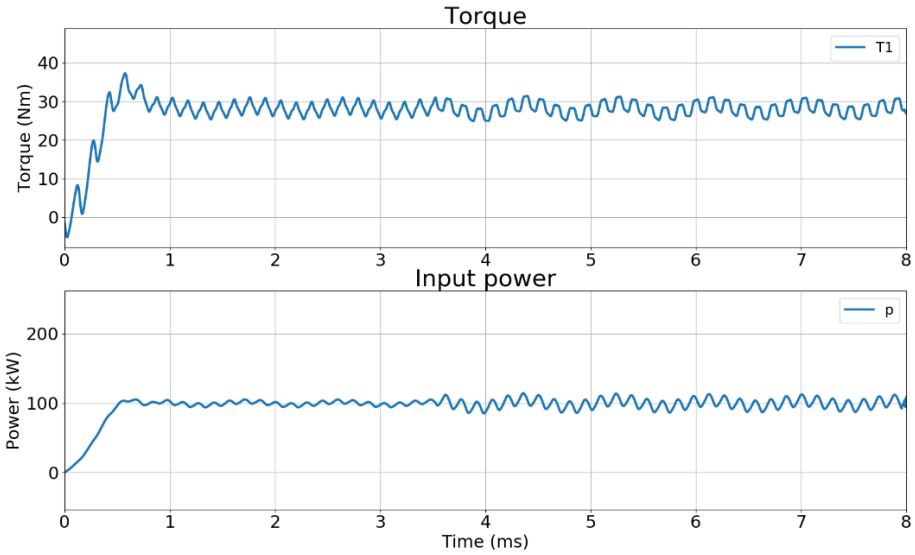

Figure 36. *Torque and input power of the motor.*

According to Table 4, the rated torque is 28.1 Nm and the shaft power is 100 kW. Figure 36 shows that the torque and input power is very close to those values and in principle, the model seems to be working correctly. The increased ripple value of the curves after 3.53 ms is due to the added electric conductivity.

The torque, input power and losses at different parts of the rotor are studied next in one fundamental period. Figure 37 shows these curves and their average values.

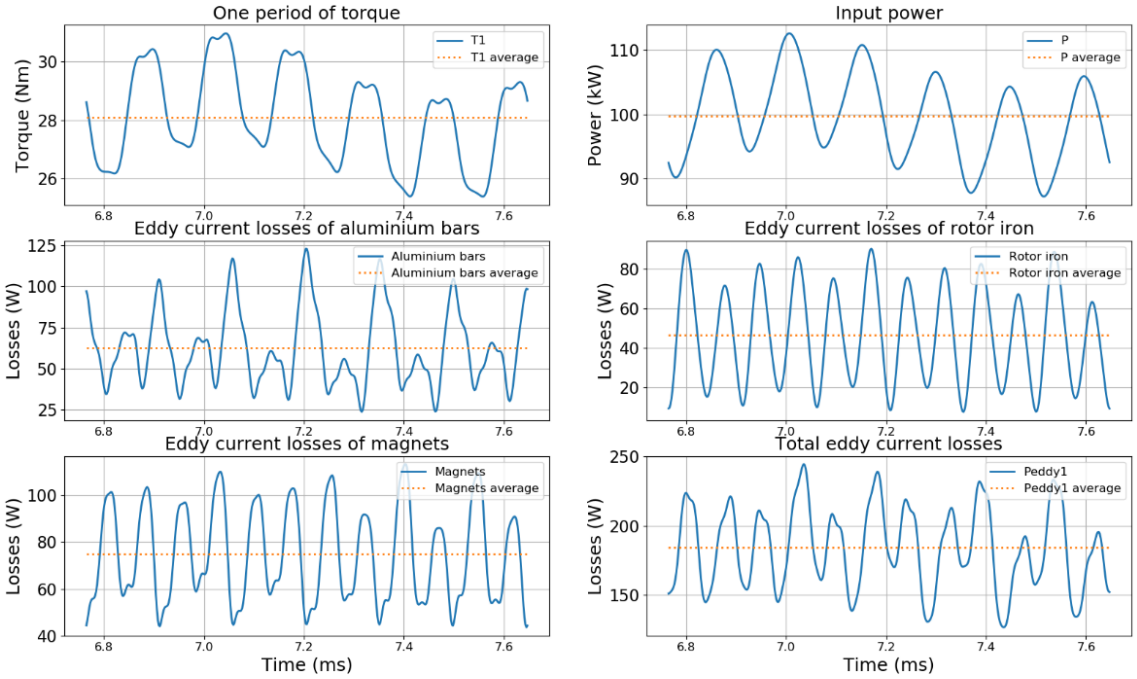

Figure 37. *Torque, input power and losses in one fundamental period.*

The fundamental period in Figure 37 is taken between 6.76 ms – 7.65 ms in the simulations. The average values for the torque and input power are 28.085 Nm and 99.707 kW

respectively. These are very close to the rated values, which shows that the base model is working correctly. In addition, the eddy current losses are calculated from the three different rotor materials. The eddy current losses for the aluminum bars, rotor iron and magnets are 62.75 W, 46.74 W and 74.77 W respectively. The total eddy current losses are then 184.25 W. For total losses the copper losses needs to be added. The copper losses are calculated according to (3.3) and the value is 414.14 W. Now, the total losses are 598.39 W. These total losses can be used in power balance calculations according to (6.1) and the calculated power balance is -886.58 W. As noted before, the power balance is not zero but if the power balance is compared to the input power, the power balance value is 0.889 % of the input power and therefore it can be neglected.

6.2.2 PWM supply

This chapter studies the effect of the PWM voltage supply to the motor. Because of the transient phenomena, the motor cannot be started directly with the PWM voltage even when using a ramp function. Therefore, the sinusoidal voltage supply is changed to PWM voltage supply during one fundamental period starting at 7.94 ms. Figure 38 shows the terminal voltages of the motor with the PWM voltage supply.

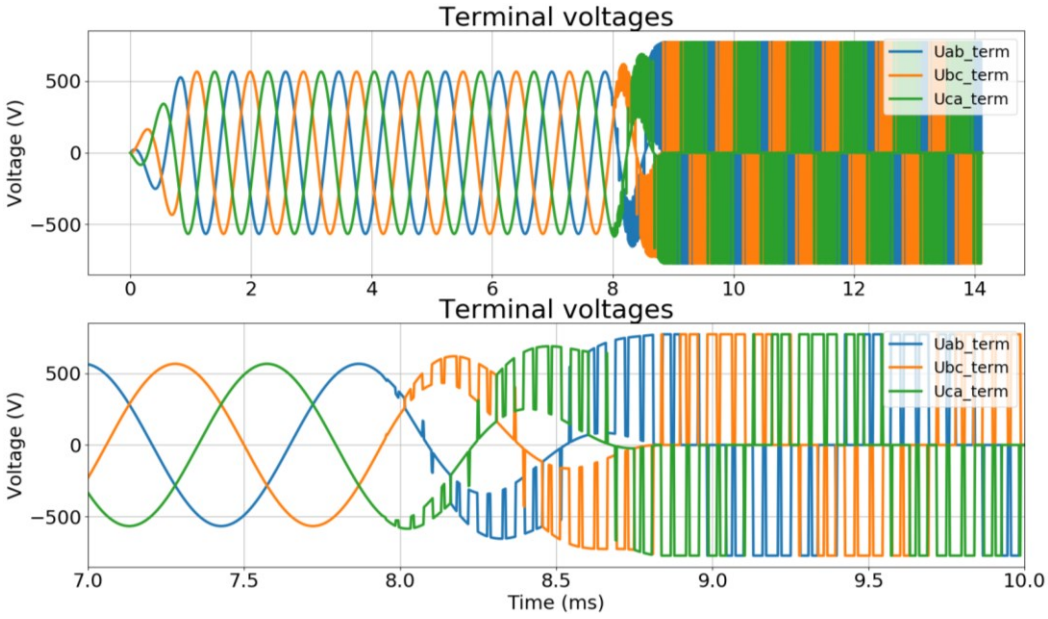

Figure 38. *Terminal voltages.*

The lower plot in Figure 38 shows the transition from sinusoidal to PWM voltage supply more closely. The voltage values are studied between 7.94 ms – 14.11 ms. The PWM voltage peak value is 771.72 V and it has been scaled so that the fundamental signal of the PWM voltage produces the same phase and peak voltage value than the sinusoidal voltage before the transition at 7.94 ms. This method ensures that there will be no extra

transients in the simulations. If the phase and peak values differ, there would be significant transients in the simulations. Therefore, the fundamental values of the PWM voltages should be the same as sinusoidal supply values (400 V RMS).

As can be seen from the voltage supply, the voltage input is far from sinusoidal. This should significantly decrease the quality of the winding and terminal currents. Figure 39 shows the winding and terminal currents.

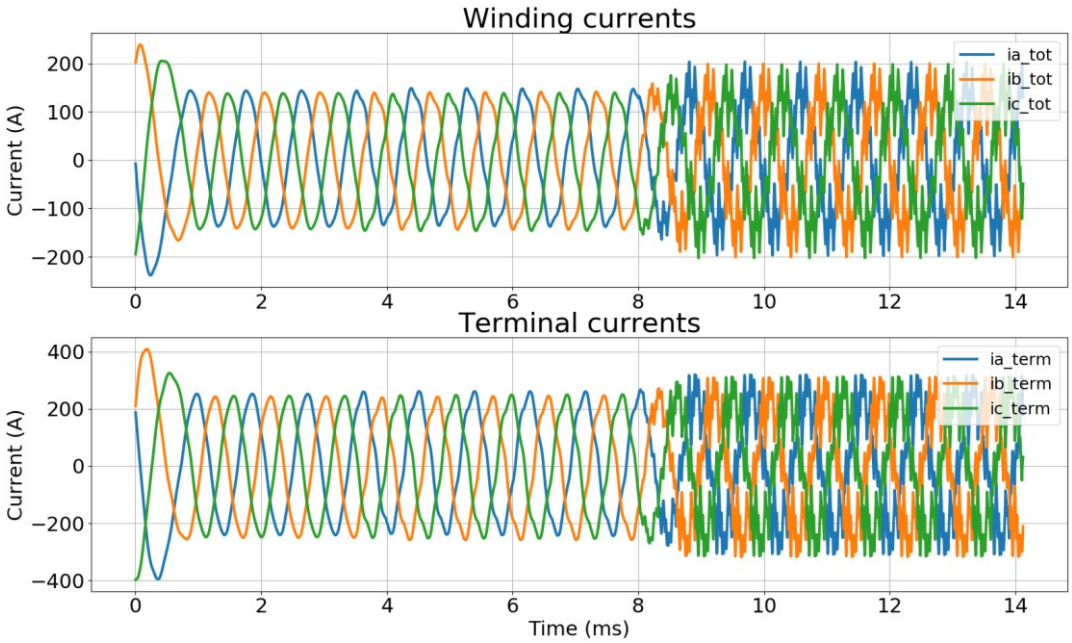

Figure 39. *Winding and terminal currents.*

According to Figure 39, the current quality decreases significantly. This is due to the PWM voltage supply. The RMS values of the winding and terminal currents are around 104.66 A and 181.17 A respectively. This shows about 10 A increase in the currents because of the PWM supply.

The torque and input power are studied next with the PWM voltage supply. Figure 40 shows these values over the whole simulation.

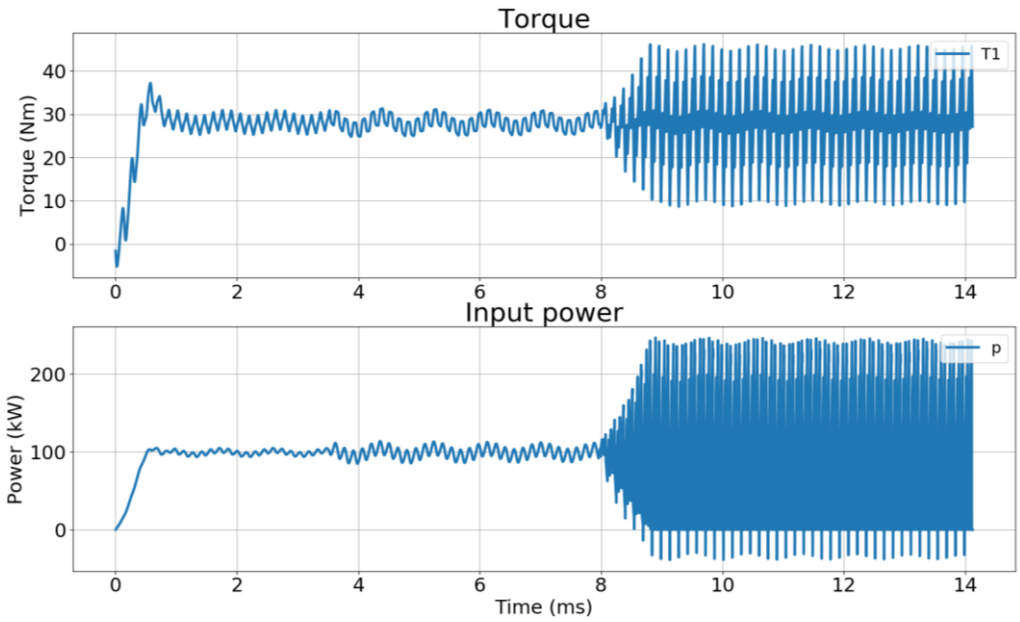

Figure 40. *Torque and input power of the motor.*

As can be seen from Figure 40, the torque and input power values show some significant ripple after the voltage supply is changed to PWM. This is normal since the voltage and currents are far from sinusoidal as seen from the previous figures. The average values, however, should be close to the rated values, which is shown in the next figure.

The torque, input power and losses at different parts of the rotor are studied next in one fundamental period. Figure 41 shows these curves and their average values.

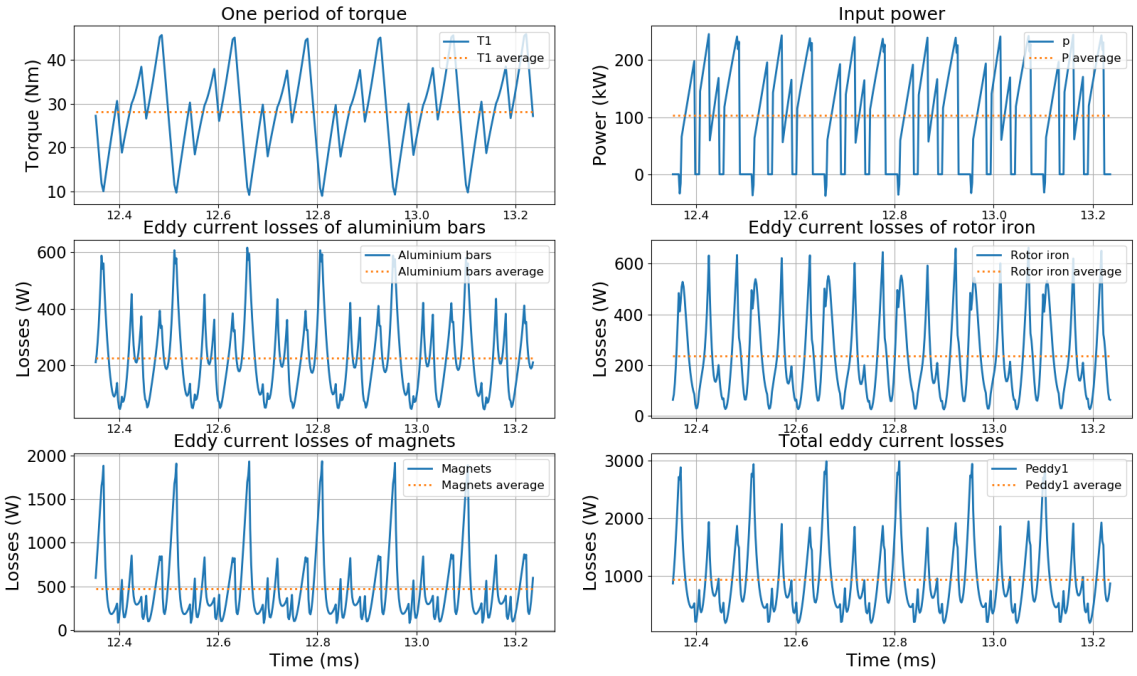

Figure 41. *Torque, input power and losses in one fundamental period.*

The fundamental period in Figure 41 is taken between 12.35 ms – 13.24 ms in the simulations. Compared to the sinusoidal supply (Figure 37), the curves show substantial ripple. In addition, the loss values increase significantly in this case. The eddy current losses for the aluminum bars, rotor iron and magnets are 225.96 W, 236.02 W and 474.45 W respectively. The total eddy current losses are 936.44 W and with the copper losses, the total losses increase to 1395.38 W. The power balance is 2252.52 W and it is 2.17 % of the input power. The power balance value is higher compared to the sinusoidal supply but low enough to be neglected. The average values for the torque and input power are 28.09 Nm and 103.662 kW respectively.

At last, the sinusoidal and the PWM voltage supply values are summarized. The summarized values consist of torque, input power, shaft power and the different losses. Table 10 shows the results.

Table 10. *Torque, input power and losses at nominal operation.*

Variable	***Symbol***	***Sine supply***	***PWM supply***
Torque	T_1	28.08 Nm	28.09 Nm
Input power	P_{in}	99.707 kW	103.662 kW
Shaft power	$P_{\mathrm{shaft}} = \omega_{\mathrm{n}} T_{\mathrm{n}}$	99.995 kW	100.014 kW
Copper losses	P_{Cu}	414.13 W	458.95 W
Aluminum losses	P_{alu}	62.75 W	225.96 W
Rotor iron losses	P_{rotor}	46.74 W	236.02 W
Magnets losses	P_{mag}	74.77 W	474.45 W
Eddy current losses	P_{eddy}	184.25 W	936.44 W
Total losses	P_{tot}	598.39 W	1395.38 W

According to Table 10, the PWM voltage supply increases the eddy current losses substantially. In addition, the copper losses increase since the current RMS values are higher with PWM voltage supply. Eddy currents increase by 752.19 W and copper losses by 44.82 W. The increase in total losses is 796.99 W. These losses could be decreased by increasing the switching frequency of the frequency converter since the output would be smoother and closer to sinusoidal (still far from ideal). The losses increase significantly but the high speed is impossible to reach with the sinusoidal supply since the frequency in the grid is 50 Hz and there is no gearbox attached.

6.3 No-load simulations

The same simulations that were done in the loaded motor are now done for the motor without the load. In these simulations, only the power angle between the stator and the rotor field is different. The power angle and load current would be zero in the ideal case. In practice, there is always some mechanical losses due to the friction of air in the air gap and there will be some load current in the motor. The power balance equation is not used in the no-load simulations. The rotor-starting angle is adjusted so that the torque value is close to zero.

6.3.1 Sinusoidal supply

In these simulations, the same figures are plotted and compared to the nominal load operation. In addition, the same methods are used to reduce the transients. The main difference is that the torque average is set to zero. Figures 42-44 show the terminal voltages, currents, torque and input power values.

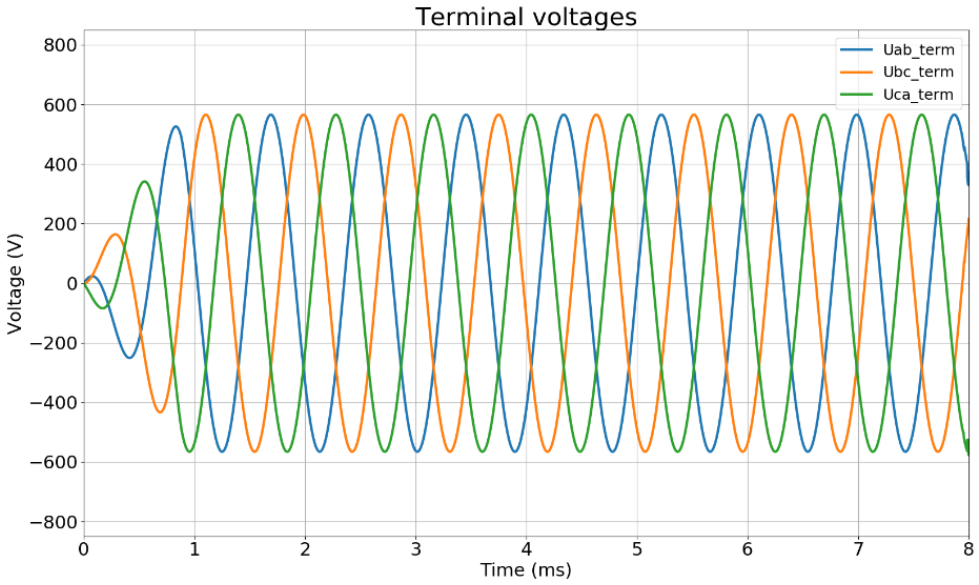

Figure 42. *Terminal voltages.*

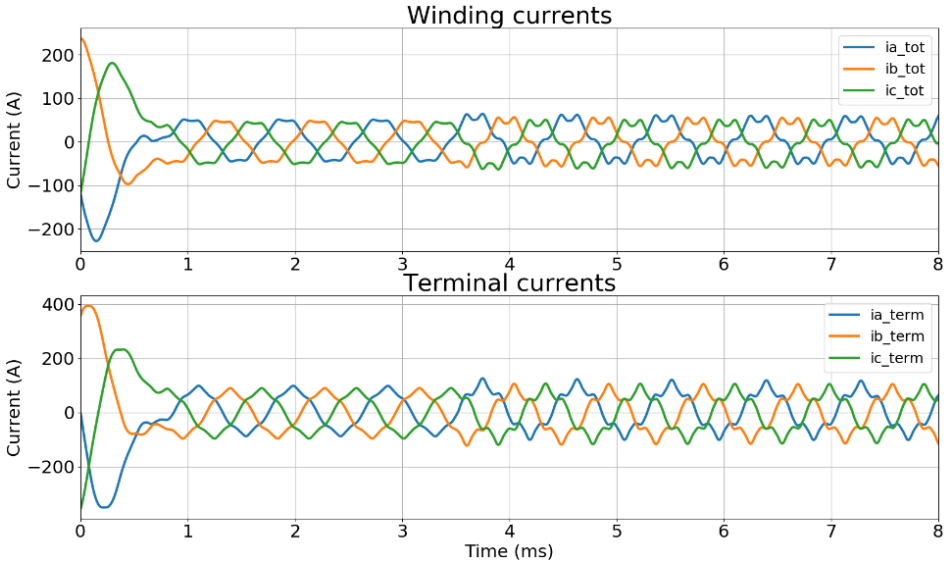

Figure 43. *Winding and terminal currents.*

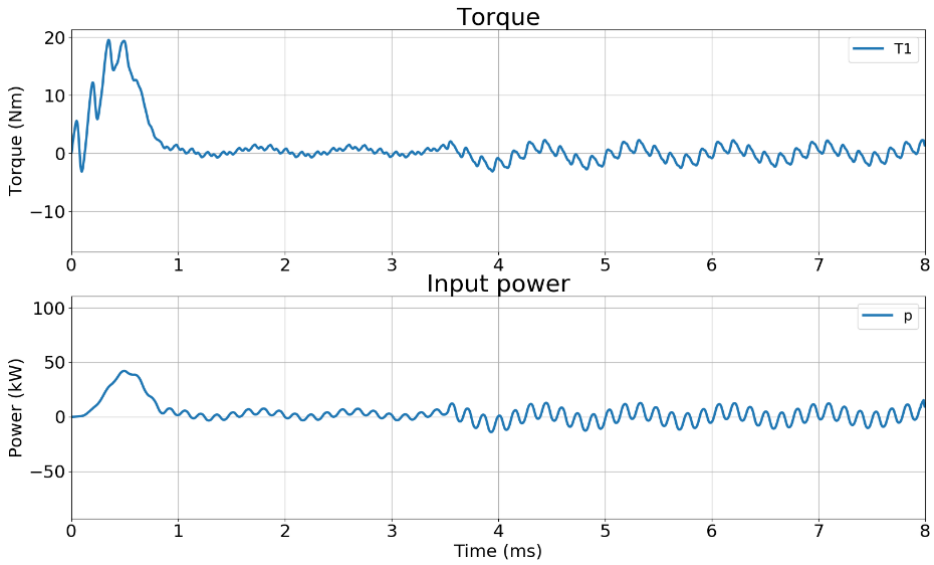

Figure 44. *Torque and input power of the motor.*

The terminal voltage RMS values are the same as before because the voltage supply is not modified in these simulations. The values are around 400 V RMS like in loaded motor. The winding and terminal currents are around 36.82 A and 63.78 A respectively. The terminal currents in no-load are 37 % of the load currents with the sinusoidal voltage supply. In Figure 44, the no-load torque and input power are close to zero.

The torque, input power and losses at different parts of the rotor are studied next in one fundamental period. Figure 45 shows these curves and their average values at no-load operation.

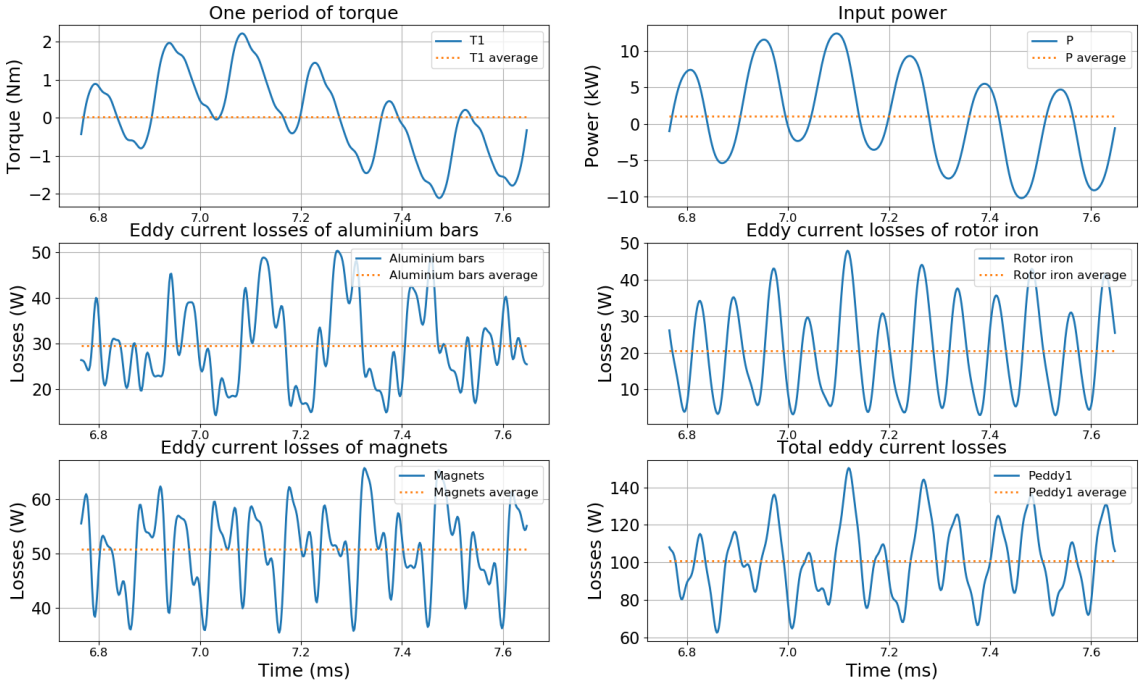

Figure 45. *Torque, input power and losses in one fundamental period.*

The fundamental period in Figure 45 is taken from the same interval as in nominal load simulations. The eddy current losses for the aluminum bars, rotor iron, and magnets are 29.62 W, 20.55 W and 50.83 W respectively. The total eddy current losses are 100.99 W and with the copper losses, the total losses increase to 157.52 W. The total losses for the nominal load operation were 598.39 W thus the losses decrease by 440.87 W in no-load operation. The main reason for this is the substantially reduced winding and terminal currents. The copper losses, for example, are proportional to the square of the winding currents.

6.3.2 PWM supply

The PWM voltage supply has been implemented similarly as in the nominal load operation. Figures 46-48 show the terminal voltages, currents, torque and input power values.

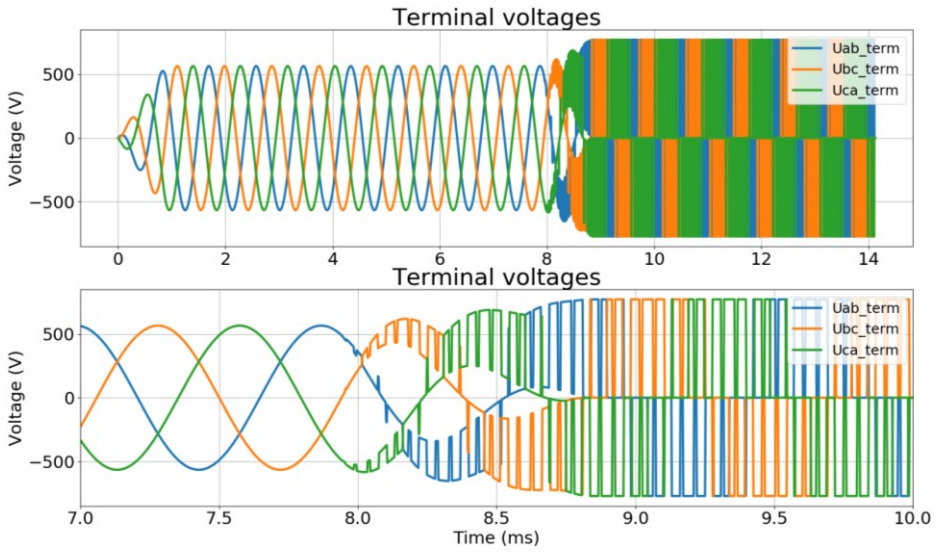

Figure 46. *Terminal voltages.*

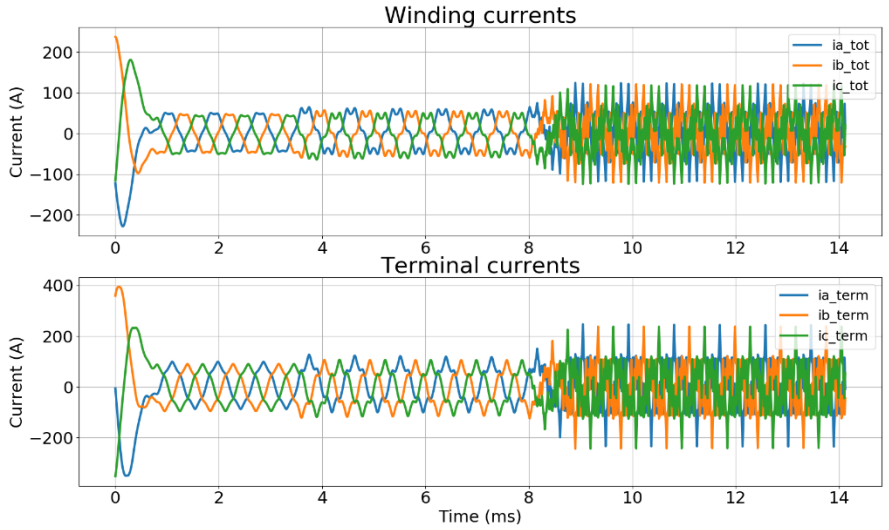

Figure 47. *Winding and terminal currents.*

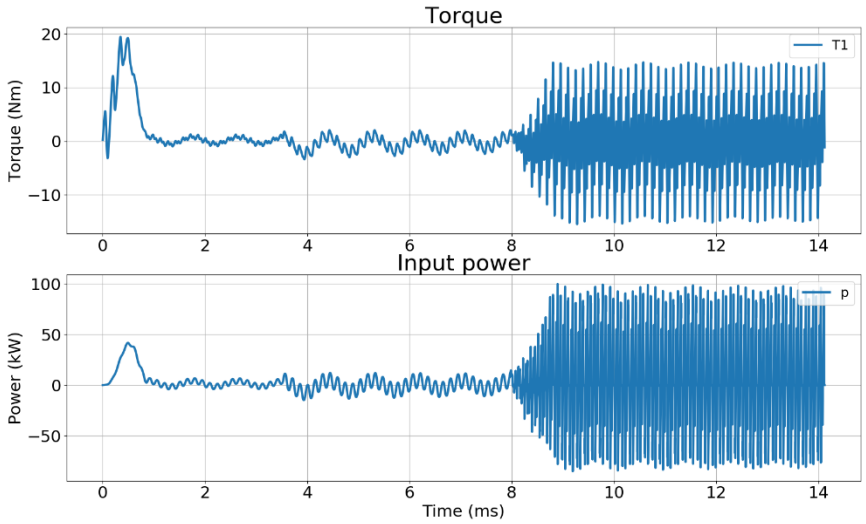

Figure 48. *Torque and input power of the motor.*

The terminal voltage RMS values are the same as before because the voltage supply is not modified in these simulations. The values are around 400 V RMS like in loaded motor. The winding and terminal currents are around 48.39 A and 83.83 A respectively. According to this, the terminal currents in no-load are 46.27 % of the load currents with PWM voltage supply. In Figure 48, the no-load torque and input power average values are close to zero.

The torque, input power, and losses at different parts of the rotor are studied next in one fundamental period. Figure 49 shows these curves and their average values at no-load operation.

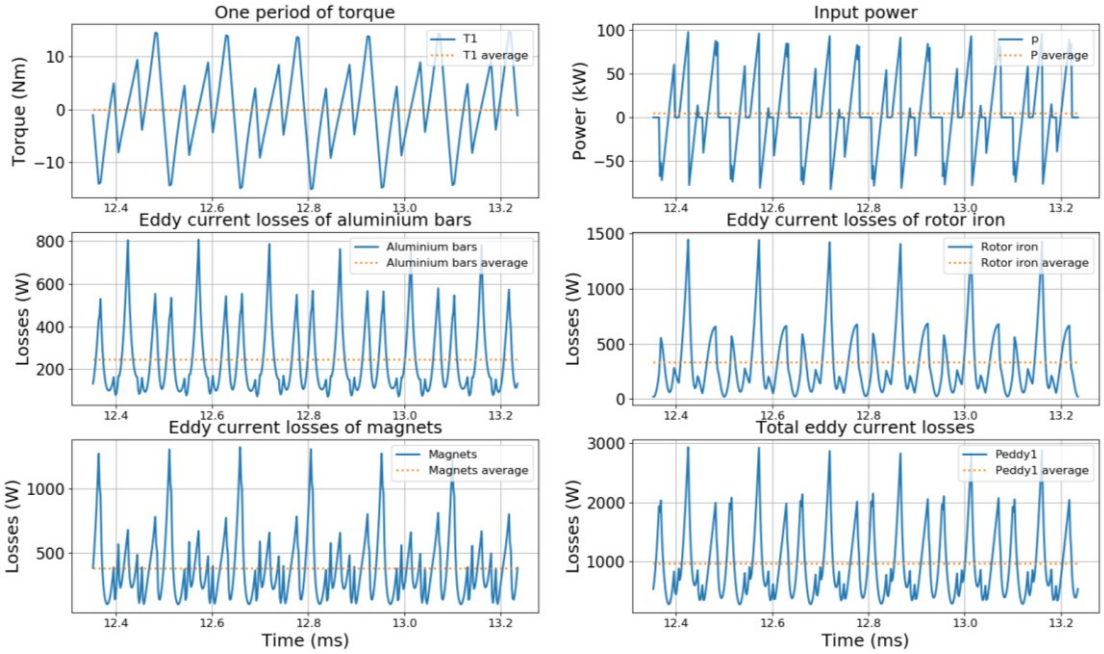

Figure 49. *Torque, input power and losses in one fundamental period.*

The fundamental period in Figure 49 is taken from the same interval as in nominal load simulations. The eddy current losses for the aluminum bars, rotor iron, and magnets are 247.65 W, 336.16 W and 378.92 W respectively. The total eddy current losses are 962.72 W and with the copper losses, the total losses increase to 1061.02 W. The total losses for the nominal load operation were 1395.38 W thus the losses decrease by 334.36 W in no-load operation. This is due to the same reasons as for the sinusoidal supply.

At last, the sinusoidal and the PWM voltage supply values are summarized. The summarized values consist of the torque, input power, shaft power and different losses. Table 11 shows the results.

Table 11. *Torque, power and losses at no-load operation.*

Variable	***Symbol***	***Sine supply***	***PWM supply***
Torque	T_1	0.026 Nm	0.008 Nm
Input power	P_{in}	1.040 kW	5.211 kW
Shaft power	$P_{\text{shaft}} = \omega_{\text{n}} T_1$	92.01 W	27.17 W
Copper losses	P_{Cu}	56.53 W	98.30 W
Aluminum losses	P_{alu}	29.62 W	247.65 W
Rotor iron losses	P_{rotor}	20.55 W	336.16 W
Magnets losses	P_{mag}	50.83 W	378.92 W
Eddy current losses	P_{eddy}	100.99 W	962.72 W
Total losses	P_{tot}	157.52 W	1061.02 W

According to Table 11, the PWM voltage supply increases the eddy current losses significantly. Eddy currents increase by 861.73 W and copper losses by 41.77 W. The increase in total losses is 903.50 W. These losses could be decreased by increasing the switching frequency of the frequency converter since the output would be smoother and closer to sinusoidal (still far from ideal).

6.4 Results summary

This chapter summarizes all the previous results. Table 12 shows the summarized losses.

Table 12. *Summary of the losses at every operation point.*

Variable	***Nominal load***	***Nominal load***	***No load***	***No load***
Supply	Sine	PWM	Sine	PWM
Copper losses	414.13 W	458.95 W	56,53 W	98,30 W
Aluminum losses	62.75 W	225.96 W	29,62 W	247,65 W
Rotor iron losses	46.74 W	236.02 W	20,55 W	336,16 W
Magnets losses	74.77 W	474.45 W	50,83 W	378,92 W
Eddy current losses	184.25 W	936.44 W	100,99 W	962,72 W
Total losses	598.39 W	1395.38 W	157,52 W	1061,02 W

The copper losses decrease significantly when changing from a nominal load to no-load operation. The losses decrease from 458,95 W to 98,30 W with PWM voltage supply. This is due to the decreased winding and terminal currents. In an ideal situation, there would be no currents at all since there is no load for the motor. However, there are always some mechanical losses due to the friction of the air in the air gap when the motor is running. The mechanical losses will require some load current to keep the motor running and the currents, in turn, induce winding and eddy current losses. This resists the rotation of the motor. It is clearly seen from Table 12, that the losses increase always when changing from sine supply to PWM supply voltage. The total losses are higher in nominal load compared to the no-load operation. The main reason for this is the increased currents in the nominal load operation.

The eddy current loss behavior is interesting in these simulations. The eddy currents decrease when changing from nominal load to no-load operation when supplying the stator windings by sinusoidal supply. However, with the PWM supply voltage, the eddy currents slightly increase when changing from nominal load to no-load operation. Figure 39 and Figure 47 shows that the current waveforms are far more distorted in the no-load operation, which increases the total eddy current losses. The aluminum and rotor iron eddy currents increase and the eddy currents in the magnets decrease when changing the operation point from nominal load to no-load.

6.5 Field solution comparison

This chapter shows the field solution for the magnetic flux density and joule heating at nominal and no load operation supplied by PWM voltage. Figure 50 shows the magnetic flux density field with flux lines at nominal and no-load operation.

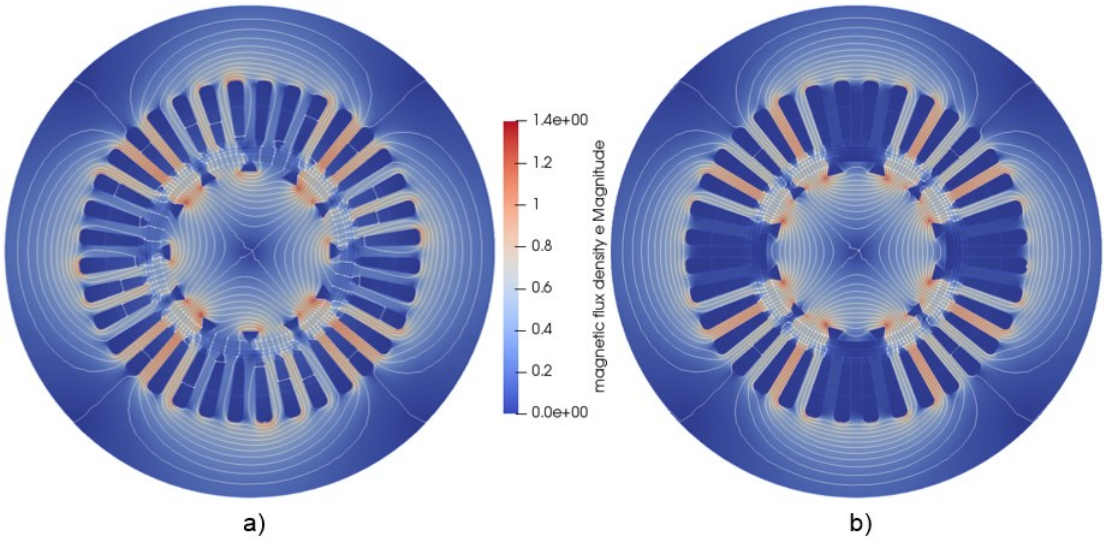

Figure 50. *Magnetic flux density* ***B*** *with flux lines at nominal load (a) and no-load (b) operation.*

The main difference between the load operations is the rotor angle. The screenshots have been taken from the Paraview at the last time step (7 200). Figure 50 a shows the nominal operation field solution and the Figure 50 b shows the no-load operation. At nominal load, the stator created magnetic field is around 15 degrees ahead of the rotor created magnetic field. This can be seen from Figure 50 a since the flux lines are focused on the left magnets of the four poles. In no-load operation, the magnetic flux lines are focused evenly on the magnets in the poles. The no-load operation is demonstrated well since the stator and the rotor fields are perpendicular to each other at the air gap and the flux lines are evenly distributed. According to the field solution, the maximum value of the magnetic flux density in the stator teeth is about 1,4 T. This seems reasonable.

The joule heating variable in Elmer demonstrates the resistive dissipation power. In this case, the eddy current losses. Figure 51 shows the joule heating field at nominal and no-load operation at the last time step (7200).

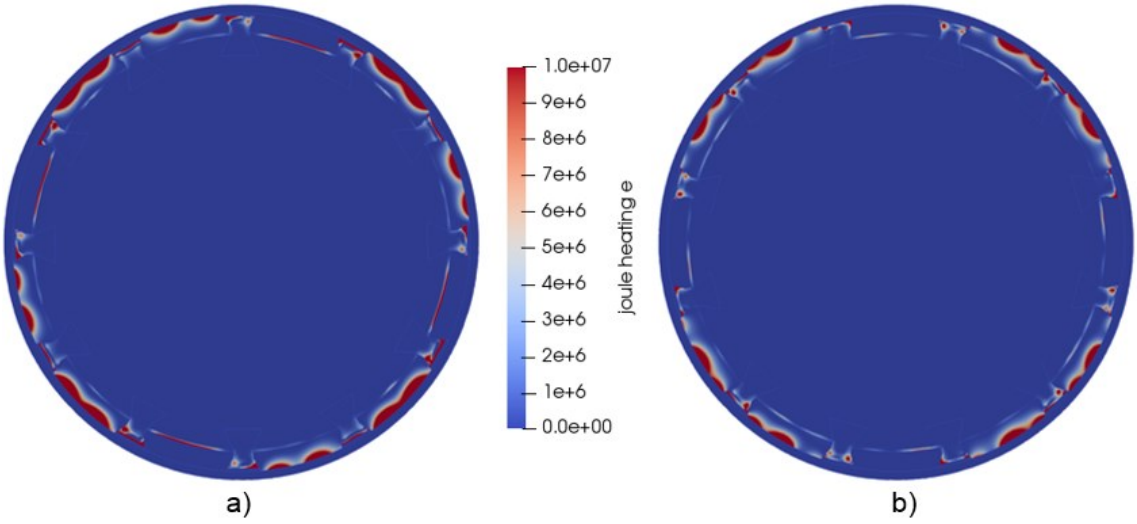

Figure 51. *Joule heating at nominal load (a) and no load (b) operation.*

In the joule heating Figure 51, there is no major difference since the total eddy losses differ only 26,28 W and this difference is quite hard to demonstrate in the field solution. Only the rotor needs to be inspected in this case since the eddy currents are only calculated in the rotor parts. The skin depth effect shows how deep the eddy currents can penetrate. Using (3.4), the skin depth can be calculated for every rotor material. The skin depths for the aluminum, rotor iron and magnets are 3,48 mm, 6,54 mm and 25,89 mm respectively. The skin depth distances for aluminum and rotor iron are substantially shorter compared to the magnets because the electric conductivity values for these materials are higher. The effect of the short skin depth values can be seen from Figure 51. The eddy currents in the aluminum and rotor iron only show on the surface of these materials. In the magnets, the eddy currents can penetrate deeper to the surface because of the higher skin depth value.

6.6 Comparing to the measured values

There are also some measurements at no-load operation with PWM voltage supply but the data is limited to two measurement points and cannot be effectively compared to the simulation results. Another reason for this is the limits of the work. In the measurement data, all the possible losses occur and in the simulations, only the stator winding copper losses and rotor eddy current losses are studied. The most significant difference in these losses consists of the stator iron losses and the mechanical (friction) losses. Figure 52 shows the test setup for the measurements.

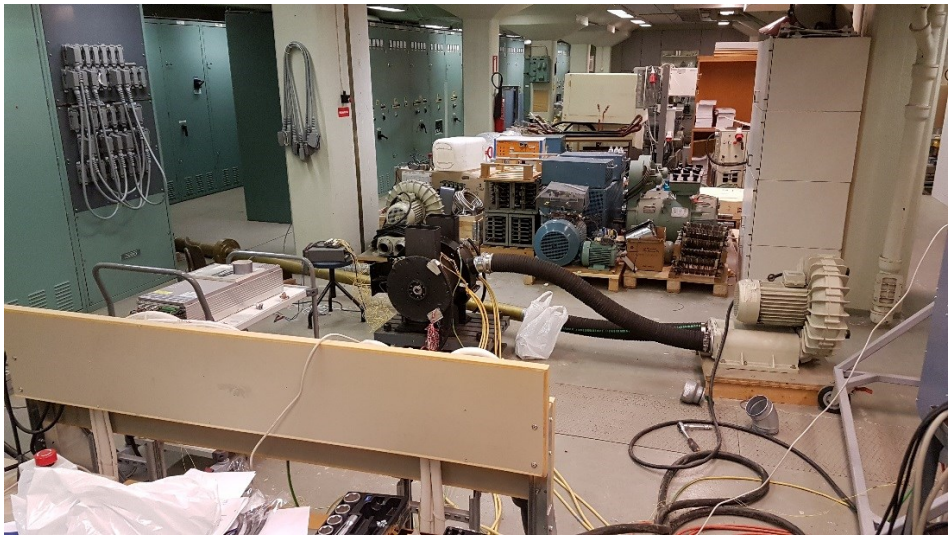

Figure 52. *Test setup for measurements.*

The black motor in Figure 52 is the simulated motor. The measured input powers at no load changed between 2,1 kW at 12 000 rpm and 3,2 kW at 20 000 rpm. However, it is difficult to create a reliable loss distribution model only from these two points and these losses include the air friction losses. The hysteresis losses could be obtained by curve fitting of these results and assuming that the losses would be zero when the rotor is not rotating. With the PWM voltage supply, this may not be the case. This would give three different points and with the curve fitting the losses at 34 000 rpm could be estimated. The hysteresis losses are a major loss component in electrical machines and they should be considered in the loss comparison. However, with the lack of reliable coefficients for the Steinmetz equation (3.6) these losses are not considered in this thesis.

7. CONCLUSIONS

An Ingersoll-Rand made high-speed permanent magnet synchronous motor was studied by four different simulations. The motor was operating at nominal or no-load and supplied by sinusoidal supply or frequency converter. The eddy current and copper losses were calculated at these operation points. The main objective was to study the eddy current losses behavior at these different operation points. The effect of the frequency converter was obtained when comparing the results of the sinusoidal and PWM voltage supplies. From these results, it can be seen that the eddy current losses increase substantially with the PWM voltage supply. The copper losses are always higher in the loaded motor since the motor current is proportional to the loading. Ideally, in the no-load situation there are no currents but in practice, there is always some load consisting of mechanical losses. In the results, there was some interesting behavior when comparing the nominal load and no-load operations with different supplies. The total eddy current losses decrease when changing the loading from nominal to no-load with sinusoidal supply. However, with the PWM supply, the losses increase in the same situation. This is due to the increased current transients in the no-load current waveforms. The increase of the PWM supply switching frequency would improve the current waveforms and the eddy current losses would be closer to the sinusoidal values.

The workflow for this thesis was selected by the author. The workflow makes use of the following software: SpaceClaim, Salome, Elmer, Paraview and Python. SpaceClaim is the only commercial software in this workflow. FS Dynamics had the license for it and the software was found easy to use during this thesis. The overall workflow was rather long and even a slight modification to the geometry required the whole workflow process all over again. However, the use of Elmer as a solver requires some other software for geometry, mesh and post-process when studying complex simulation models. The advantage of Elmer was the easy and effective parallelization of the simulation model. The simulation results were calculated with an office computer using 12 cores. The post-process software were found useful and they produced very nice field solutions and plots. Overall, this workflow was successfully implemented in this thesis.

The start-up transients and how they can be reduced in the simulations were also studied. At the start of the study, the simulation model would not reach steady-state no matter how long the simulation time was. In this thesis, three different methods were developed in the process, which are discussed in detail at section 6.1. The motor is started with a ramped sinusoidal voltage, the electric conductivity is added after the model has reached steady-state with sinusoidal supply and at last the sinusoidal voltage is changed to PWM voltage during one fundamental period. The hardest part was to figure out how to add the

electric conductivity to the model without excessive transients. These methods were found working rather well in the simulations.

Even though the simulation model was found working and the results were obtained, there is some future work to be done. The measured and simulated results could not be effectively compared since there is not enough measurement data to construct reliable loss coefficients for the simulations. That is unfortunate since it would have added some extra credibility for the thesis. In addition, the simulation model only solves the eddy current and copper losses. In practice, the stator iron losses (hysteresis) and mechanical losses are taken into account. Therefore, the simulation results focus on comparing the different motor operation points instead of comparing the simulation results to measured values.

The eddy current losses are mainly a 3D problem and the model is created in 2D, which is not as accurate. In the geometry section, the 3D motor model consists of two separate stator structures and the permanent magnets are divided into 8 smaller magnets per pole. In 2D-model, the axial length is taken into account by multiplying the solution with effective axial length. This distorts the simulation results since these phenomena are hard to implement with 2D-model. In addition, the simulation time could have been reduced by using a quarter or half of the simulation model.

REFERENCES

[1] P. Råback, M. Malinen, Overview of Elmer, CSC – IT Center for Science, 2018, 10 p.

[2] J. Luomi, Finite element methods for electrical machines, Chalmers University of Technology, Study material, 1993, 176 p.

[3] P. Ponomarev, FEM modeling of PMSMs using Elmer, 2015, 56 p.

[4] P. Ponomarev, SEMTEC report Elmer FEM – induction machine tutorial, 2017, 95 p.

[5] J. Keränen et al, Efficient parallel 3-D computation of electrical machines with Elmer, IEEE Transactions on Magnetics, Vol. 51, No. 3, 2015, pp. 1-4.

[6] P. Ponomarev, L. Aarniovuori, J. Keränen, Selection of optimal slice count for multi-slice analysis of skewed induction motors, IECON 2017 – 43rd Annual Conference of the IEEE Industrial Electronics Society, 2017, pp. 2149-2153.

[7] J. Keränen, P. Ponomarev, S. Sathyan, J. Kataja, A. Belahcen, Magneto-structural simulation of an induction motor start-up using nodal magnetic forces in Elmer, Rakenteiden mekaniikka (Journal of Structural Mechanics), Vol. 50, No. 3, 2017, pp. 296-299.

[8] P. Ponomarev, J. Keränen, P. Pasanen, Electromagnetic transient finite element 3D modelling of electrical machines using open-source tools, 2016 XXII International Conference on Electrical Machines (ICEM), 2016, pp. 1657-1661.

[9] A. Borisavljevic, Limits, modeling, and design of high-speed permanent magnet machines, Springer, 2013, 228 p.

[10] K. Nousiainen, Sähkömagnetiikka, Tampere University of Technology, Study material, 2018.

[11] J. Pyrhönen, T. Jokinen, V. Hrabovcova, Design of rotating electrical machines, John Wiley & Sons, 2014, 615 p.

[12] S. R. Trout, Material selection of permanent magnets, considering thermal properties correctly, For the Electric Manufacturing and Coil Winding Conference, 2001, 7 p.

[13] M. Salo, Sähkökäyttöjen ohjaustekniikka, Tampere University of Technology, Study material, 2008, 156 p.

[14] J. Bastman, Sähkökoneet, Tampere University of Technology, Study material, 2011, 189 p.

[15] J. Rekola, Synchronous machine dynamic model, Tampere University of Technology, Lecture notes, 2016, 70 p.

[16] P. Salminen, J. Pyrhönen, M. Niemelä, A comparison between surface magnets and embedded magnets in fractional slot wound PM-motors, ISEF 2003 – 11th International Symposium on Electromagnetic Fields in Electrical Engineering, 2003.

[17] S. Chapman, Electric machinery fundamentals fourth edition, McGraw-Hill Companies, 2005, 746 p.

[18] P. Rasilo, A. Arkkio, Modeling the effect of inverter supply on eddy-current losses in synchronous machines, SPEEDAM 2010, 2010, 5 p.

[19] L. Hietalahti, Tehoelektroniikan perusteet, Tammertekniikka, 2011, 124 p.

[20] N. Mohan, T. Undeland, W. Robbins, Power electronics: converters, applications, and design, Wiley, 1989, 667 p.

[21] S. Li, Y. Li, W. Choi, High-speed electric machines: challenges and design considerations, IEEE Transactions on Transportation Electrification, vol. 2, no. 1, 2016, pp. 2-13.

[22] J. Larjola, A. Arkkio, J. Pyrhönen, Suurnopeustekniikka, Yliopistopaino, 2010, 163 p.

[23] C. Huynh, L. Zheng, D Acharya, Losses in high speed permanent magnet machines used in microturbine applications, Journal of Engineering for Gas Turbines and Power, Vol. 131, No. 2, 2009, 6 p.

[24] A. Jassal, H. Polinder, J. A. Ferreira, Literature survey of eddy-current loss analysis in rotating electrical machines, IET Electric Power Applications, Vol. 6, No. 9, 2012, pp. 743-752.

[25] P. Rasilo, Iron losses, eddy currents in the windings, Tampere University of Technology, Lecture notes, 2016, 32 p.

[26] W. Roshen, Iron loss model for permanent-magnet synchronous motors, IEEE Transactions on Magnetics, vol. 43, no. 8, 2007, pp. 3428-3434.

[27] J. Cardoso, Electromagnetics through the finite element method, CRC Press, 2017, 213 p.

[28] J. Smajic, How to perform electromagnetic finite element analysis, NAFEMS, 2016, 120 p.

[29] P. P. Silvester, R. L. Ferrari, Finite elements for electrical engineers, Cambridge U. P., 1983-1990, 344 p.

[30] N. Bianchi, Electrical machine analysis using finite elements, CRC Press, 2005, 304 p.

[31] P. Rasilo, Introduction to finite element method elements and shape functions, Tampere University of Technology, Lecture notes, 2016, 31 p.

[32] R. Bargallo, Finite elements for electrical engineering, Universitat politecnica de Catalunya, Study material, 2006, 325 p.

[33] J. Haataja, J. Heikonen, Y. Leino, Numeeriset menetelmät käytännössä, CSC – IT Center for Science, 2002, 415 p.

[34] A. Arkkio, Analysis of induction motors based on the numerical solution of the magnetic field and circuit equations, Helsinki University of Technology, Doctoral dissertation, 1987, 97 p.

[35] E. Vikman, Kestomagnetoidun roottorin mekaniikkasuunnittelu ja –analysointi, Lappeenranta University of Technology, Master's thesis, 2014, 111 p.

[36] Conductive materials, metals and stainless steels properties table, Tibtech Innovations, website. Available (accessed on 24.10.2018): https://www.tibtech.com/conductivite.php?lang=en_US

[37] Neodymium magnets – overview, Eclipse Magnetics, website. Available (accessed on 24.10.2018): https://www.eclipsemagnetics.com/row/magnetic-materials-rare-earth-neodymium-ndfeb/

[38] P. Råback, ElmerGrid manual, CSC – IT Center for Science, 2015, 43 p.

[39] J. Ruokolainen, M. Malinen, P. Råback, T. Zwinger, A. Pursula, M. Byckling, ElmerSolver manual, CSC–IT Center for Science, 2018, 159 p.

[40] P. Råback, M. Malinen, J. Ruokolainen, A. Pursula, T. Zwinger, Elmer models manual, CSC–IT Center for Science, 2018, 313 p.

APPENDIX A: WINDING DIAGRAMS

Table 1. *Winding parameters.*

Variable	***Value***
Number of slots	36
Number of poles	4
Slots per pole and phase	3
Coil pitch	6/9
Number of turns/slot	16
Approx. length of a turn	700 mm
Number of wires in a turn	17
Diameter of wire	0,63 mm
Number of wires/slot	272
Connection	2xDelta
Connection cable	6x50 mm

The winding diagrams for all the phases are shown in Figures 1-4. Note that the N and D ends represents the two different stator structures as demonstrated in the thesis. In addition, the connection is divided for both N and D ends and there are internal delta-connections at each end. In Figures 2-4, the slot polarities are marked as + or – signs in slots.

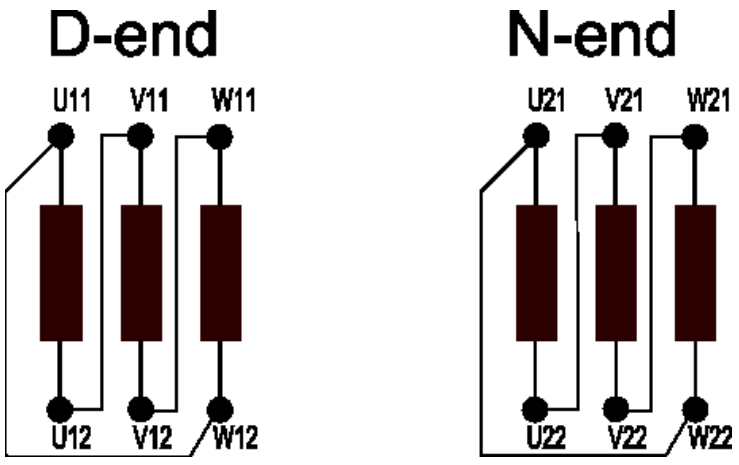

Figure 1. *Connection diagram for windings.*

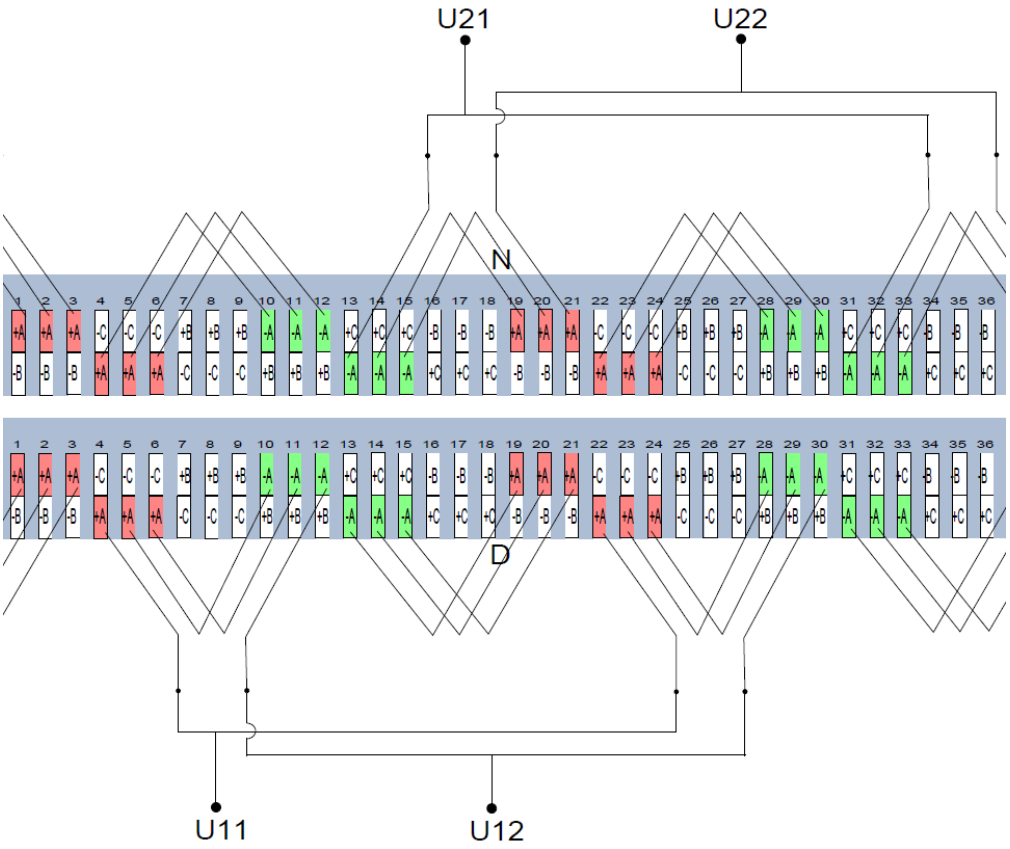

Figure 2. *Connection diagram for phase A.*

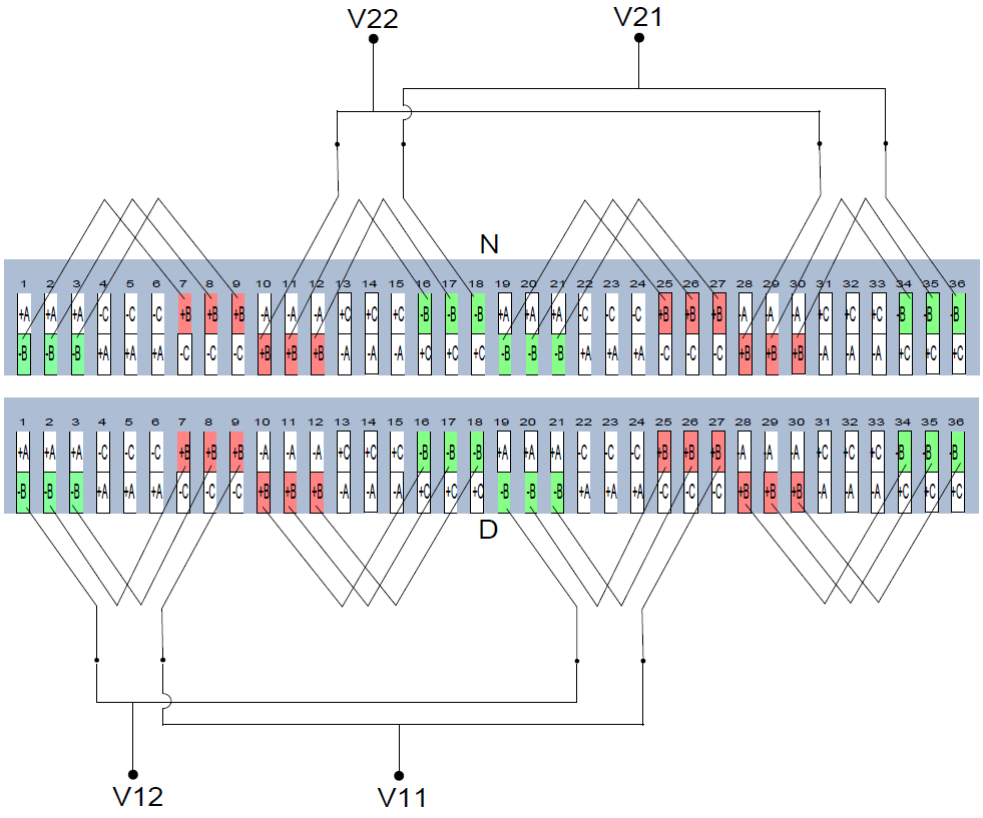

Figure 3. *Connection diagram for phase B.*

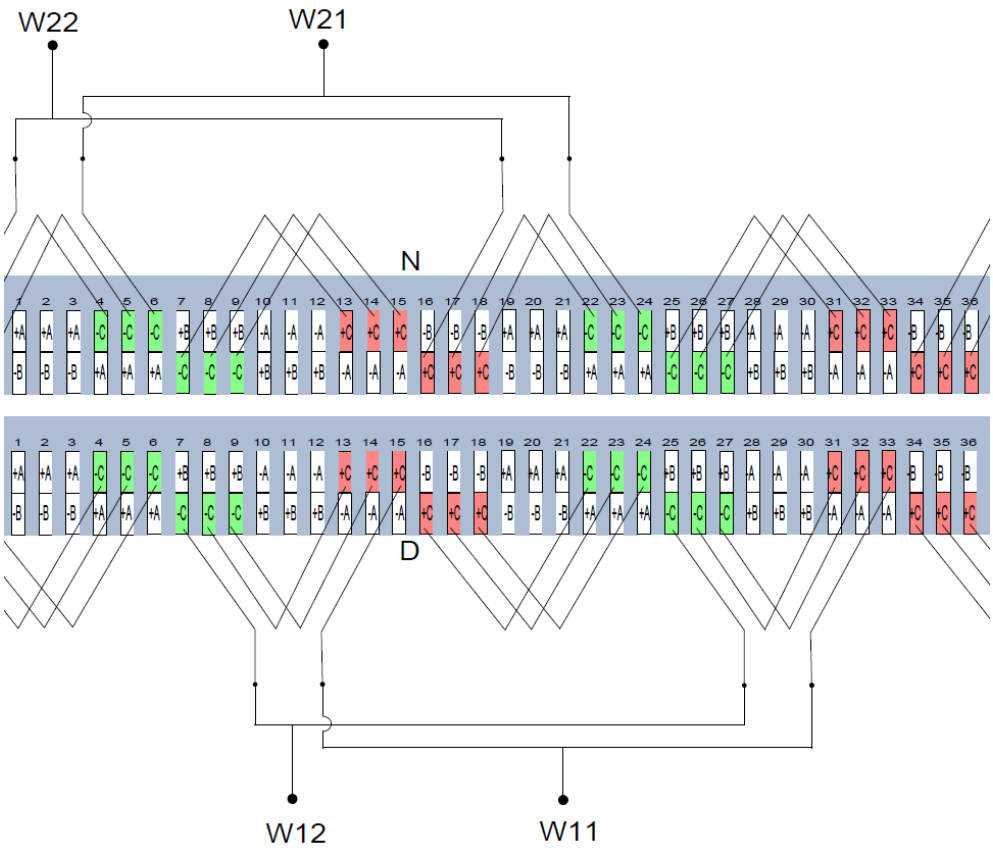

Figure 4. *Connection diagram for phase C.*

APPENDIX B: STATOR IRON BH-CURVE

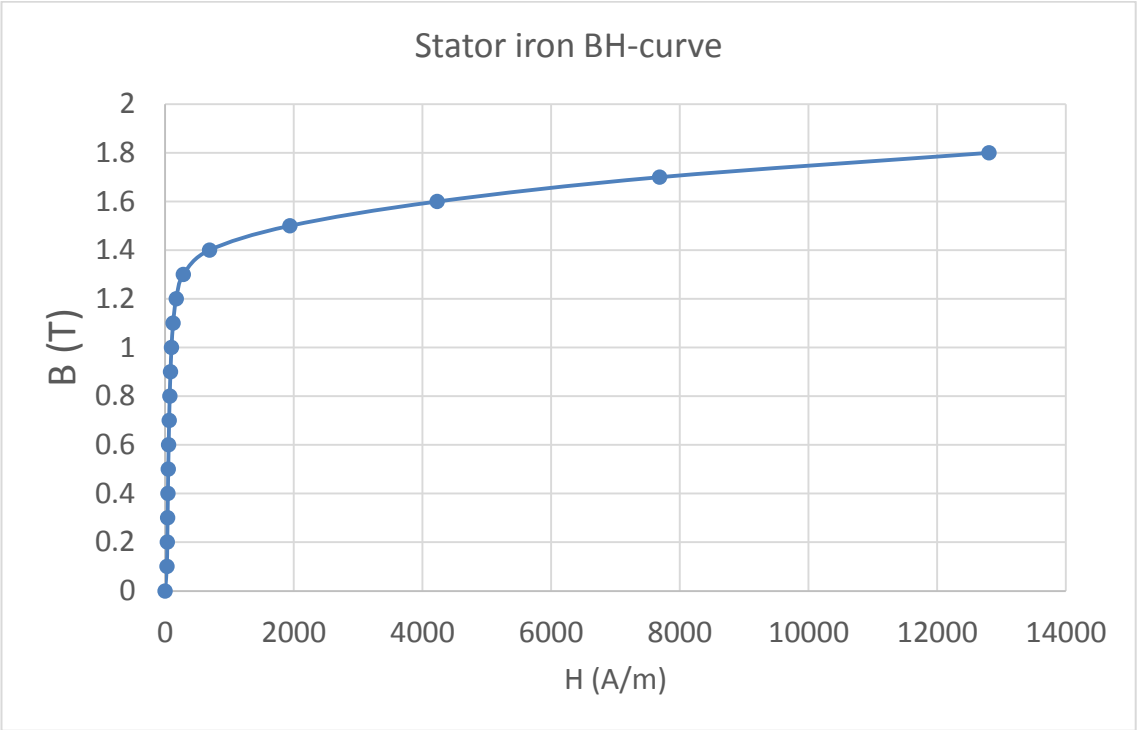

Figure 1. *Stator iron BH-curve.*

Table 1. *BH-curve data points.*

B (T)	H (A/m)
0	0
0.1	26
0.2	33
0.3	38
0.4	43
0.5	48
0.6	55
0.7	62
0.8	71
0.9	83
1	99
1.1	124
1.2	171
1.3	283
1.4	688
1.5	1937
1.6	4230
1.7	7688
1.8	12808

APPENDIX C: ROTOR IRON BH-CURVE

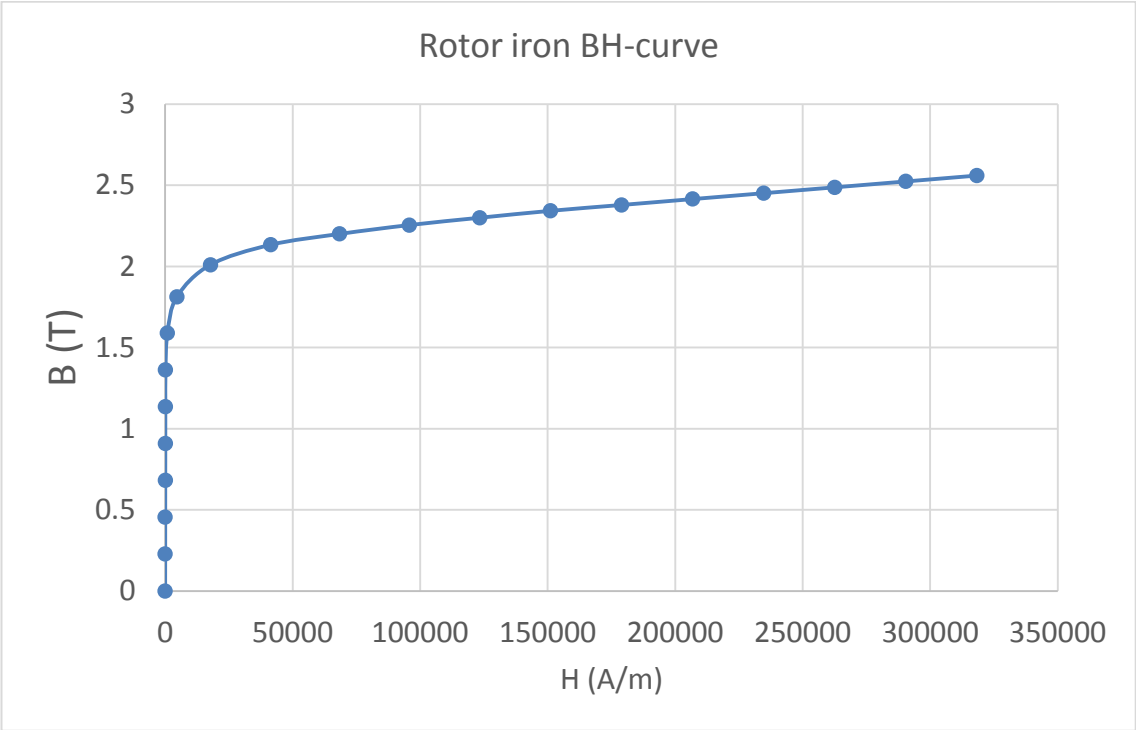

Figure 1. *Rotor iron BH-curve.*

Table 1. *BH-curve data points.*

B (T)	H (A/m)
0	0
0.227065	13.8984
0.45413	27.7967
0.681195	42.3974
0.90826	61.4157
1.13533	82.3824
1.36239	144.669
1.58935	897.76
1.81236	4581.74
2.01004	17736.2
2.13316	41339.3
2.19999	68321.8
2.25479	95685.5
2.29993	123355
2.34251	151083
2.37876	178954
2.41501	206825
2.45126	234696
2.4875	262568
2.52375	290439
2.56	318310